Probing Entangled States of the Nuclear-Electronic Quantum Magnet LiHoF$_4$

THÈSE N^O 7015 (2016)

PRÉSENTÉE LE 12 MAI 2016
À LA FACULTÉ DES SCIENCES DE BASE
LABORATOIRE DE MAGNÉTISME QUANTIQUE
PROGRAMME DOCTORAL EN PHYSIQUE

ÉCOLE POLYTECHNIQUE FÉDÉRALE DE LAUSANNE

POUR L'OBTENTION DU GRADE DE DOCTEUR ÈS SCIENCES

PAR

Ivan KOVAČEVIĆ

acceptée sur proposition du jury:

Prof. F. Mila, président du jury
Prof. H. M. Rønnow, directeur de thèse
Prof. D. M. Silevitch, rapporteur
Prof. M. Schechter, rapporteur
Dr G. Boero, rapporteur

EPFL

ÉCOLE POLYTECHNIQUE
FÉDÉRALE DE LAUSANNE

Suisse
2016

Everything around you
that you call life
was made up by people
that were no smarter than you.
And you can change it.
You can influence it.
You can build your own things
that other people can use.
— Steve Jobs

To my late grandfather, Vladisav.

Acknowledgements

First, I would like to thank my supervisor, Prof. Henrik Rønnow. He was always available for help and discussion while at the same time leaving enough space for creativity. His subtle guidance, combined with sharp problem solving skills and passion for knowledge, was leading me through the thesis. Instead of taking the safe path, Henrik showed me how to experiment off-piste.

Peter Babkevich taught me how to do neutron scattering experiments, analyse data and he was there to help in every phase of my project in the lab. Minki Chung taught me about nuclear magnetic resonance, helped me discover new topics in physics and showed me the art of writing an article. But most of all, I would like to thank Peter and Minki for their friendship and many memorable moments on our shared journey through science and life which made these 4 years a pleasurable experience.

Without the invaluable help from Giovanni Boero it would have been much harder to build the experimental setup. I am also grateful to M. Graf, S. S. Kim for their contribution in building the experimental setup.

All of the group members where very supportive from the very beginning. Julian Piatek showed me how dilution fridge works, Bastien Dalla Piazza taught me how to do computer calculations, Krunoslav Prša welcomed me in the lab, Pau Jorba Cabre helped me with designing the copper blocks for thermalization, Zhuo Quan Im simulated resonators' response, Elahi Shaik almost read the thesis, and Claudia Fatuzzo tolerated my music in the office and talked to me endlessly. I will always be grateful to Ivica Živković for pointing me in the right direction. I would like to thank Jagoda and Naunidh for proofreading the thesis.

This thesis is dedicated to my wife for sharing her dreams with me. And to my mum, dad, sister and grandma for believing in me.

Lausanne, 18 February 2016   I. K.

i

Abstract

Two objects are entangled when their quantum mechanical wavefunctions cannot be written in a separable product form. Entangling dissimilar quantum objects, or hybridization, has been suggested as a promising route to efficient quantum information processors, but mostly realized on a limited scale. Hybrid nuclear-electronic many-body systems remain a largely unexplored challenge to both experiments and theories. The prototypical transverse-field Ising ferromagnet $LiHoF_4$ is an ideal platform to address this issue. The Ising model is considered as an archetype both for the investigation of quantum criticality and for the evaluation of quantum simulators. The hyperfine coupling strength of a Ho^{3+} ion is exceptionally large, promoting a strong hybridization or entanglement between the nuclear and electronic moments. The magnetic coupling between the Ho^{3+} ions that leads to ferromagnetic ordering is predominantly through long-range dipole interactions, while nearest-neighbor exchange interaction is negligibly weak. Applying a transverse field induces a zero temperature quantum phase transition driven by quantum fluctuations. Altogether $LiHoF_4$ represents a unique nuclear-electronic quantum magnet, whose wavefunctions can be readily obtained by diagonalizing the Hamiltonian using the mean-field approximation.

In this thesis we develop an experimental scheme allowing us to quantify hybridized nuclear-electronic states in the model transverse field Ising system $LiHoF_4$. Using magnetic resonance the field and temperature evolution of the nuclear-electronic states are successfully traced across the whole phase diagram. We develop a theoretical framework based on mean-field calculations and linear response theory. Our experimental observation of the hybridization is remarkably well reproduced by the calculations based on parameters obtained from experiments probing three orders of magnitude higher energies. Thus armed, we find that the calculated entanglement entropy shows a peak at the quantum phase transition. This raises the tantalizing possibility that electronic entanglement is encoded onto the nuclear-electronic states, which presents an interesting avenue towards experimental probes of many-body entanglement.

Keywords: magnetism, quantum phase transition, magnetic resonance, quantum information, quantum simulation, entanglement entropy.

Résumé

Deux objets sont emmêlés quand leurs fonctions d'onde quantique mécanique ne peuvent être écrites dans la forme du produit séparable. En emmêlant des objets quantiques différents, la hybridation, a été suggéré comme la bonne façon pour le processeur efficace quantique informatique, mais principalement réalisé sur une échelle limitée. Les systèmes hybrides nucléaires électroniques multi corps reste un défi inexploré pour l'expérience et la théorie. Le Ising ferromagnet prototypique $LiHoF_4$ avec le champ transversal est une plateforme idéale pour aborder cette question. Le modèle Ising est considéré comme un archétype pour la recherche de la criticité quantique ainsi que pour l'évaluation de simulateurs quantiques. La force très fin de couplage d'un ion Ho^{3+} est exceptionnellement élevé, et cette force promeut une forte hybridation ou un enchevêtrement entre les moments nucléaires et électroniques. Le couplage magnétique entre les ions Ho^{3+} qui conduit à la commande ferromagnétique est essentiellement par des interactions dipolaires à longue portée, tandis que l'interaction de plus proches voisins est faible. L'application d'un champ transversal induit une température de zéro transition de phase quantique entraînée par les fluctuations quantiques. Au total, $LiHoF_4$ représente un magnet quantique nucléaire électronique unique, dont les fonctions d'onde peuvent être facilement obtenus par diagonalisation l'Hamiltonien en utilisant l'approximation du champ moyen. Dans cette thèse, nous développons un montage expérimental pour sonder l'état nucléaire électronique dans un système de Ising transversale champ modelé du $LiHoF_4$. En utilisant la résonance magnétique, l'évolution du champ et de la température des états nucléaires électronique est avec succès tracée à travers l'ensemble du diagramme de phase. Nous développons un cadre théorique sur la base de calculs de champ moyen qui est d'accord avec les observations expérimentales. Ayant établi expérimentalement que les fonctions d'onde de champ moyen sont une excellente approximation de la fonction d'onde réelle, nous les avons utilisées pour calculer l'enchevêtrement entropie de l'état fondamental entre des moments magnétiques électroniques et nucléaires. Nous constatons que l'entropie d'enchevêtrement entre les moments nucléaires et électroniques présente un pic à la transition de phase quantique. Ceci suggère que l'enchevêtrement électronique est codé sur chaque état nucléaire-électronique. Nos résultats ouvrent la voie à de nouvelles recherches théoriques et expérimentales de l'intrication quantique.

Acknowledgements

Contents

Contents

1 Introduction

Entangling dissimilar objects such as atom-photon, photon-spin, or nuclear-electronic spins, can bring together the merit of each element for efficient quantum information processing [1, 2]. Hybrid nuclear-electronic spin systems might enable fast gating on electron spins together with long storage on nuclear spins [3]. Simulating quantum many-body systems [4, 5] may also benefit from such hybridization, and foster the entanglement perspective on many-body phenomena [4]. Indeed entanglement increasingly provides a useful toolkit for many-body systems [6, 7, 8, 9, 10], for instance, by displaying a scaling behavior close to a quantum phase transition (QPT) [11, 12] or enabling identification of novel quantum phases like a topologically ordered one [13, 14, 15]. However, the efforts to realize hybrid quantum systems mostly focus on and is limited by a few body ones, and *hybrid many-body systems* remain a largely unexplored challenge to both experiments and theories.

The prototypical transverse-field Ising ferromagnet $LiHoF_4$ (see Fig. 1.1a for the phase diagram) is an ideal platform to address this issue. Indeed the Ising model is considered as an archetype both for the investigation of quantum criticality [6, 11, 12, 17] and for the evaluation of quantum simulators [18]. First, the hyperfine coupling strength of a Ho^{3+} ion is exceptionally large as coupling constant $A = 39$ mK [19, 20], promoting a strong hybridization or entanglement between the nuclear and electronic moments [16, 17, 21]. Second, the magnetic coupling between the Ho^{3+} ions that leads to ferromagnetic ordering at $T_c = 1.53$ K is predominantly through long-range dipole interactions $\mathcal{J}_D$ with strength in the order of 1 K, while nearest-neighbor exchange interaction is negligibly weak as $J_{ex} = -1.2$ mK [22]. This gives rise to the upper critical dimension $d^* = 3$ so that a mean-field approximation is accurate up to a logarithmic correction [23, 24, 16]. Third, applying a relatively small transverse field $H_c = 4.95$ T induces a zero-temperature QPT [16] driven by quantum fluctuations. Altogether $LiHoF_4$ represents a unique *nuclear-electronic quantum magnet* (Fig. 1.1b) [21], whose wavefunctions can be readily obtained by diagonalizing the Hamiltonian using the mean-field approximation.
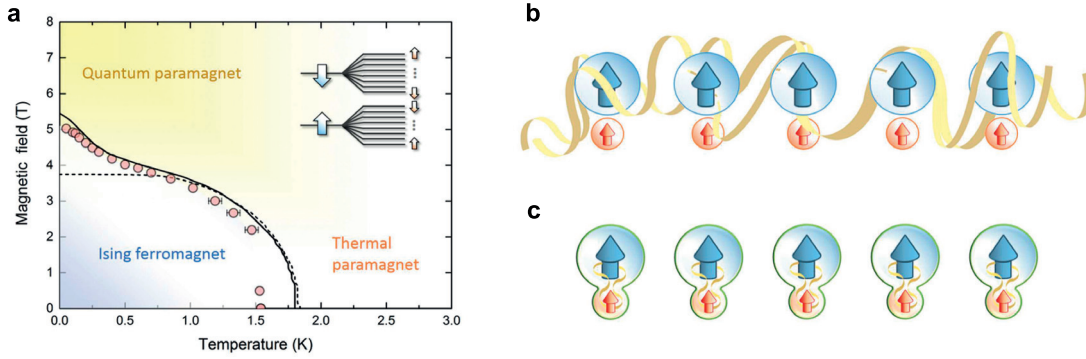
Figure 1.1: **a**) Phase diagram in LiHoF$_4$. Solid line represents a mean-field calculation taking into account strong hyperfine interaction in Ho ions, while dashed line is calculated in the absence of hyperfine interaction. Inset shows schematic energy levels for the Ising spins in an ordered phase (left) and its modification by hyperfine interactions with the nuclear spins (right). Experimental data taken from Bitko *et al.* [16]. **b**) Conceptual drawing of many-body nuclear-electronic system, where blue and red arrows represent electronic and nuclear moments, respectively, and wavy ribbon the entanglement. **c**) Entanglement from the many-body system encoded onto each nuclear-electronic hybrid in the mean-field model.

Using inelastic neutron scattering it was revealed that the collective electronic excitations in LiHoF$_4$ are incoherently coupled to the nuclear spin bath [17, 25]. The true QPT must therefore takes place in a hybridized nuclear-electronic state. In this thesis I develop a technique allowing to directly probe the entangled nature of electrons and nuclei using magnetic resonance schemes.

In order to guide and interpret our experimental investigation, first I perform a model calculation of the system. In the chapter 2, I establish and solve the Hamiltonian of the single Ho ion in the crystal field of LiHoF$_4$. By comparing the calculated energies of states as a function of magnetic field to the electron paramagnetic resonance measurements on LiHoF$_4$ I confirm that the Hamiltonian accurately describes the physical system. Hyperfine interaction is introduced to the single-ion Hamiltonian to show the effect of nuclear-electronic coupling on splitting of the electronic states. To model the ferromagnetic ordering of the system below critical temperature, I have to account for the dipolar interaction between the Ho ions. It is impossible to solve the many-body Hamiltonian so I introduce the concept of the mean-field approximation. The calculated mean-field states and energies are the foundation for calculating the expected dynamic susceptibility response of the system in the microwave frequency range. The linear response theory is then introduced as a formalism to calculate the excitations in the magnetic resonance experiment. This calculation is the foundation for interpreting our experimental data. Most of the theoretical work to date has focused on the static energy levels and phase diagram so these are the first calculations which describe the dynamical regime of the LiHoF$_4$ system. In the final section of the chapter 2 I show

original calculations of entanglement entropy in an interacting many-body system to get a deeper understanding of the quantum nature of the nuclear-electronic states, especially near quantum critical point, from the perspective of nuclear-electronic entanglement.

In the chapter 3 I describe the experimental setup which I developed to quantify hybridized nuclear-electronic states in the model transverse field Ising system LiHoF$_4$. I start by introducing the basic principles and detection techniques of magnetic resonance experiment. After that I explain the principles of operation of the dilution refrigerator which is necessary to access the low temperature physics where nuclear-electronic entanglement starts to play an important role [26]. Finally, I describe how I built the magnetic resonance setup and thermally anchored it to the dilution refrigerator. I show how the experimental data is fitted in order to extract the resonant frequency and Q-factor which are related to real and imaginary part of the magnetic susceptibility, calculated in previous chapter.

Experimental results, both raw and analyzed, are shown in the chapter 4. The interpretation of the experimental data is given by comparing it to the calculations from chapter 2. Our experimental observation of the hybridization is remarkably well reproduced by the calculations based on parameters obtained from experiments probing three orders of magnitude higher energies. I demonstrate the realization of nuclear-electronic magnetic resonance in an interacting many-body system by probing directly the transitions between the nuclear-electronic states which could not be resolved in neutron scattering experiments.

In the following, I further aim to explore the observed hybridization of the nuclear-electronic states from the perspective of entanglement. Comparing the measured susceptibility to the calculated entanglement entropy I find that they behave remarkably similar across the quantum phase transition. I conclude that the extended entanglement present in the transverse-field Ising model may leave a signature on the nuclear-electronic states through hybridization and that having an access to the nuclear spin as an observer may open an interesting avenue towards experimental probes of many body entanglement.

2 Theoretical background and calculations

In this chapter a theoretical model for LiHoF$_4$ is introduced and using a mean-field approximation the hyperfine nuclear-electronic energy levels are calculated. The real and imaginary part of the frequency-dependent magnetic susceptibility is calculated within the linear response framework, using the mean-field wavefunctions and energy levels. Entanglement in vicinity of the quantum phase transition is studied by calculating entanglement entropy of the nuclear and electronic subsystems.

2.1 LiHoF$_4$

The crystal structure of LiHoF$_4$ is tetragonal and belongs to the space group $I4_1/a$, n°88 in the International Tables for Crystallography [28] (Scheelite structure) with lattice constants $a = b = 5.175$ Å and $c = 10.75$ Å. The magnetic moments are carried by the rare earth ions, whose positions in the unit cell are shown in Fig. 2.1. The conventional unit cell contains 4 rare earth ions.

In LiHoF$_4$ the Ho^{3+} ions have a partially filled outermost $4f$ shell with 10 electrons. By applying the Hund′s rules we find that the ground state electronic configuration of a single Ho^{3+} ion is $^5I_8$ ($J = 8, L = 6, S = 2$). The effective magnetic moment $\mu_{eff} = g\mu_B\sqrt{J(J+1)}$ is $\mu_{eff} = 10.6\mu_B$. In the absence of a crystalline electric field, the ground state is (2J+1)=17-fold degeneracy. The lowest excited state of the configuration $^5I_7$ is 7400 K above, so it is not in the range of temperatures of interest discussed here [29].

2.1.1 Crystal field

If we include the Coulomb interaction of the Ho^{3+} ion with the surrounding Li$^+$ and F$^-$ ions, the degeneracy of the electron orbital states is broken due to the static electric field produced by the surrounding charge distribution (surrounding ions). Therefore,
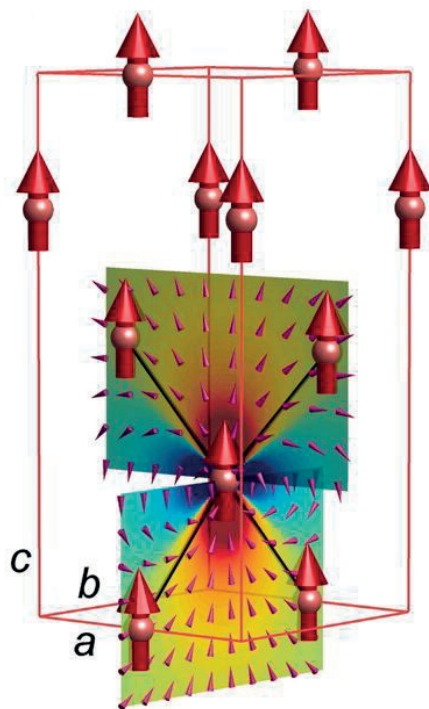
Figure 2.1: The crystal and magnetic structure of $LiHoF_4$ in the ferromagnetic phase. The magnetic moments of the Ho ions in the ordered phase are along the c-axis. The dipole field from the central moment yields the ferromagnetic (red scale) and antiferromagnetic (blue scale) coupling. The sign and the strengths of the coupling depend on the direction of the moments. After Ref. [27].

this electric field depends heavily on the spatial symmetry of the crystal. The derivation of the crystal-field electrostatic potential takes into account the lattice symmetry, and is most simply expressed in terms of operators called the operator equivalents. The details of the derivation can be found in Hutchings [30]. The operator equivalents are operators built out of the **J** operators that act on a 2J+1 dimensional space.The operators act only on the angular part of the wave function of the coupled system, and the matrix elements of the radial part of the wave function are usually incorporated in the fitting parameters. The number of the operators needed to define the crystal field Hamiltonian $\mathcal{H}_{CF}$, and rules for deriving them, is determined by the spatial symmetry of the crystal and the ground state configuration of the ion. These rules are clearly explained by Stevens [31, 32].

The LiHoF_4 crystal has the S$_4$ point group symmetry, which partially splits the 17-fold degeneracy. The ground state of the crystal-field Hamiltonian is a doublet, which is a non-Kramers degenerate ground state. The S$_4$ point group symmetry of the Ho-ion surroundings in the Scheelite lattice of LiHoF_4 implies that the relevant Stevens operators are:

$$
\begin{aligned}
O_2^0 &= 3J_z^2 - J(J+1), \\
O_4^0 &= 35J_z^4 - 30J(J+1)J_z^2 + 25J_z^2 - 6J(J+1) + 3J^2(J+1)^2, \\
O_4^4(c) &= \frac{1}{2}(J_+^4 + J_-^4), \\
O_6^0 &= 231J_z^6 - 315J(J+1)J_z^4 + 735J_z^4 + 105J^2(J+1)^2J_z^2 \\
&\quad - 525J(J+1)J_z^2 + 294J_z^2 - 5J^3(J+1)^3 + 40J^2(J+1) - 60J(J+1), \\
O_6^4(c) &= \frac{1}{4}(J_+^4 + J_-^4)[11J_z^2 - J(J+1) - 38] + \text{H.c.}, \\
O_6^4(s) &= \frac{1}{4i}(J_+^4 - J_-^4)[11J_z^2 - J(J+1) - 38] + \text{H.c.},
\end{aligned}
\tag{2.1}
$$

where $J_+ = J_x + J_y$ and $J_- = J_x - J_y$. Using these operators, the crystal field Hamiltonian $\mathcal{H}_{CF}$ can be written as

$$
\mathcal{H}_{CF} = B_2^0 O_4^0 + B_4^0 O_4^0 + B_6^0 O_6^0 + B_4^4(c)O_4^4(c) + B_6^4(c)O_6^4(c) + B_6^4(s)O_6^4(s). \tag{2.2}
$$

The x-axis can be chosen arbitrarily. The coordinate system was rotated around the crystal symmetry z-axis so that the parameter $B_4^4(s)$ vanishes (removing the additional $O_4^4(s)$ term which would otherwise be present) and $B_4^4(c)$ is positive.

Although it is possible to calculate the crystal field parameters B_m^l in point-charge approximation, where the surrounding ions are considered as an array of point charges, the accuracy of these calculations is rarely acceptable. The crystal field parameters are

Table 2.1: Crystal-field parameters in units of meV. The set of parameters are the same for all four Ho sublattices. The sign of $10^5 B_6^4(s)$ is undetermined, not arbitrary, and depends on the chosen fluoride basis.

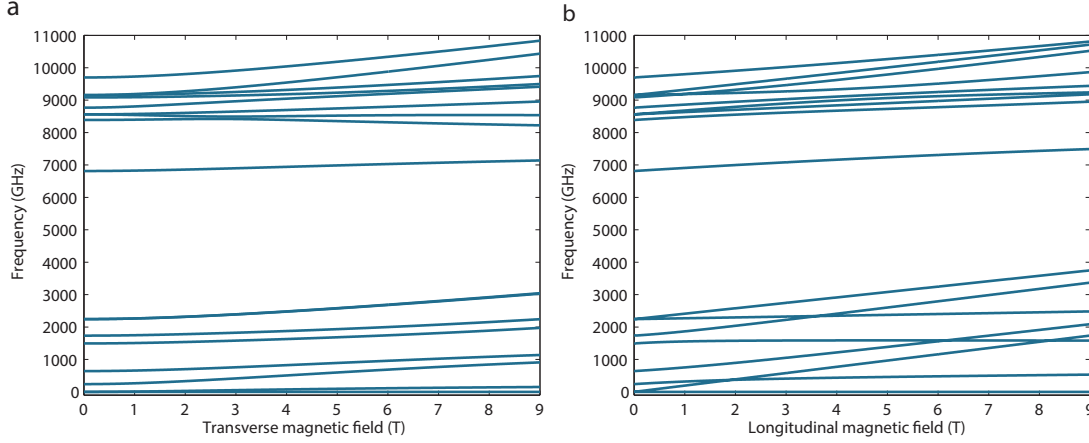| B_2^0	$10^3 B_4^0$	$10^3 B_4^4$	$10^5 B_6^0$	$10^5 B_6^4(c)$	$10^5 B_6^4(s)$
-0.06	0.35	3.6	0.04	7.0	± 0.98

Figure 2.2: Calculated crystal field energy levels as a function of **a**) the transverse and **b**) longitudinal magnetic field.

extracted by fitting the crystal field spectrum. The values of the crystal field parameters were obtained by fitting the c-axis field dependence of the three lowest crystal-field levels to the observed electron paramagnetic resonance data [20]. In the calculations we have used the crystal field parameters refined by Rønnow *et al.* [22] shown in the table 2.1.

2.1.2 Magnetic field effects

We diagonalised the crystal field Hamiltonian which resulted in 17 electronic eigenstates and eigenvalues, shown in Fig. 2.2. The ground state at the zero-field is a doublet and the first excited state is 11 K above it. The ground state doublet is followed by 4 singlet states and again a doublet state.

By diagonalizing the crystal field Hamiltonian $\mathcal{H}_{CF}$ and the Zeeman term $\mathcal{H}_Z$,

$$\mathcal{H} = \mathcal{H}_{CF} + \mathcal{H}_Z \quad , \quad \mathcal{H}_Z = g_L \mu_B \mathbf{J} \cdot \mathbf{H}$$

were g_L (Lande factor) = 1.250 and μ_B is the Bohr magneton, we track the electronic states as a function of the transverse magnetic field along the a-axis (Fig. 2.2a) and the
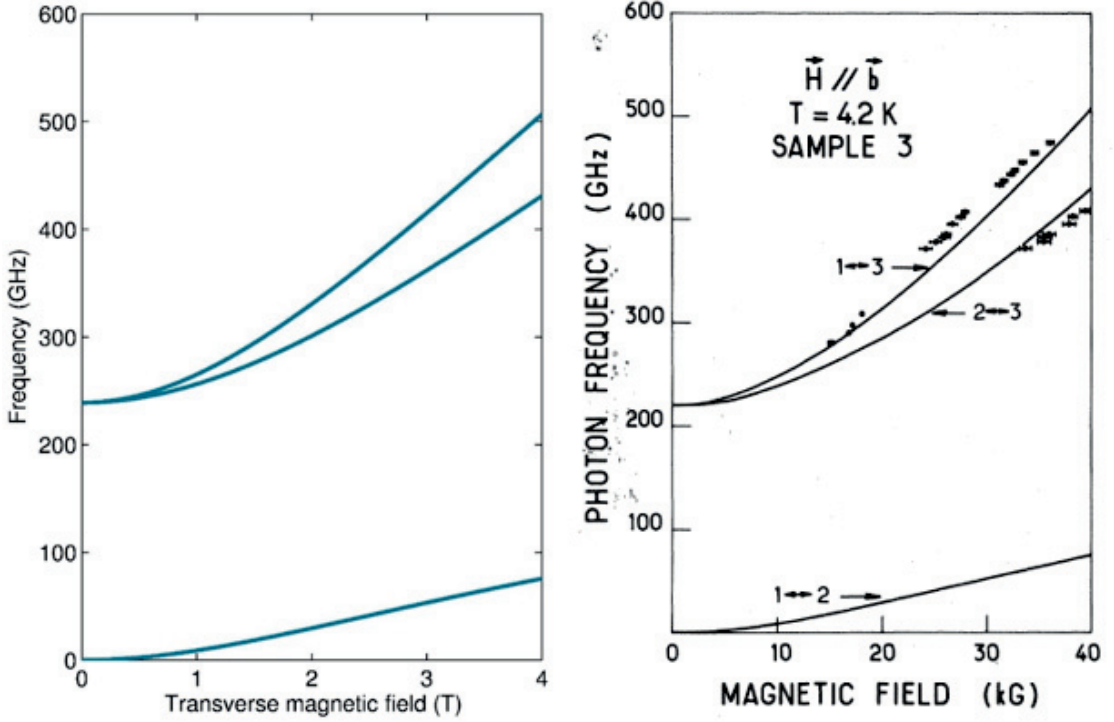
Figure 2.3: **a**) Calculated transitions between the 3 lowest crystal field levels as a function of the transverse magnetic field. **b**) Experimental EPR transitions measured by Magarino *et al.* [20].

longitudinal magnetic field along the c-axis (Fig. 2.2b). The ground state doublet is split when the transverse field is applied. The transverse field is effectively mixing the excited states into the ground state.

To compare our calculations with the experiment we calculated transitions between the 3 lowest crystal field levels as a function of the transverse magnetic field (Fig. 2.3a) and transition between 4 lowest levels as a function of longitudinal field (Fig. 2.4a), and show it alongside the electron paramagnetic resonance (EPR) measurements from Magarino *et al.* [20] (Fig. 2.3b, Fig. 2.4b). We see that the transitions between different electronic states measured by EPR agree with the diagonalization of the crystal-field Hamiltonian.

Diagonalizing the $\mathcal{H}_{CF}$ shows that the lowest excited state in the spectrum is the singlet state lying 11 K above the ground state doublet. At temperatures lower than this gap, only the ground state doublet is significantly populated, and low temperature physics can be captured by using a two state system. The two degenerate states, $|\alpha\rangle$ and $|\beta\rangle$ can be chosen in a way that $\langle\alpha|J_z|\beta\rangle = 0$ and $\langle\alpha|J_z|\alpha\rangle = -\langle\beta|J_z|\beta\rangle$. We identify the two degenerate states as $|\uparrow\rangle$ and $|\downarrow\rangle$. If we consider only the low temperatures, LiHoF$_4$ Hamiltonian can be reduced to a transverse field Ising model with pseudo-spin-$\frac{1}{2}$
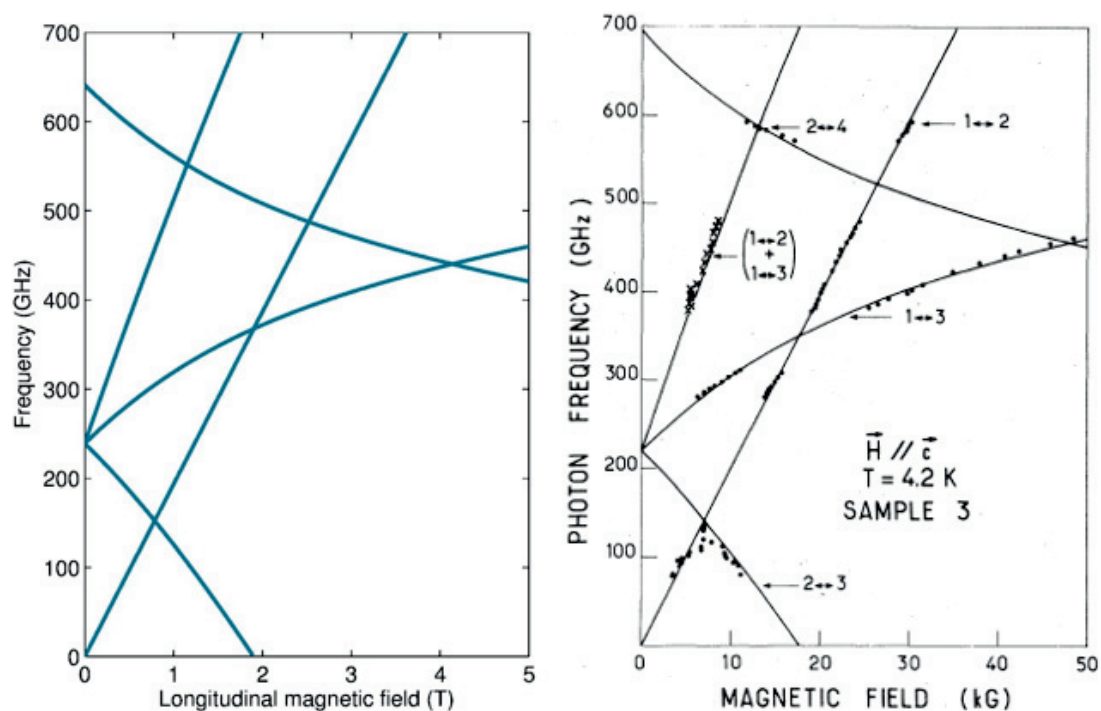
Figure 2.4: **a**) Calculated transitions between the 4 lowest crystal field levels as a function of the longitudinal magnetic field. **b**) Experimental EPR transitions measured by Magarino *et al.* [20].

degrees of freedom. Considerable work was carried out on LiHoF$_4$, based on Monte Carlo simulations in order to elucidate a spin glass phase [29, 33, 34]. Most of that work was performed on a reduced rare earth Hamiltonian.

The two lowest Ising states are formed from the odd J_z eigenstates, such that $|\uparrow\rangle = \{|-5\rangle, |-1\rangle, |3\rangle, |7\rangle\}$ and $|\downarrow\rangle = \{|-7\rangle, |-3\rangle, |1\rangle, |5\rangle\}$. We see that J_x cannot couple directly between the two lowest lying states, therefore, applying the transverse external field H_x, which couples to J_x via Zeeman term $g_L\mu_B J_x H_x$ alone is not enough to mix $|\uparrow\rangle$ and $|\downarrow\rangle$. We need at least 1st excited state (at 11 K) which consists of $\{|-6\rangle, |-2\rangle, |2\rangle, |6\rangle\}$, which can be mixed with the ground states by J_x when applying H_x, to make the $\langle\uparrow |J_x| \downarrow\rangle = \langle\downarrow |J_x| \uparrow\rangle$ matrix element non-zero, to have non-zero energy splitting $g_L\mu_B J_x H_x$. Since $\langle\uparrow |J_x| \downarrow\rangle$ is proportional to H_x, the energy splitting between the two lowest levels is proportional to H_x squared at low fields (as shown by 1↔2 transition in Fig. 2.3).

The two lowest states are no longer pure Ising states as we apply the transverse magnetic field, because the higher states are mixed into the new lowest states. In the following, we shall treat the full rare-earth Hamiltonian, including all 17 electronic states, not the effective Ising model.

2.1.3 Hyperfine interaction

So far we considered the Hamiltonian with a crystal field and Zeeman interaction. But in case of LiHoF$_4$ a hyperfine interaction between Holmium electrons and Holmium nuclei is so strong that at low temperatures it affects the electronic phase diagram [26].

The hyperfine coupling of a single Ho atom with its own $I = 7/2$ nuclear spin gives the term

$$\mathcal{H}_{Hyp} = A\,\mathbf{J}\cdot\mathbf{I} \tag{2.3}$$

The hyperfine constant in LiHoF$_4$, $A = 3.36\,\mu$eV, has been determined by the hyperfine resonance [20] and heat capacity measurements [19].

Let us consider the simple case in which there is only the crystal field, Zeeman splitting, and we add the hyperfine term to the Hamiltonian

$$\mathcal{H} = \sum_i [\mathcal{H}_{CF} + A\mathbf{J}_i\cdot\mathbf{I}_i - g_L\mu_B\mathbf{J}_i\cdot\mathbf{H}] \tag{2.4}$$

The hyperfine coupling additionally splits each crystal field level into $(2I+1)=8$ hyper-
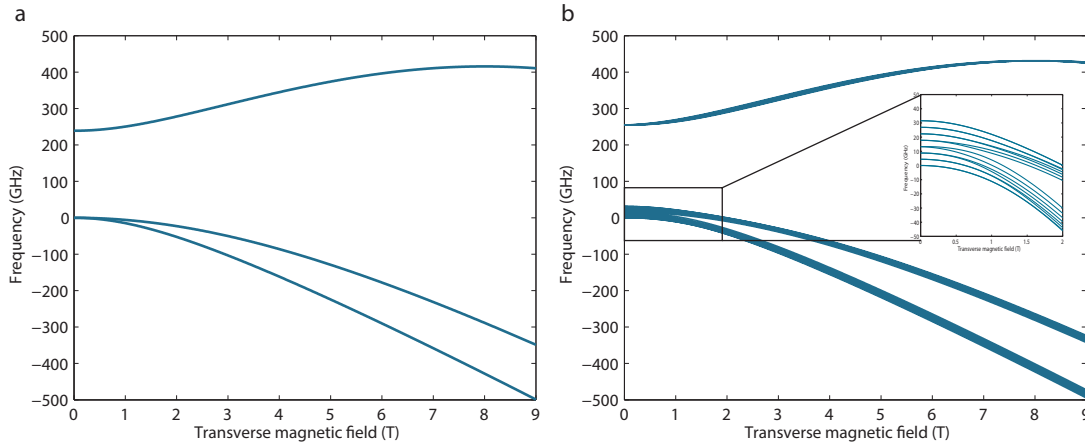
Figure 2.5: **a**) Lowest 3 energy levels split into 24 levels when hyperfine interaction is included **b**). Inset in **b**) shows splitting of the doublet at low fields.

Figure 2.6: Lowest nuclear-electronic states of the electronic doublet split by the hyperfine interaction. After M. Schechter and P. C. E. Stamp [21].

fine states, making it (17·8)=136 nuclear-electronic levels in total. In Fig. 2.5 we show how the lowest 3 electronic states are split into 24 nuclear-electronic states. If we take a closer look (Fig. 2.5b inset) we see that we have 8 hyperfine levels at the zero-field. The magnetic field breaks the degeneracy and splits each energy level into two.

One can think of this lowest 8 energy levels in zero-field states as 16 double degenerate states with 8 different nuclear spin quantum numbers (-7/2 to 7/2), where each of them has one of the two original electron spin states, $|\uparrow\rangle$ and $|\downarrow\rangle$ (Fig. 2.6). Nuclear and electronic spin angular momenta is aligned along the crystallographic c-direction in the zero-field, but this is no longer true when the transverse field is applied. When a transverse field is applied, states can no longer be considered as separable nuclear and electronic states, but rather as mixed nuclear-electronic states. At high magnetic fields they can be treated as separable states again.

To excite some of the particles from the lower to higher energy state one would need an oscillating magnetic field tuned to the energy equal to the difference between energy levels. That is exactly what we want to do in our magnetic resonance experiment, so we have calculated the energy difference between states as a function of the transverse magnetic field. The nuclear magnetic resonance (NMR) excitations which change nuclear spin quantum number by 1, $\Delta m_N = 1$, and preserve the electron spin quantum
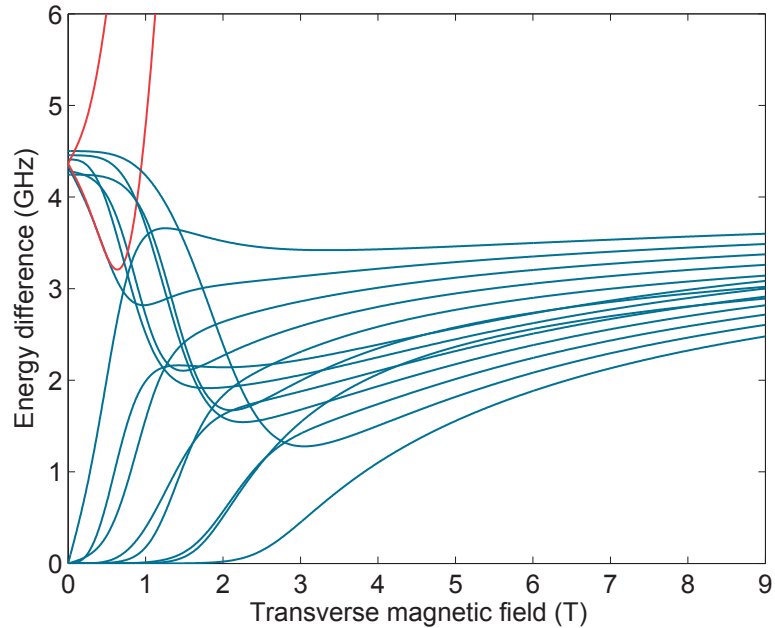
Figure 2.7: Calculated energy difference between subsequent states or NMR transitions (blue) and EPR transitions (red).

number, $\Delta m_S = 0$, are shown by blue lines in Fig. 2.7. The electronic paramagnetic resonance (EPR) excitations between spin up and spin down state, which preserves the nuclear spin quantum number, are shown by the red lines.

The hyperfine interaction $\mathcal{H}_{Hyp} = AJ \cdot I$ splits the lowest doublet states to an eightfold multiplet of nearly equidistant levels. The energy difference between the nuclear-electronic states is approximately 4.5 ± 0.2 GHz at the zero-field and it gets smaller as the field is increased and the states are more mixed. These states are not equidistant because mixed nuclear-electronic states cannot be written as a product state of the electronic and nuclear state. Nevertheless, to a first approximation and in the zero field, we can think of the nuclear-electronic states as the product of electronic and nuclear states.

2.2 Mean-field theory

So far we have considered only the single-ion part of the Hamiltonian, which has contribution from the crystal field, the Zeeman coupling, and the hyperfine coupling, but there is also interaction between the Ho^{3+} ions which is dominated by the long-

range dipole coupling, with a small nearest neighbour exchange interaction:

$$
\begin{aligned}
\mathcal{H} &= \sum_i [\mathcal{H}_{\mathrm{CF}}(\mathbf{J}_i) + A\mathbf{J}_i \cdot \mathbf{I}_i - g_L \mu_{\mathrm{B}} \mathbf{J}_i \cdot \mathbf{H}] \\
&\quad - \frac{1}{2} \sum_{ij} \sum_{\alpha\beta} \mathcal{J}_{\mathrm{D}} \overline{\overline{D}}_{\alpha\beta} \mathbf{J}_{i\alpha} \mathbf{J}_{j\beta} - \frac{1}{2} \sum_{ij,n.n.} \mathcal{J}_{\mathrm{ex}} \mathbf{J}_i \cdot \mathbf{J}_j \, .
\end{aligned}
\tag{2.5}
$$

It is relatively easy to solve a single-body problem by diagonalizing the Hamiltonian. Difficulty arises when the considering interaction Hamiltonian, because the size of Hamiltonian increases as $N!$, where N is the number of particles. The primary motivation of a mean-field approximation is to reduce the $N-$body Hamiltonian to a single-body Hamiltonian. The mean-field theory replaces interactions between various ions by an interaction between a single ion with a self-consistent field, neglecting the fluctuations of moments around their equilibrium position.

Dipolar interactions are long-range pair interactions, therefore all the pairs of moments in the lattice should be taken into account in $\mathcal{H}_{\mathrm{dip}}$:

$$
\mathcal{H}_{\mathrm{dip}} = -\frac{1}{2} \sum_{ij} g_{Li} g_{Lj} \mu_{\mathrm{B}}^2 \mathbf{J}_i D_{ij} \mathbf{J}_j
\tag{2.6}
$$

where D_{ij} is the matrix for the dipole-dipole interaction between sites i and j. D_{ij} can be derived from the classical dipole-dipole interaction:

$$
D_{\mathrm{ij}} = \frac{\mu}{4\pi} \left(\frac{3 r_{ij} r_{ij}^T}{||r_{ij}||^5} - \frac{\delta_{ij}}{||r_{ij}||^3} \right) .
\tag{2.7}
$$

In the mean-field approximation the fluctuations of moments around their equilibrium positions are neglected, J_i is replaced in the $\mathcal{H}_{\mathrm{dip}}$ by $(J_i - \langle J_i \rangle) + \langle J_i \rangle$, where $(J_i - \langle J_i \rangle)$ is the fluctuation term which is considered small. The second order terms are neglected and constant is removed. Since $D_{ij} = D_{ji}$ and D_{ij} is symmetric

$$
\mathcal{H}_{\mathrm{dip}}^{MF} = -\sum_{ij} g_{Li} g_{Lj} \mu_{\mathrm{B}}^2 \mathbf{J}_i D_{ij} \langle J_j \rangle .
\tag{2.8}
$$

The effective mean field can be introduced

$$\mathbf{h}_{\text{eff}}^i = \sum_j \tilde{D}_{ij} \mu_\mathrm{B} g_{Lj} \langle J_j \rangle, \tag{2.9}$$

where the i index varies from 1 to 4, for the 4 sites in the unit cell. The $\tilde{D}_{ij}$ matrices are defined by

$$\tilde{D}_{ij} = \frac{N}{V} \left(\frac{4\pi}{3} + \sum_{cells} D_{ij} - \mathcal{N}_{ij} \right) \tag{2.10}$$

The first term is the Lorentz factor, the second term is the sum of the D_{ij} matrices calculated for a large number of unit cells inside a sphere of 80 cells radius, and the third term is the demagnetization factor.

A demagnetization field depends on the geometry of a sample and most of the time is not uniform. If a sample is ellipsoid-shaped, the demagnetizing field is linearly related to the magnetization and the proportionality factor $\mathcal{N}$ is the demagnetization factor, which is a diagonal tensor in the basis of principal axes of the ellipsoid. This tensor has two general properties: it is symmetric and its trace is 1. For a non-ellipsoidal body, the demagnetization factor is not uniform inside the sample, even if there is only one magnetic domain in the sample.

Our sample is cube shaped, but magneto-optic Kerr effect images [35] and scanning Hall probe microscope imaging of our cubic $LiHoF_4$ sample [36] show that magnetic domains are needle shaped along the c-axis due to the strong anisotropy. We calculated the critical field, H_C, in $LiHoF_4$ at 0.15 K with demagnetization factors for the three different sample body types: for a needle-shaped body $H_C = 4.9$ T, for an egg-shaped body $H_C = 3.5$ T and for a sphere- or cube-shaped body $H_C = 2.2$ T. Since our susceptibility measurements with the cubical sample show that the critical field at 0.15 K is 4.8 T, we used the demagnetization factor for needle-shape body in our calculations.

Finally, we can express the dipolar $\mathcal{H}_{\text{dip}}^{MF}$ in terms of the effective mean field $\mathbf{h}_{\text{eff}}$

$$\mathcal{H}_{\text{dip}}^{MF} = \sum_{i=1}^4 g_{Li} \mu_\mathrm{B} \mathbf{J}_i \cdot \mathbf{h}_{\text{eff}}^i. \tag{2.11}$$

The Heisenberg exchange interaction can also be calculated in the mean-field approxi-

mation as

$$\mathcal{H}_{\text{ex}}^{MF} \quad = \quad \sum_{i,j} \mathcal{J}_{\text{ij}} \mathbf{J}_i \cdot \langle J_j \rangle \qquad\qquad (2.12)$$

which, if taking only the closest neighbours interaction into account, becomes

$$\mathcal{H}_{\text{ex}}^{MF} \quad = \quad \sum_{\langle i,j \rangle} \mathcal{J}_{12} \mathbf{J}_i \cdot \langle J_j \rangle. \qquad\qquad (2.13)$$

The value for the anti-ferromagnetic exchange coupling was fitted by H. M. Rønnow *et al.*, finding a value of $\mathcal{J}_{12} = -\,0.1\ \mu$eV [26].

The mean-field approximation neglects second order fluctuation terms, which implies that it neglects the two ion correlation, leading to $\langle J_i J_j \rangle = \langle J_i \rangle \langle J_j \rangle$. The variables J_i and J_j are therefore independent in the mean-field approximation. Which is not the case in real system LiHoF$_4$. This has important consequences when the correlation length is large, at the phase transition where correlation length goes to infinity. Furthermore, as the fluctuations increase at the transition, the behaviour of the system around the transition cannot be accurately described by this mean field approximation. It is a well-known fact that mean-field theory in general overestimates the transition temperature and the critical transverse magnetic field, because the fluctuations are neglected. To compensate for the effects of the fluctuations we renormalized the moment along the c-axis by a renormalization factor of 1.3, calculated in the effective-medium theory to the first order in the $1/z$ expansion by Rønnow *et al.* [22].

Once this Hamiltonian is established, the calculation which computes the values only in the unit cell is as follows:

1. The matrices $\tilde{D}_{ij}$ are computed once at the beginning.

2. The moments $\langle J_i \rangle$ are initialized in a given arbitrary configuration.

3. The mean fields $\mathbf{h}_{\text{eff}}^i$ are computed from the current configuration of the moments

4. The mean field hamiltonian $\mathcal{H}_{\text{i}}^{MF} = \mathcal{H}_{\text{CF}}^i + \mathcal{H}_{\text{Zeeman}}^i + \mathcal{H}_{\text{Hyp}}^i + \mathcal{H}_{\text{dip}}^{iMF} + \mathcal{H}_{\text{ex}}^{iMF}$ is diagonalized for each site.

5. The means moments $\langle J_i \rangle$ are updated by computing the thermal average from the eigenvalues and eigenvectors of $\mathcal{H}_{\text{i}}^{MF}$.

6. The difference between new and old $\langle J_i \rangle$ is evaluated and compared to a convergence threshold 10^{-6}. If the difference is larger than the threshold, the algorithm
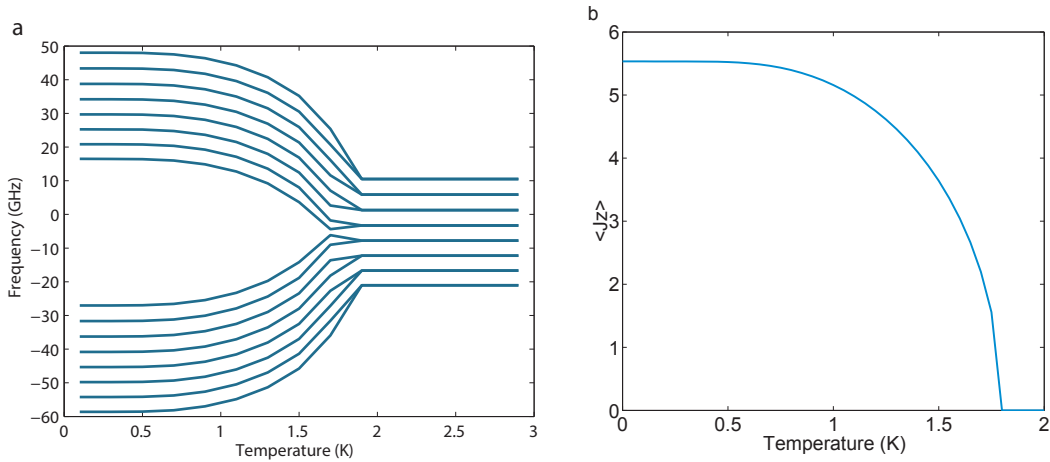
Figure 2.8: **a**) Temperature dependence of the lowest 16 energy levels at the zero-field. **b**) $\langle J_z \rangle$ as a function of temperature.

returns to the third step. This procedure is repeated until the convergence is satisfied.

We carried out calculations in the mean-field approximation while considering the full rare-earth Hamiltonian with 136 nuclear-electronic states. The calculated critical temperature is $T_C = 1.8$ K (experimental $T_C = 1.53$ K) and the critical transverse field $H_C = 5.4$ T.

Figure 2.8 shows the evolution of energies of the 16 lowest states as we decrease the temperature below the T_C. The doublet splits because the mean field increases due to the ferromagnetic ordering as the temperature is decreased below T_C.

When the temperature is lowered below T_C, the spins order in the c-direction, which results in the mean field along the c-direction. This field removes the degeneracy of the doublet. The mean field increases with the decrease in temperature splitting the doublet even more. The difference between the hyperfine energy levels is intact, it is the same 4.5 GHz at 0.1 K as it was in the ordered state.

The evolution of the energies of the 16 lowest states at 0.1 K was calculated as a function of the transverse magnetic field from 0 to 9 T (Fig. 2.9).

Now that we have seen what happens to the energy levels when we cool down to 0.1 K, we calculate how they evolve with the applied transverse field at 0.1 K (Fig. 2.9). The transverse field separates the two sets of states even further and mixes the higher energy states into $|\uparrow\rangle$ and $|\downarrow\rangle$ states, which become more mixed.

We are particularly interested in the difference between the energy levels because that is the most relevant for the magnetic resonance experiments which we carried out.
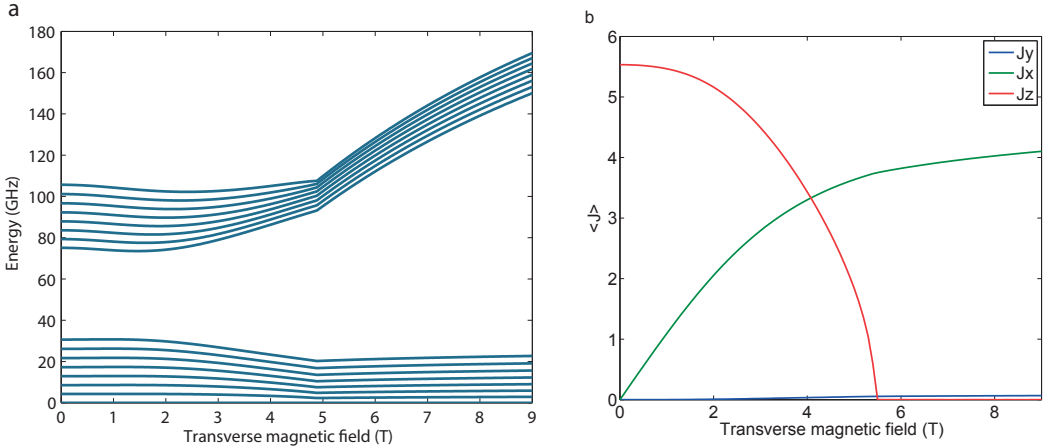
Figure 2.9: **a**) Field dependence of the lowest 16 energy levels at 0.1 K calculated in mean-field aproximation. **b**) $\langle J_z \rangle$ and $\langle J_x \rangle$ as a function of the transverse field.
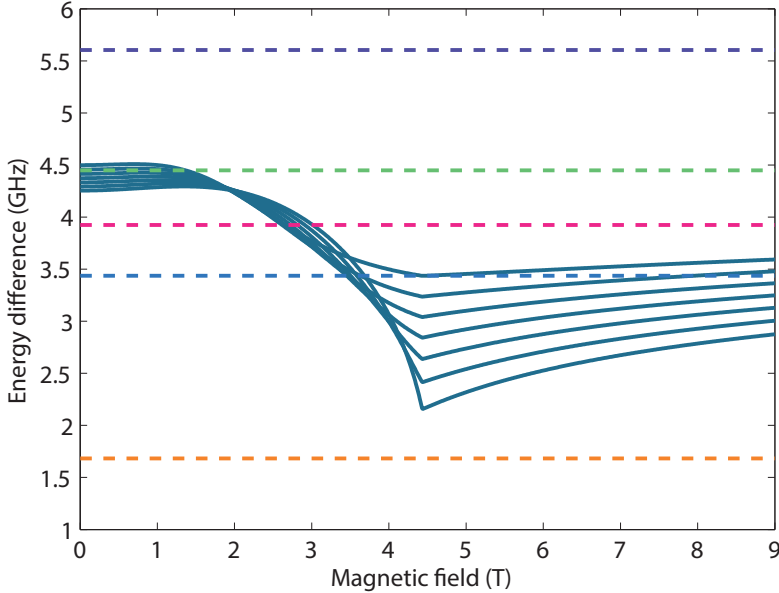

Figure 2.10: Field dependence of difference in energy between lowest 8 states at 0.1 K.

We show the difference between the hyperfine energy levels as a function of the field in Fig. 2.10. Only the 8 lowest states are considered because the higher states are not significantly populated at the low temperatures at which the experiment is performed.

The differences between the energy levels become smaller until it reaches the minimum value at the critical field H_C. After that, the difference in energy increases with field and finally saturates at high field. The difference between the energy levels is dominated by the hyperfine term $A\langle J \rangle$. $A\langle J_Z \rangle$ is getting smaller with the increase of the transverse magnetic field (Fig. 2.9b) while $A\langle J_X \rangle$ is increasing. Total $A\langle J \rangle$ has a minimum at the quantum phase transition, and so does the difference in energy (Fig. 2.10). With experimental setup we shall probe the system at five fixed frequencies noted with different colours in Fig. 2.10. The magnetic resonance condition should be satisfied at frequencies and fields where the frequency of excitation field is equal to the difference between the energy levels.

2.3 Linear response theory

To calculate the actual response of the system to a small external perturbing oscillating magnetic field, we have calculated the susceptibility in the linear response theory framework. Before calculating the response of our system, let us first introduce the concept of the linear response theory as reported by J. Jensen and A. R. Mackintosh [37].

A response function for a macroscopic system relates the change of an ensemble-averaged physical quantity $\langle \mathbf{B}(t) \rangle$ to an external force $f(t)$. In our case, $\mathbf{B}(t)$ is the angular momentum of an ion or the magnetization and $f(t)$ is a time-dependent applied magnetic field. We shall only consider the regime where $\langle \mathbf{B}(t) \rangle$ changes linearly with the force $f(t)$, hence the name linear response theory. We suppose that $f(t)$ is sufficiently weak to ensure that the response is linear. We shall check that this condition is satisfied when performing the experiment. We assume that the system is in the thermal equilibrium before the external force is applied.

A system in thermal equilibrium is characterized by the density operator

$$\rho_0 = \frac{1}{Z} e^{-\beta \mathcal{H}_0} \qquad ; \qquad Z = \text{Tr } e^{-\beta \mathcal{H}_0}, \tag{2.14}$$

where $\mathcal{H}_0$ is the (effective) Hamiltonian, Z is the (grand) partition function, and $\beta = 1/k_B T$. Since we are only interested in the linear part of the response, we may assume that the weak external disturbance $f(t)$ gives rise to a linear time-dependent

perturbation in the total Hamiltonian $\mathcal{H}$:

$$\mathcal{H}_1 = -\mathbf{A}f(t) \qquad ; \qquad \mathcal{H} = \mathcal{H}_0 + \mathcal{H}_1, \tag{2.15}$$

where $\mathbf{A}$ is a constant quantum operator.

In the magnetic resonance experiment the z-axis is defined parallel to the crystallo-graphic c-axis long which the electronic spins are aligned in the ferromagnetic phase. The static transverse magnetic field which drives the quantum phase transition is applied along the x-axis which is parallel to the crystallographic a-axis. The oscillating magnetic field which acts as an external force f(t) is applied along the y-axis to ensure that it is always perpendicular to $\langle J \rangle$, which is along the z-axis in the ferromagnetic phase (at the zero-field) or along the x-axis in the quantum paramagnetic phase. Thus, $\mathcal{H}_1$ is the Zeeman term $\mathcal{H}_1 = -g_L \mu_B J_y H_y(t)$, so that $\mathbf{A} = J_y$ and $f(t) = g_L \mu_B H_y(t)$.

As a consequence of this perturbation, the density operator $\rho(t)$ becomes time-dependent and so also does the ensemble average of the operator $\mathbf{B}$:

$$\langle \mathbf{B}(t) \rangle = \mathrm{Tr}\{\rho(t)\mathbf{B}\}. \tag{2.16}$$

The linear equation between this quantity and the external force has the form

$$\langle \mathbf{B}(t) \rangle - \langle \mathbf{B} \rangle = \int_{-\infty}^{t} \phi_{BA}(t - t')f(t')dt', \tag{2.17}$$

Where ϕ_{BA} is the response function. The differential change of $\langle \mathbf{B}(t) \rangle$ is proportional to the external disturbance $f(t')$ and the duration of the perturbation delta t'. Equation 2.17 can be Fourier transformed into

$$\langle \mathbf{B}(\omega) \rangle = \chi_{BA}(\omega)f(\omega), \tag{2.18}$$

$\chi_{BA}(\omega)$ is called the frequency-dependent susceptibility and is the Fourier transform of the response function $\phi_{BA}(t)$.

We shall deduce the expression for the response function $\phi_{BA}(t)$ in the term of the operators $\mathbf{B}$ and $\mathbf{A}$ and the unperturbed Hamiltonian $\mathcal{H}_0$. Instead of the Schrodinger picture we adopt the Heisenberg picture, so that the wave functions are independent of time, while the operators become time-dependent. In the Heisenberg picture the

operators are

$$\mathbf{B}(t) = e^{i\mathcal{H}t/\hbar}\mathbf{B}e^{-i\mathcal{H}t/\hbar}, \tag{2.19}$$

While the corresponding equation of motion is

$$\frac{d}{dt}\mathbf{B}(t) = \frac{i}{\hbar}[\mathcal{H}, \mathbf{B}(t)]. \tag{2.20}$$

The equation of motion derived for the density operator in the Schrodinger picture is similar to the Heisenberg equation of motion above, except for the change of the sign in front of the commutator

$$\frac{d}{dt}\rho(t) = -\frac{i}{\hbar}[\mathcal{H}, \rho(t)]. \tag{2.21}$$

The density operator may be written as the sum of the two terms

$$\rho(t) = \rho_0 + \rho_1(t) \quad \text{with} \quad [\mathcal{H}_0, \rho_0] = 0, \tag{2.22}$$

where ρ_0 is the density operator of the thermal-equilibrium state which, by definition, must commute with $\mathcal{H}_0$. $\rho_1(t)$ is time-dependent change due to the perturbation.

It can be easily derived (details can be found in Ref. [37]) that, to first order order in the external perturbations, the time-dependent density operator is

$$\rho(t) = \rho_0 + \frac{i}{\hbar}\int_{-\infty}^{t}[\mathbf{A}_0(t' - t), \rho_0]f(t')dt', \tag{2.23}$$

where

$$\mathbf{A}_0(t) = e^{i\mathcal{H}_0t/\hbar}\mathbf{A}e^{-i\mathcal{H}_0t/\hbar}. \tag{2.24}$$

This determines the time dependence of **B** as

$$\langle \mathbf{B}(t) \rangle - \langle \mathbf{B} \rangle = \text{Tr}\{(\rho(t) - \rho_0)\mathbf{B}\}$$

$$= \frac{i}{\hbar}\text{Tr}\left\{\int_{-\infty}^{t}[\mathbf{A}_0(t' - t), \rho_0]\mathbf{B}f(t')dt'\right\}$$

$$= \frac{i}{\hbar}\int_{-\infty}^{t}\text{Tr}\{\rho_0[\mathbf{B}, \mathbf{A}_0(t' - t)]\}f(t')dt'$$

$$= \frac{i}{\hbar}\int_{-\infty}^{t}\langle[\mathbf{B}_0(t), \mathbf{A}_0(t')]\rangle_0 f(t')dt'.$$

A comparison of this result with the definition of the response function gives

$$\phi_{BA}(t - t') = \frac{i}{\hbar}\langle[\mathbf{B}(t), \mathbf{A}(t')]\rangle. \tag{2.25}$$

This expression is called the Kubo formula for the response function.

If the eigenvalues E_α and the corresponding eigenstates $|\alpha\rangle$ for the Hamiltonian $\mathcal{H}_0$ are known, it is possible to derive an explicit expression for the response function and for frequency-dependent susceptibility.

$$K_{BA}(t) = \frac{i}{\hbar}\frac{1}{Z}\text{Tr}\left\{e^{-\beta\mathcal{H}}[e^{i\mathcal{H}t/\hbar}\mathbf{B}e^{-i\mathcal{H}t/\hbar}, \mathbf{A}]\right\}$$

$$= \frac{i}{\hbar}\frac{1}{Z}\sum_{\alpha\alpha'}e^{-\beta E_\alpha}\left\{e^{iE_\alpha t/\hbar}\langle\alpha|\mathbf{B}|\alpha'\rangle e^{-iE_{\alpha'}t/\hbar}\langle\alpha'|\mathbf{A}|\alpha\rangle - \langle\alpha|\mathbf{A}|\alpha'\rangle e^{iE_{\alpha'}t/\hbar}\langle\alpha'|\mathbf{B}|\alpha\rangle e^{-iE_\alpha t/\hbar}\right\}.$$

Interchanging α and α' in the last term, and introducing the population factor

$$n_\alpha = \frac{1}{Z}e^{-\beta E\alpha} \quad ; \quad Z = \sum_{\alpha'}e^{-\beta E\alpha'}, \tag{2.26}$$

we get

$$K_{BA}(t) = \frac{i}{\hbar}\sum_{\alpha\alpha'}\langle\alpha|\mathbf{B}|\alpha'\rangle\langle\alpha'|\mathbf{A}|\alpha\rangle(n_\alpha - n_{\alpha'})e^{i(E_\alpha - E_{\alpha'})t/\hbar}, \tag{2.27}$$

and hence

$$\chi_{BA}(\omega) = \lim_{\epsilon \to 0^+} \int_0^\infty K_{BA}(t) e^{i(\omega + i\epsilon)t} dt$$

$$= \lim_{\epsilon \to 0^+} \sum_{\alpha\alpha'} \frac{\langle \alpha | \mathbf{B} | \alpha' \rangle \langle \alpha' | \mathbf{A} | \alpha \rangle}{E_{\alpha'} - E_\alpha - \hbar\omega - i\hbar\epsilon} (n_\alpha - n_{\alpha'}), \qquad (2.28)$$

$\chi_{BA}(\omega)$ can be separated into the reactive and absorptive part of susceptibility. The absorptive part of susceptibility is

$$\chi''_{BA}(\omega) = \pi \sum_{\alpha\alpha'} \langle \alpha | \mathbf{B} | \alpha' \rangle \langle \alpha' | \mathbf{A} | \alpha \rangle (n_\alpha - n_{\alpha'}) \delta(\hbar\omega - (E_{\alpha'} - E_\alpha)) \qquad (2.29)$$

and the reactive part of susceptibility is

$$\chi'_{BA}(\omega) = \sum_{\alpha\alpha'}^{E_\alpha \neq E_{\alpha'}} \frac{\langle \alpha | \mathbf{B} | \alpha' \rangle \langle \alpha' | \mathbf{A} | \alpha \rangle}{E_{\alpha'} - E_\alpha - \hbar\omega} (n_\alpha - n_{\alpha'}) + \chi'_{BA}(el)\delta_{\omega 0} \qquad (2.30)$$

where

$$\delta_{\omega 0} \equiv \lim_{\epsilon \to 0^+} \frac{i\epsilon}{\omega + i\epsilon} = \begin{cases} 1 & \text{if} \quad \omega = 0 \\ 0 & \text{if} \quad \omega \neq 0 \end{cases} \qquad (2.31)$$

and the elastic term $\chi'_{BA}(el)$, which only contributes in the static limit $\omega = 0$, is

$$\chi'_{BA}(el) = \beta\{ \sum_{\alpha\alpha'}^{E_\alpha = E_{\alpha'}} \langle \alpha | \mathbf{B} | \alpha' \rangle \langle \alpha' | \mathbf{A} | \alpha \rangle n_\alpha - \langle \mathbf{B} \rangle \langle \mathbf{A} \rangle \}. \qquad (2.32)$$

The absorptive part $\chi''_{BA}(\omega)$ is a sum of δ-functions, whose argument is zero only when $\hbar\omega$ is equal to the excitation energies $E_{\alpha'} - E_\alpha$. In such system no spontaneous transitions occur. In real macroscopic system the distribution of states is continuous and only the ground state may be considered as a well-defined discrete state. At non-zero temperature the parameters of the system are subject to fluctuations in space and time. The introduction of a non-zero probability for a spontaneous transition between the levels α and α' can be included in a phenomenological way by replacing the energy difference $E_{\alpha'} - E_\alpha$ by $(E_{\alpha'} - E_\alpha) - i\Gamma_{\alpha'\alpha}$. When $|E_{\alpha'} - E_\alpha| \gg \Gamma_{\alpha'\alpha}$ the δ-function is

effectively replaced by a Lorentzian:

$$\chi''_{BA}(\omega) \simeq \sum_{\alpha\alpha'} \frac{\langle\alpha|\mathbf{B}|\alpha'\rangle\langle\alpha'|\mathbf{A}|\alpha\rangle}{(E_{\alpha'} - E_\alpha - \hbar\omega)^2 + \Gamma^2_{\alpha'\alpha}} \Gamma_{\alpha'\alpha}(n_\alpha - n_{\alpha'})$$
$$+ \frac{\hbar\omega\Gamma_0}{(\hbar\omega)^2 + \Gamma_0^2} \chi'_{BA}(el) \tag{2.33}$$

with a linewidth, or more precisely FWHM (full width at half maximum), of $2\Gamma_{\alpha'\alpha}$. The corresponding reactive part of the susceptibility is

$$\chi'_{BA}(\omega) \simeq \sum_{\alpha\alpha'} \frac{\langle\alpha|\mathbf{B}|\alpha'\rangle\langle\alpha'|\mathbf{A}|\alpha\rangle}{(E_{\alpha'} - E_\alpha - \hbar\omega)^2 + \Gamma^2_{\alpha'\alpha}} (E_{\alpha'} - E_\alpha - \hbar\omega)(n_\alpha - n_{\alpha'})$$
$$+ \frac{\Gamma_0^2}{(\hbar\omega)^2 + \Gamma_0^2} \chi'_{BA}(el) \tag{2.34}$$

The absorption observed in the resonance experiment is proportional to $\chi''_{AA}(\omega)$. The peak in the absorption spectrum is interpreted as an elementary or quasi-particle excitation, or as a normal mode of the dynamic variable $\mathbf{A}$, with a lifetime $\tau \simeq \hbar/\Gamma_{\alpha'\alpha}$.

LiHoF$_4$ eigenvalues E_α and eigenstates $|\alpha\rangle$ in thermal equilibrium are calculated in a mean-field approximation, as explained in the previous section.

In a standard electron spin resonance (ESR) experiment the excitation oscillating field of the fixed frequency ω is perpendicular to the external magnetic field. We orientate the sample so that the external magnetic field is along the x-axis and oscillating field along the y-axis, so the Zeeman term is $\mathcal{H}_1 = -g_L\mu_B J_y H_y(t)$, which means that $\mathbf{A} = g_L\mu_B J_y$, where J_y is a quantum operator for the angular momentum of the electron, $g_L = 1.25$, and μ_B is a Bohr magneton. Since the experimental setup is measuring the sample's response or change of magnetization along the y-axis, $\mathbf{B} = \mathbf{A} = g_L\mu_B J_y$.

This would be the case for a typical electron spin resonance experiment, but as we have seen in previous chapter, we are probing the entangled nuclear-electron states, so our excitation and response are coupled to the nuclear and electronic moments. Thus, $\mathcal{H}_1 = -(g_L\mu_B J_y + g_N\mu_N I_y)H_y(t)$, and $\mathbf{B} = \mathbf{A} = g_L\mu_B J_y + g_N\mu_N I_y$, where I_y is the quantum operator for angular momentum of the nuclei, $g_N = 4.173$ is the nuclear magnetic moment of Ho^{3+} in units of μ_N and μ_N is the nuclear magneton.

For transitions between hyperfine levels, which are eigenstates of I_z in zero field, so predominantly nuclear-spin levels,

Since the transitions are induced between hyperfine levels, which are eigenstates of I_z in zero field, we would expect that the intensity of the response to the oscillating field
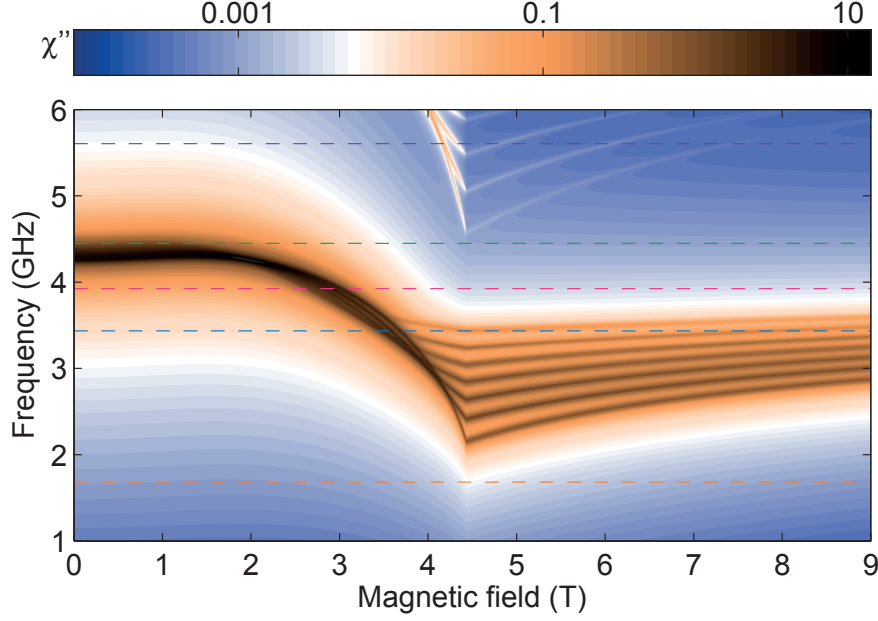
Figure 2.11: Calculated absorption χ'' as a function of the transverse magnetic field at 0.3 K.

is dominantly from the nuclear operator. We were surprised to find out that the electronic operator is dominating in the magnetic-resonance experiment. By calculating separately the contribution from the electrons and the nuclei we have found that contribution from the electrons is approximately 500 times larger than the contribution from the nuclei. We conclude that this is a hybrid magnetic resonance experiment, where levels are predominantly nuclear-spin levels as in nuclear magnetic resonance (NMR), while the signal is coming from electrons as in electron spin resonance (ESR) experiment.

Our calculation of the absorptive part

$$\chi''_{(J_y+I_y)(J_y+I_y)}(\omega) = \sum_{\alpha\alpha'} \frac{\langle\alpha|(g_L\mu_B\mathbf{J}_y + g_N\mu_N\mathbf{I}_y)|\alpha'\rangle\langle\alpha'|(g_L\mu_B\mathbf{J}_y + g_N\mu_N\mathbf{I}_y)|\alpha\rangle}{(E_{\alpha'} - E_\alpha - \hbar\omega)^2 + \Gamma^2_{\alpha'\alpha}}\Gamma_{\alpha'\alpha}(n_\alpha - n_{\alpha'})$$
$$+ \frac{\hbar\omega\Gamma_0}{(\hbar\omega)^2 + \Gamma^2_0}\chi'_{BA}(el) \tag{2.35}$$

for LiHoF$_4$ has been shown in Fig. 2.11.

The maximum absorption appears exactly at the excitation frequencies which are equal to the difference between the two energy levels. If we track the field-dependence of the absorption at a fixed frequency, for example at 3.9 GHz, there is a maximum at 3 T. The only free parameter in our calculations is the lifetime or the width of the

Lorentzians in the absorption spectrum $\Gamma_{\alpha'\alpha}$. If the width is infinitesimally small, there would be 7 separated absorption peaks. Since in our experiment at 3.9 GHz absorption appears as one broad peak at 3 T, the width in the simulation shown in Fig. 2.11 was set to $\Gamma_{\alpha'\alpha} = 0.1$ μeV (lifetime $\tau \simeq 40$ ns) to reflect that. It is not correct to assume that the lifetime of the states does not change with temperature or field, especially between the ferromagnetic and paramagnetic phase, but we shall discuss this in detail later when analysing the experimental results.

2.4 Entanglement

2.4.1 Quantum information meets condensed matter

The phenomenon of entanglement is probably the most fundamental characteristics which distinguishes the quantum from the classic world. Entanglement was one of the first studied and discussed aspects of quantum physics (e.g., EPR paradox [38]), and there are many ways of defining it. In the last 30 years, the interest in quantum entanglement has risen sharply in various formerly disconnected scientific communities, bringing them together in unexpected ways.

In the early 1980s the entanglement between particles inside and outside of a black hole was suggested the basis for the properties of the Hawking's radiation. The idea is that an observer outside of the black hole will perceive an effective mixed quantum state if there is entanglement with the other subsystem inside the black hole. The entanglement entropy between pure quantum subsystems is corresponding to the von Neumann entropy associated with the reduced density matrix.

In the 1990s, with the rise of quantum information science, it was important to find a quantitative measure of entanglement. One of the most important results in quantum information science is that entanglement entropy is a candidate for measuring entanglement between two subsystems.

In recent years there has been a cultural interchange between quantum information science and condensed-matter physics. Traditionally, the characterisation of many-body systems has been carried on through the study of different physical quantities, such as magnetization and susceptibility in magnetic systems, and their correlations. Very little attention was paid to the structure of their quantum state and in particular to their amount of entanglement. Methods developed in quantum information have proven to be extremely useful in the analysis of the state of many-body systems.

This new interdisciplinary field could improve our understanding of strongly correlated systems, and also help control and manipulate quantum correlations to our convenience, with the hope of making an impact on the quantum computation.

2.4.2   Entanglement as a tool to characterise quantum phase transition

Among the most challenging and interesting problems in quantum dynamics involve understanding the behaviour of strongly-coupled many-body systems with many degrees of freedom that undergo quantum phase transition. Classical phase transitions occur when a physical system reaches a state below a critical temperature characterized by a microscopic order. Quantum phase transitions (QPT) occur at an absolute zero temperature, and they are induced by the change of an external parameter or coupling constant, and are driven by quantum fluctuations [39, 40]. Both classical and quantum second order phase transitions are governed by a diverging correlation length, although quantum systems possess additional correlations that do not have a classical counterpart. This phenomenon is known as entanglement. The role of entanglement at a phase transition is not captured by statistical mechanics.

At the moment the most common technique to study entanglement in critical quantum systems is the renormalization group (RG), which is the standard way to obtain information about systems at and near criticality. The development of the renormalization group has shown that phase transitions are universal in the sense that many properties of a system do not depend on the details of a system. Instead, using the RG techniques, it has been shown that the critical behaviour depends only on certain global properties, such as symmetry and dimension.

Recently it became apparent that there was a rich structure to be uncovered by introducing the concept of entanglement entropy in context of many-body physics, in particular in the vicinity of the transition point [12]. Osborne *et al.* [11] argued that the physical origin of the long-range correlations which occur in systems exhibiting a quantum phase transition is quantum entanglement. It was also argued that a system state is strongly entangled at the critical point. A ground-state wavefunction undergoes qualitative changes at a quantum phase transition, which is why it is important to understand how its quantum aspects evolve throughout the transition. The analysis of entanglement for a condensed-matter system close to a quantum critical point allows us to characterize both quantitatively and qualitatively the change in the wavefunction of the ground state on passing the transition.

The entanglement entropy is a good candidate to characterize quantum states near a critical point because of its simple definition. We only have to divide a system into subsystems and calculate the entanglement entropy. The entanglement entropy extracts fundamental properties of a critical behaviour in a cleaner way than most standard quantities and measures quantum correlations in a more universal and flexible way than the correlation functions themselves.

The association between entanglement and phase transitions has been studied in different systems [12, 11]. The ground-state entanglement in the infinite one-dimensional

Heisenberg chain was studied by Wootters [41]. Numerical calculations of entanglement in the Heisenberg model on a small number of sites were carried out by Arnesen *et al.* [42]. Arnesen *et al.* identified parameter regions where there is appreciable thermal entanglement, which is entanglement present at nonzero temperatures. Recent studies include the numerical calculation of entanglement in the transverse Ising model on small numbers of sites [43], and the analytic computations of entanglement in the XY model on two sites [44] and three sites [45]. However, the precise nature of the relationship between entanglement and phase transitions is not yet fully understood.

2.4.3   Entanglement entropy

Entanglement entropy is a measure of entanglement between two regions of a system and is given by the von Neumann entropy associated with the reduced density matrix.

Consider two noninteracting regions of the systems A and B, with respective Hilbert spaces H_A and H_B. The Hilbert space of the composite system is the tensor product $H_A \otimes H_B$. If the first system is in state $|\psi\rangle_A$ and the second system in state $|\psi\rangle_B$, the state of the composite system is $|\psi\rangle_A \otimes |\psi\rangle_B$. If the state of the composite system can be represented in this form, it is called a separable state or product state. If the systems A and B are entangled, the composed state may not be represented in a separable form as a product state.

Since only the product states lead to pure reduced density matrices, a measure for their mixedness is a step toward quantifying entanglement. One of the most useful mathematical tools in understanding how to quantify entanglement is that of the Schmidt decomposition, which is based on the property of singular value decomposition for matrices.

In general, any composite state $|\Psi\rangle$ in $H_A \otimes H_B$ can be represented as

$$|\Psi\rangle = \sum_j c_j |\psi_j\rangle_A \otimes |\psi_j\rangle_B, \tag{2.36}$$

where $|\psi\rangle_A$ and $|\psi\rangle_B$ are orthonormal vectors in H_A and H_B, respectively, which is essentially a restatement of the singular value decomposition. According to the Schmidt theorem, the scalars c_j are real, non-negative, and, as a set, uniquely determined by $|\Psi\rangle$. They are called Schmidt coefficients.

If $|\Psi\rangle$ can be expressed as a product $|\psi\rangle_A \otimes |\psi\rangle_B$ then it is called a separable state. Otherwise, $|\Psi\rangle$ is said to be an entangled state. From the Schmidt decomposition, we can see that $|\Psi\rangle$ is entangled if and only if $|\Psi\rangle$ has Schmidt rank strictly greater than 1. The number of Schmidt coefficients of $|\Psi\rangle$, counted with multiplicity, is called its

Schmidt rank. Therefore, the two subsystems that partition the pure state are entangled if and only if their reduced states are mixed states.

The measure of entanglement between A and B in $|\Psi\rangle$ is then determined by the c_j values and the von Neumann entropy is defined as

$$S \equiv -\sum_j |c_j|^2 \ln |c_j|^2. \tag{2.37}$$

If $c_1 = 1$ and all $c_{i \neq 1} = 0$, entropy is zero, which means that $|\Psi\rangle$ is a product state and is unentangled (although there may still be correlations). If, on the other hand, all c_j are equal, then the entanglement entropy takes its maximal value, given by the logarithm of the smaller of the dimensions of H_A and H_B. For example, if each subspace is a tensor of a spin-$\frac{1}{2}$ (2-dimensional) then the maximal entanglement entropy is $\ln 2$.

2.4.4   Nuclear-electronic hybrid

The association between the entanglement and the phase transitions has been studied in different systems [12, 11, 41, 42, 43, 44, 45], but the precise nature of this relationship is not yet fully understood. We try to detect the presence of quantum phase transition by analysing a ground-state wavefunction of nuclear-electronic ferromagnet $LiHoF_4$ from a perspective of the quantum entanglement between the electronic and the nuclear subsystem.

$LiHoF_4$ undergoes a second-order quantum phase transition at a critical transverse field around $H_C = 5$ T. The magnetization along the c-axis vanishes above H_C. On the contrary the magnetization along a-direction is different from zero at any transverse field larger than 0 T due to the transverse field along a-axis.

The $LiHoF_4$ single-ion Hilbert spaces is constructed as a tensor product of the electronic and the nuclear Hilbert spaces, $H_e \otimes H_n$. The total electronic angular momentum $J = 8$ creates a (2J+1)=17-dimensional Hilbert space H_e, while the nuclear spin $I = 7/2$ forms a 8-dimensional Hilbert space. The total nuclear-electronic Hilbert space is 136-dimensional. To calculate the entanglement entropy the system needs to be divided into two partitions. The most natural way to do that is to calculate the entanglement between the nuclear and the electronic subsystem.

We analysed the entanglement between the nuclear and the electronic part of the ground state wavefunction as a function of a transverse field along the crystallographic a-axis and temperature (Fig. 2.12). In case the ground state is double degenerated, which is the case in the paramagnetic phase at zero field, we analysed one of the two degenerated ground states.
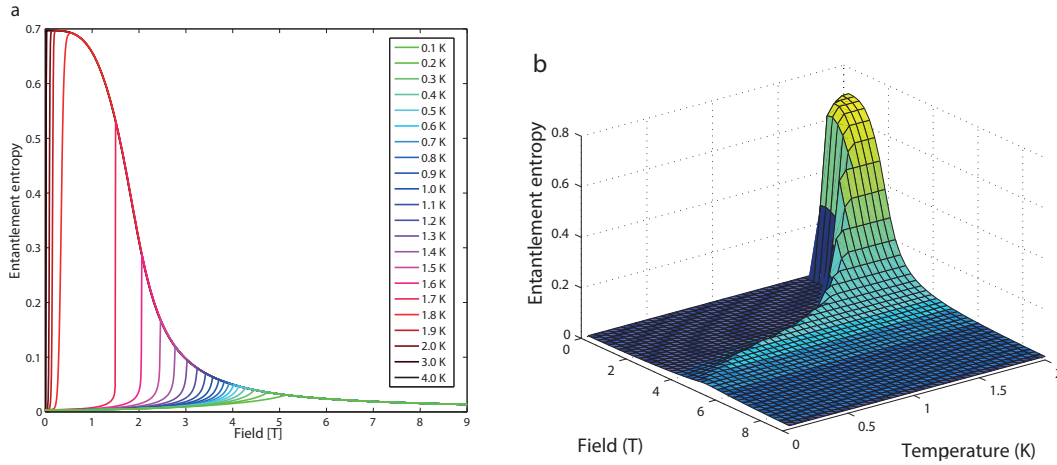
Figure 2.12: **a**) The entanglement entropy as a function of transverse field, calculated at different temperatures. **b**) The same calculation shown as 3D shaded surface plot.

The entanglement entropy in the ferromagnetic phase varies from zero at zero field to maximum at the quantum phase transition H_C, and then again descends toward zero at high fields. There is a characteristic sharp peak at critical field. In the limit $B = 0$ T, the entanglement entropy in the ordered phase approaches zero due to a large dipolar mean field along the c-axis which is reinforcing the anisotropy along c-axis, so the ground state is similar to the product state. On the other hand, the transverse field along the a-axis is mixing higher excited states into the ground state, consequently enhancing mixedness between the nuclear and the electronic subsystem. The entanglement entropy, as a measure of this mixedness, peaks at H_C. At the large transverse field $H > H_C$, a dipolar mean field along the c-axis is zero, the electronic and the nuclear moments polarize in a direction of the transverse field, so ground state gravitates toward the product state, resulting in the entanglement entropy approaching zero.

Calculation shows that the entanglement between the nuclear and the electronic subsystem is maximal at the critical field H_C, which supports the experimental data from Ronnow *et al.* [17] where they show that the soft mode is gapped near the phase transition due to strong nuclear-electronic coupling.

It is unexpected that maximum in the entanglement entropy is increasing with the temperature. The entanglement entropy is not measuring the entanglement content of the ground state, but rather it is measuring the degree of mixing of the ground state. The increase of temperature is decreasing the dipolar mean field along the c-axis, so there is more mixing between the nuclear and the electronic subsystem at higher temperature.

The unexpected feature is the appreciable entanglement in the system for temperatures

above the critical temperature 1.8 K, where the quantum system is expected to behave classically. The presence of the entanglement in the system at temperatures above the energy gap indicates that quantum effects persist past the point where they are usually expected to disappear.

In the paramagnetic phase the entanglement entropy is temperature independent because the temperature only enters the Hamiltonian through mean-field ($\langle J \rangle$), which is zero above T_C.

One would expect a maximum entanglement entropy to appear at 0 T in the paramagnetic phase. The reason for small entanglement at 0 T in the paramagnetic phase is the Ising-like degenerate ground state of $LiHoF_4$. We calculate entanglement entropy for only one of these two degenerated states as a function of transverse field. At zero field ground state is degenerate, and each of the two states is an unentangled state, but small transverse field is enough to break the degeneracy and mix two ground states, resulting in maximally entangled state.

Above H_C, the system is in a paramagnetic state in a strong transverse field and temperature does not make a difference on the ground state entanglement entropy.

The calculated entanglement entropy in the absence of interactions decreases smoothly as a function of transverse field. This result is in agreement with those previously reported by Schechter and Stamp *et al.* [21]. However, turning on dipolar coupling in the model produces a cusp-like peak at the QPT, which reflects the enhanced mixing upon approaching the QPT.

Theoretically the maximal entropy is equal to the dimension of the subsystem with lower dimension. In our case it is a nuclear subsystem which is 8-dimensional, so the maximal entropy should be $\ln 8$. However, maximum of the calculated entanglement entropy in $LiHoF_4$ appears to be $\ln 2$. The reason for this might be that the $LiHoF_4$ ground state can be treated as an effective transverse field Ising model which is 2-dimensional electronic spin subsystem.

The analysis of the entanglement for a condensed-matter system close to a quantum critical point allows us to characterize both quantitatively and qualitatively the change in the wavefunction of the ground state on passing the phase transition. We see that the entanglement between the electronic and the nuclear subsystem is an indicator of the quantum phase transition. A sharp peak of the electron-nuclear entanglement entropy and transition in the structure of the entanglement takes place exactly at the critical point.

Since the total wavefunction is approximated to a product of mean-field wavefunctions of the nuclear-electronic states the correlations between the electronic moments are neglected (Fig. 1.1c). On the other hand, an isolated nuclear-electronic state would

not track the QPT which results from the underlying transverse-field Ising model as a solely many-body phenomenon. This suggests that the entanglement present in the transverse-field Ising model leaves a signature on the nuclear-electronic states through hybridization. By attaching a nuclear spin to each electronic moment, a two-body pure-state wavefunction could suffice to trace the entanglement that dictates the QPT.

Whilst current theory of entanglement entropy has largely focused on pure states of spin-1/2 one-dimensional systems or mixed states of two qubits [12, 46], the field is still developing. Strong hyperfine interaction has been previously suggested to limit our ability to observe intrinsic electronic criticality by the introduction of nuclear spin bath [17]. Our new results suggest that we may actually take advantage of the nuclear spins entangled with the electronic moments to monitor the underlying criticality.

3 Experimental techniques and setup

3.1 Continuous-wave magnetic resonance

3.1.1 Principle of operation

The energy differences between states can be measured and with knowledge of these energy differences, we gain insight into the magnetic interactions of the sample under study. We can measure these energy differences, ΔE, because of an important relationship between ΔE and the absorption of electromagnetic radiation. According to Planck's law, electromagnetic radiation will be absorbed if:

$$\Delta E = hf = \hbar\omega \tag{3.1}$$

where h is Planck's constant, $\hbar = \frac{h}{2\pi}$, f is the frequency and ω is the angular frequency of the radiation.
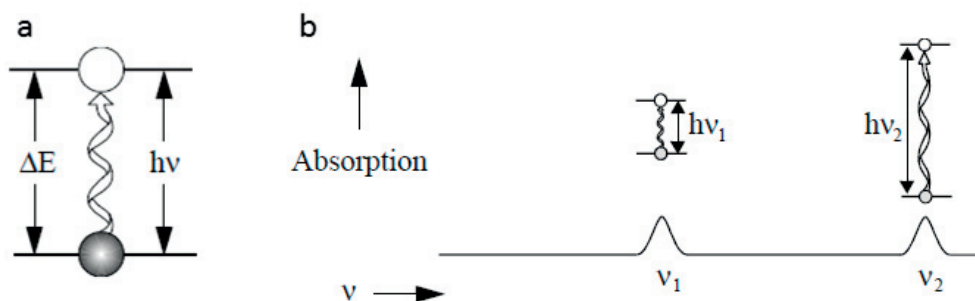
Figure 3.1: **a**) Transition associated with the absorption of electromagnetic energy. **b**) An absorption spectrum. After Ref. [47].
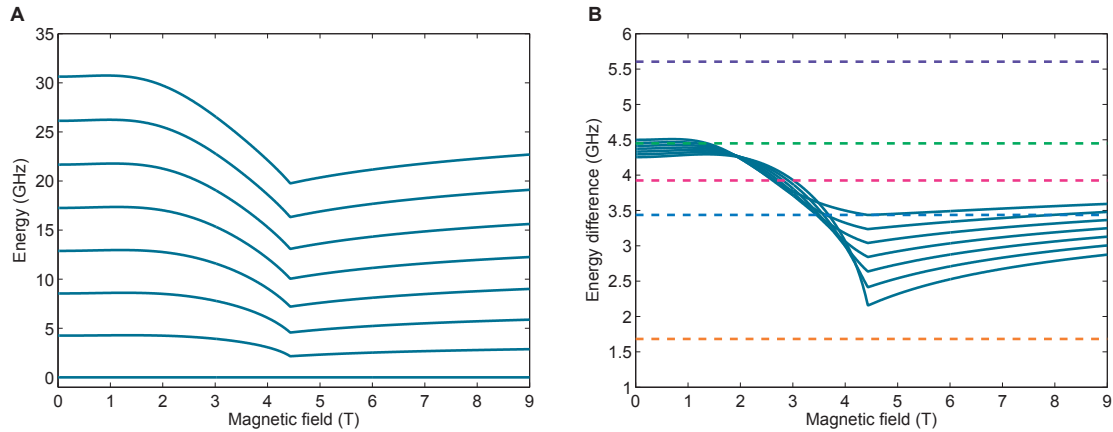
Figure 3.2: **a**) Lowest lying hyperfine states calculated in the mean-field model. **b**) Difference of energy between subsequent lowest lying hyperfine levels.

The absorption of energy causes a transition from a lower energy state to a higher energy state (see Fig. 3.1A). In conventional spectroscopy, frequency is varied or swept and the frequencies at which absorption occurs corresponds to the energy difference between the states. This record is called a spectrum. The frequencies vary from radio waves in the megahertz range, typical for nuclear magnetic resonance (NMR), to microwaves in the gigahertz range, typical for electron spin resonance (ESR), to visible and ultraviolet light. Since the hyperfine coupling is particularly strong in our sample, the splitting between nuclear-electronic levels becomes ∼4.5 GHz whereas in most other systems it is in MHz range. Splitting between the levels change with transverse magnetic field produced by superconducting magnet in the laboratory.

Typically, without a magnetic field, nuclear states are degenerate, so there is no energy difference to measure in the zero field, but in $LiHoF_4$ there is a strong internal magnetic field from ferromagnetic ordering at low temperature, of strength $A\langle J\rangle$, which gives rise to a large hyperfine energy of 4.5 GHz. Since a transverse magnetic field reduces the order parameter $\langle J\rangle$, it also reduces the energy difference between hyperfine states.

As we can change the energy differences between the two states by varying the magnetic field strength, we thus have an alternative way to obtain a spectra. Instead of applying a constant magnetic field and scanning the frequency of the electromagnetic radiation, we keep the electromagnetic radiation frequency constant and scan the magnetic field. A peak in the absorption of electromagnetic radiation will occur when the magnetic field tunes the nuclear-electronic states so that the energy difference between subsequent states matches the energy of the radiation (Fig. 3.2a). This field is called the resonant field.

In $LiHoF_4$, there are 8 hyperfine states so there are 7 transitions between subsequent energy levels (Fig. 3.2b). Each of these transitions can be tuned to the energy of

radiation so one would expect to measure 7 peaks, unless the peaks are so close to each other and so broad that they appear as one peak.

3.1.2 Detection of the signal

In a continuous wave (CW) magnetic resonance the signal is produced by a precessing magnetization in the sample. The precessing magnetization occurs in the presence of, and in response to, a weak oscillating transverse magnetic field $B(t)$. The precessing magnetization will induce a voltage in a resonator placed around the sample and the spectrometer on the reception side should detect this voltage signal.

The spectral feature of a CW signal can be calculated. A voltage is induced in the resonator by the precessing magnetization, the relation between the two being determined by various geometrical factors concerning the size of the specimen and the disposition of the resonator. The precessing magnetization results from the oscillating transverse magnetic field and the ratio of the two is the susceptibility of the sample. If we know the excitation magnetic field and if we can measure the signal voltage, we can calculate the susceptibility of the sample.

Magnetic susceptibility is defined as the ratio of magnetization to the applied magnetic field, but it is also the factor by which the inductance of a resonator is enhanced. An inductor of inductance L_0, when embedded in a medium of susceptibility χ, has its inductance changed to

$$L = L_0(1 + \chi). \tag{3.2}$$

The factor $(1 + \chi)$ is usually referred to as the relative permeability of the medium. In a practical arrangement the resonator is not embedded in the sample; but the sample is placed near the resonator. Thus, not all the magnetic field of the resonator permeates the medium; some is in the surrounding space. The enhancement of inductance is then not complete and we should write

$$L = L_0(1 + \eta\chi), \tag{3.3}$$

where the dimensionless quantity η, i.e. the filling factor quantifies this effect. Similarly, a small sample would have a reduced filling factor. We have seen in the chapter 2.3 how the magnetic susceptibility embodies a full description of the linear response of a system. Now we see that the susceptibility is reflected in the inductance of a resonator. The frequency dependent susceptibility $\chi(\omega)$ is a complex quantity. This has important consequences for the observed inductance L of the resonator, which are

best considered in terms of the complex impedance of the resonator

$$Z = -i\omega L + r, \tag{3.4}$$

where r is the resistance associated with the resonator. With a specimen coupled to the resonator this becomes

$$Z = -i\omega L_0(1 + \eta\chi) + r, \tag{3.5}$$

and writing χ in terms of its real and imaginary parts

$$\chi = \chi' + \chi'' \tag{3.6}$$

we obtain

$$Z = -i\omega L_0(1 + \eta\chi') + \omega L_0\eta\chi'' + r. \tag{3.7}$$

The imaginary part of the susceptibility has introduced a real term in the impedance. Putting a sample near the resonator causes it to appear as a changed inductance in series with an increased resistance.

There is a direct electrical way in which the CW magnetic resonance may be detected. It proves convenient to quantify the loss in the resonator, instead of using the resistance r, in terms of the dimensionless parameter, the Q factor. Q-factor describes how underdamped a resonator is, and characterizes a resonator's bandwidth relative to its center frequency. For this circuit, the Q-factor becomes

$$Q = \omega L/r, \tag{3.8}$$

i.e. it is the ratio of the reactive impedance to the resistive impedance. As we have shown in the chapter 2.3, the imaginary part of the susceptibility changes when $\Delta E = hf$, so we see that the magnetic resonance phenomena has the effect of changing the Q factor of the resonator near the sample. If Q_0 is the natural Q of the resonator, corresponding to an equivalent series resistance r of

$$r = \omega L_0/Q_0, \tag{3.9}$$

then, since the effect of the sample is to add a further resistance Δr

$$\Delta r = \omega L_0 \eta \chi'', \tag{3.10}$$

we see that the inverse Q is increased by

$$\begin{aligned}
\frac{1}{Q} &= \frac{1}{Q_0} + \eta \chi'' \\
\Delta \frac{1}{Q} &= \eta \chi''.
\end{aligned} \tag{3.11}$$

Thus we see how measurement of the resonator's Q factor may be used to detect the magnetic resonance absorption as the imaginary part of the susceptibility.

3.1.3 Saturation

The size of the absorption signal voltage is proportional to the applied oscillating voltage amplitude V_0. This follows from the linearity assumption that the precessing magnetization which induces the signal voltage is proportional to the oscillating transverse magnetic field B_1, generated by the current in the resonator. This is the case only if the oscillating transverse magnetic field is small enough that it does not significantly perturb the population of states in the thermodynamical equilibrium.

If we treat the response of the CW magnetic resonance within the framework of the Bloch equations (details can be found in Ref. [49]) we shall get real and imaginary parts of susceptibility in terms of the spin-lattice and the spin-spin relaxation times, T_1 and T_2

$$\begin{aligned}
\chi'(\omega) &= \frac{\chi_0 \omega_0 T_2^2 (\omega - \omega_0)}{1 + (\omega - \omega_0)^2 T_2^2 + \gamma^2 B_1^2 T_1 T_2} \\
\chi''(\omega) &= \frac{\chi_0 \omega_0 T_2}{1 + (\omega - \omega_0)^2 T_2^2 + \gamma^2 B_1^2 T_1 T_2}
\end{aligned} \tag{3.12}$$

where ω is the frequency of the excitation, ω_0 is resonant frequency of the system and γ is a gyromagnetic ratio. Bloch equations 3.12 enable us to evaluate the respective contributions of real and imaginary parts of the frequency-dependent susceptibility. χ' and χ'' give the dispersion and the absorption curves, respectively (Fig. 3.3).

The real part of the dynamic susceptibility χ' is in phase with the oscillating external field. It does not affect the microwave power absorption in the sample but merely
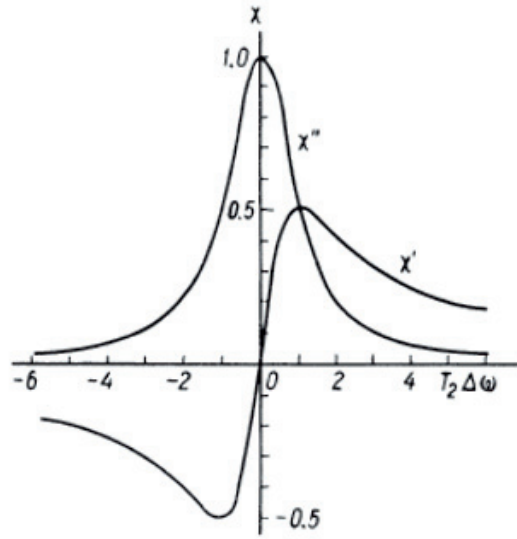
Figure 3.3: Real and imaginary part of susceptibility of the complex susceptibility $\chi = \chi' + i\chi''$ as a function of the frequency, for a generalized Lorentzian line shape (arbitrary scale). After Ref. [48].

describes a reactive effect, resulting in a shift in the resonance frequency [48]. To the first order in χ' the resonance frequency f_0 is proportional to dispersive part of the sample susceptibility [50]:

$$\omega \approx \frac{1}{\sqrt{L_0(1 + \eta\chi')}} \approx \omega_0 \left(1 - \frac{\eta\chi'}{2}\right). \tag{3.13}$$

The imaginary component χ'' of the dynamic susceptibility is in antiphase with the high-frequency field and has a resonant character. It determines the absorption of microwave power by the sample. Thus, the frequency dependent function $\chi''(\omega)$ reflects the line shape of the absorption, observed experimentally with the spectrometer.

Equations 3.12 indicate that non-linear behaviour is possible at high fields B_1 since the magnitude of the susceptibility depends on the strength of the applied field B_1. Only in the limit

$$\gamma^2 B_1^2 T_1 T_2 \ll 1 \tag{3.14}$$

the observed susceptibility is linear or independent of the strength of the excitation. It is only in this limiting case that the frequency response takes on the characteristic Lorentzian form.
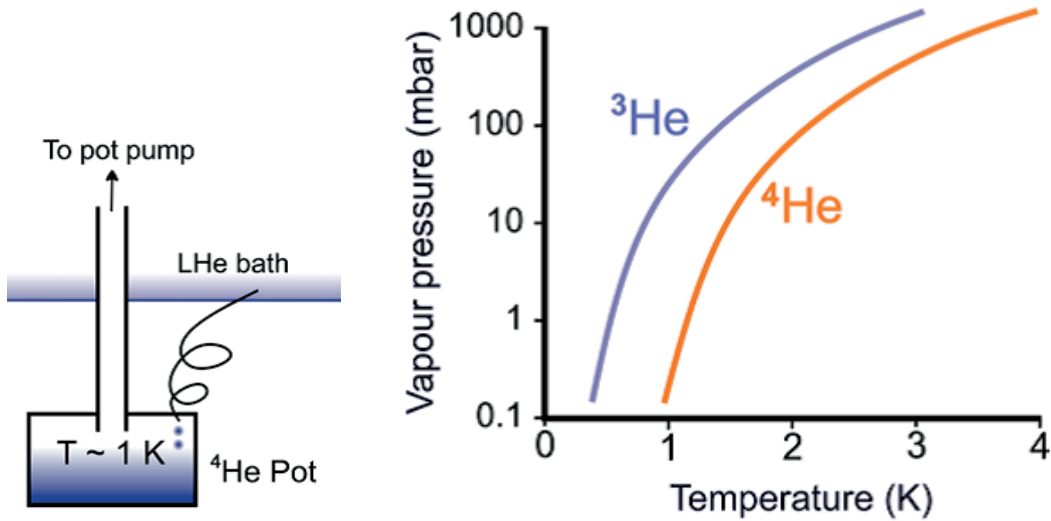
Figure 3.4: **a**) Scheme of the ^{4}He or 1K pot. **b**) Vapour pressure of ^{3}He and ^{4}He as a function on temperature. After Ref. [51].

For a physical understanding of the linearity condition let us consider the energies involved. The quantity B_1 determines the flow of energy from the oscillating magnetic field into the spin system. The rate of flow of energy out of the spin system is determined by the spin-lattice relaxation. In the steady state the flow in is balanced by the flow out. What is important from the linearity point of view is that in this steady state the spin system should not be disturbed significantly from its equilibrium state - in particular, that the Boltzmann distribution of population of the spin states should not be appreciably disturbed. This requirement is contained in Eq. 3.12. We see that the effect of a large B_1 is to equalise the populations of states. This phenomenon is known as saturation. To maintain the linearity of the response it is necessary to avoid saturation.

3.2 Dilution refrigerator

Interesting physics in LiHoF$_4$ appears at low temperatures, below 0.3 K, where hyperfine interactions change the phase diagram. To be able to reach such low temperatures we have to use a dilution refrigerator. The dilution refrigerator is immersed into a liquid helium ^{4}He bath of re-condensing cryostat which provides a stable cold environment, at 4.2 K, for the dilution refrigerator and at the same time cools superconducting wires of the magnet which provides magnetic field up to 18 T.

A ^{4}He pot pre-cools a ^{3}He - ^{4}He mixture to 1.2 K. In a small pot called 1K pot, ^{4}He is continuously fed through a small pipe which is pumping out ^{4}He from the liquid helium bath (Fig. 3.4a). At the same time ^{4}He is continuously pumped out of the 1K
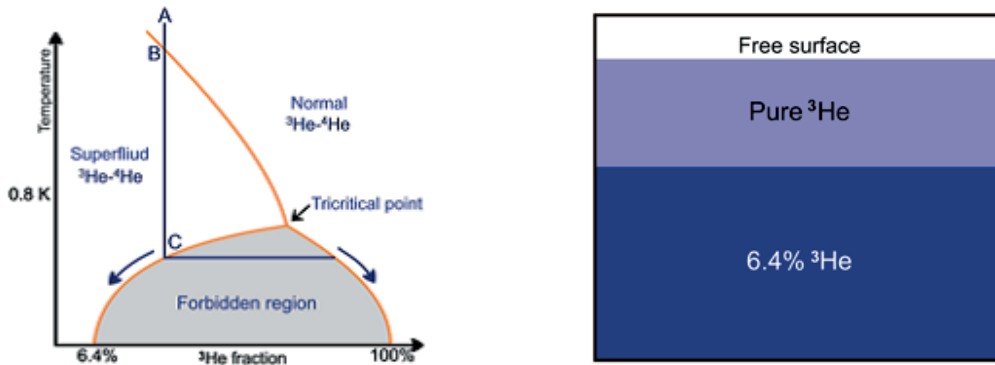
Figure 3.5: **a**) Phase diagram of the ^{3}He - ^{4}He mixture. **b**) Phase separation of pure ^{3}He and diluted ^{4}He phase in the ^{3}He - ^{4}He mixture. After Ref. [51].

pot by the 1K pot pump to achieve a constant pressure of approximately 0.1 mbar. At that pressure ^{4}He can be easily cooled down to 1.2 K (Fig. 3.4b). Cooling is achieved due to the latent heat of the evaporated liquid ^{4}He.

^{3}He is lighter than ^{4}He and it can be cooled down to 0.3 K by pumping on it, while ^{4}He can be cooled down to 1.2 K. ^{4}He has 4 nucleons and a nuclear spin of I = 0. It obeys Boson statistics and undergoes a transition to a superfluid at 2.17 K. ^{3}He has 3 nucleons, and a nuclear spin of $I = \frac{1}{2}$. It obeys Fermi statistics and the Pauli exclusion principle, which prevents it from undergoing a superfluid transition until a much lower temperature at which spins pair up to make a Boson. ^{3}He can be diluted in ^{4}He and the superfluid transition temperature of a ^{3}He - ^{4}He mixture depends on the ^{3}He concentration (Fig. 3.5a). When the ^{3}He - ^{4}He mixture is cooled down it first undergoes a transition to a superfluid, and then finally below 0.8 K the mixture is separated into two phases; one with pure ^{3}He and other with some amount of ^{3}He diluted in ^{4}He (Fig. 3.5b). If the mixture is cooled down even further to 0 K the ratio of ^{3}He to ^{4}He is further reduced, but finite, with the theoretical minimum at 6.4% of ^{3}He in the diluted phase at 0 K (Fig. 3.5a).

If we put pure ^{3}He in contact with pure ^{4}He, the single ^{3}He atom is more strongly bound to pure ^{4}He than to pure ^{3}He. The binding energy of a single ^{3}He atom in ^{4}He is larger than the binding energy of ^{3}He in ^{3}He, this is why ^{3}He atoms prefer to cross from a pure ^{3}He phase to a ^{4}He phase. This property is the reason for the solubility of ^{3}He in ^{4}He at 0 K. But the Fermi energy $k_B T_F$ of ^{3}He in ^{4}He will increase with the concentration of ^{3}He in ^{4}He. At a concentration of 6.4% the chemical potential of a ^{3}He atom in the diluted ^{4}He will be equal to its chemical potential in pure ^{3}He. At that point ^{3}He will stop crossing from pure ^{3}He to the diluted ^{4}He phase. This is why the solubility of ^{3}He in ^{4}He at 0 K is limited to 6.4%.

Heat is extracted every time a ^{3}He atom crosses from a pure ^{3}He phase to a diluted
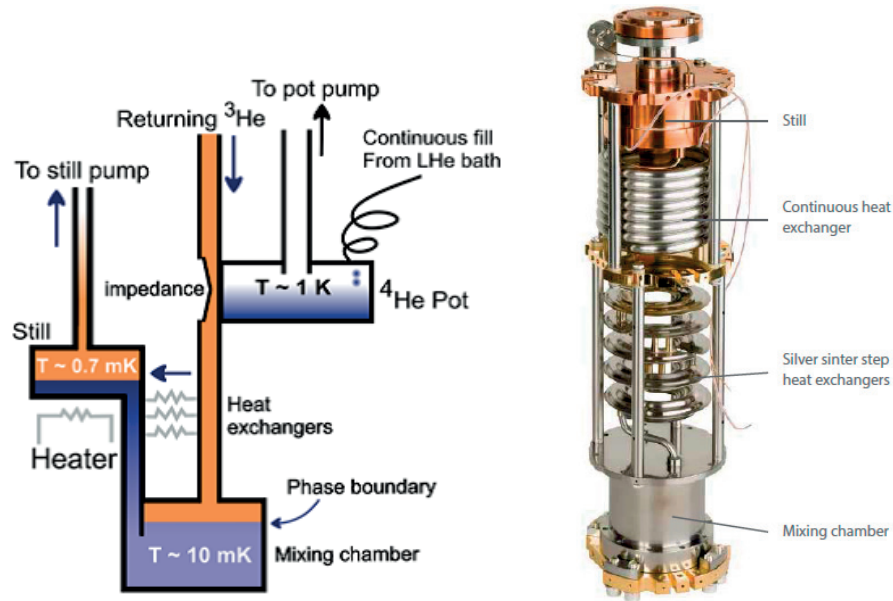
Figure 3.6: **a**) Scheme of dilution refrigerator. **b**) The dilution unit with its most important parts. After Ref. [51].

^{4}He phase. The associated cooling power is given by the enthalpy difference between ^{3}He in diluted and pure ^{3}He multiplied by the ^{3}He flow rate. The enthalpy of ^{3}He in ^{4}He is higher than the enthalpy in pure ^{3}He, due to the ^{3}He in ^{4}He behaving as a Fermi gas. This is similar to the enthalpy difference between the ^{3}He gas and ^{3}He liquid that results in the cooling power in an evaporation refrigerator.

The flow of ^{3}He from pure ^{3}He to diluted ^{4}He is established by constant removing ^{3}He from the diluted phase. This is done in a distiller (still), which is connected to a mixing chamber and distils ^{3}He from ^{4}He due to the difference in vapour pressure.

^{4}He is just a static background which is there to enable ^{3}He to transition from its pure liquid state into a Fermi gas. The dilution process of ^{3}He moving across the phase boundary is equivalent to an upside-down evaporator. While the lowest achievable temperate in an evaporator is limited by an exponentially decreasing vapour pressure, the concentration of ^{3}He in a Fermi gas (diluted ^{4}He) is constant with temperature.

We can now explain the whole circulation of ^{3}He in the dilution refrigerator. ^{3}He is circulated by a still pump which pushes the pumped ^{3}He from the still to the mixing chamber (Fig. 3.6a). Before reaching the mixing chamber ^{3}He gas is liquefied and then precooled. ^{3}He is liquefied when in contact with the 1K pot, which is kept at 1.2 K by the 1K pot pump. Impedance is there to increase the pressure and elevate the liquefying temperature. Heat exchangers take cooling power from the still which is at 0.7 - 0.8 K to cool down the liquid ^{3}He on its way to the mixing chamber. Finally, ^{3}He enters the mixing chamber where it first goes into the pure ^{3}He phase only to be moved across the
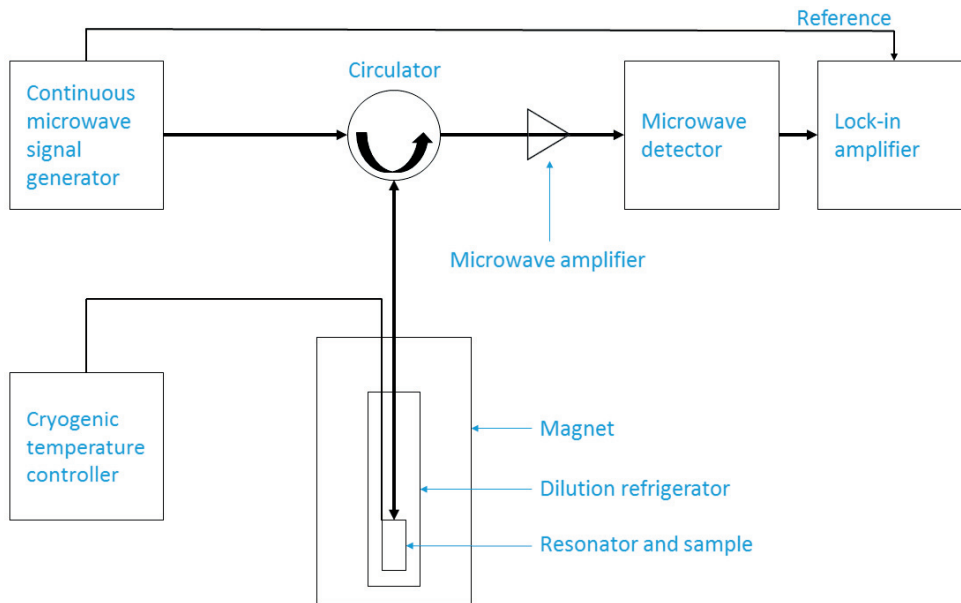
Figure 3.7: Scheme of the fixed-frequency continuous-wave experimental setup.

phase boundary to the diluted ^{4}He phase, which cools the mixing chamber. Osmotic pressure pulls ^{3}He from the mixing chamber to the still because of the difference between the concentration of ^{3}He in the still and in the mixing chamber. ^{3}He is then separated from ^{4}He by the still pump, and then pushed again to the mixing chamber, so the circle is closed. The dilution unit with all these parts, shown in Fig. 3.6b, is in the inner vacuum chamber, which is inside the cryostat filled with liquid ^{4}He at 4.2 K. The 1K pot pumps out ^{4}He from the cryostat, with the flow regulated by a needle valve. The still pump to cycle ^{3}He and the 1K pump to pump on ^{4}He are at room temperature.

3.3 Fixed frequency CW magnetic resonance

We would like to probe the nuclear-electronic states of Ho in LiHoF$_4$, but the NMR of rare-earths is constrained by technical difficulties, due to the very high frequency and fast relaxation. For this purpose we have built a continuous-wave microwave spectrometer that works at dilution temperatures. We shall explain the most important parts of this spectrometer in this section. A scheme of the setup is shown in Fig. 3.7.

3.3.1 Microwave signal generator

The signal generator, Agilent MXG N5181B, is an electronic device which produces simple repetitive waveforms, with the most simple one being a sine wave, which is what we have used in experiments. The maximum power produced by the signal generator is 16 dBm or 39.8 mW [52], but we typically worked at -16 dBm or 25 μW

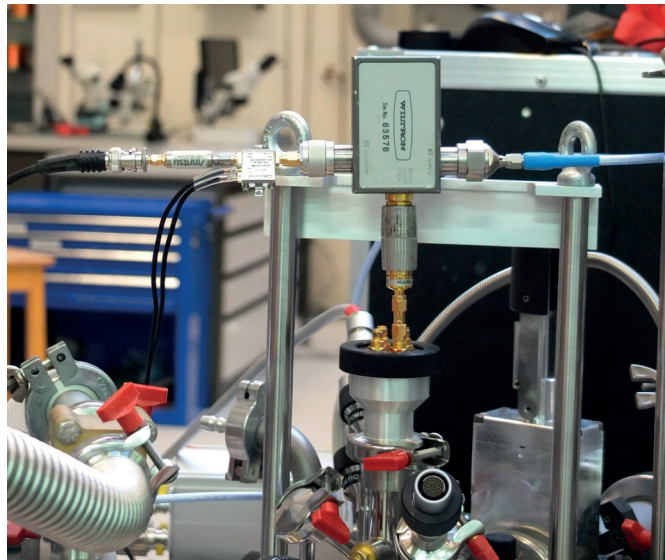Figure 3.8: Signal generator Agilent MXG N5181B.

Figure 3.9: Circulator connected to the signal generator (right port), resonator (lower port) and microwave detector (left port).

to minimise the heating. We used an amplitude modulation (AM) of the sine-wave electromagnetic field. The signal is transmitted from a signal generator to a circulator.

3.3.2 Circulator

The circulator, Wiltron 87A50 (2 GHz to 18 GHz), is a passive non-reciprocal three port device in which a microwave frequency signal is transmitted to the next port only. A port is a point where a coaxial cable connects to the circulator. A signal applied to the port 1 (Fig. 3.9) only comes out of the port 2 and a signal applied to the port 2 only comes out of the port 3. In the experimental setup, we connect signal generator as input to the port 1, this signal is then transmitted to port 2 where we connect a microwave coplanar resonator. The signal reflected from the resonator is an input for port 2 which comes out of port 3 where it is measured by a microwave detector and a lock-in amplifier. The change in the measured reflected signal is usually only a fraction
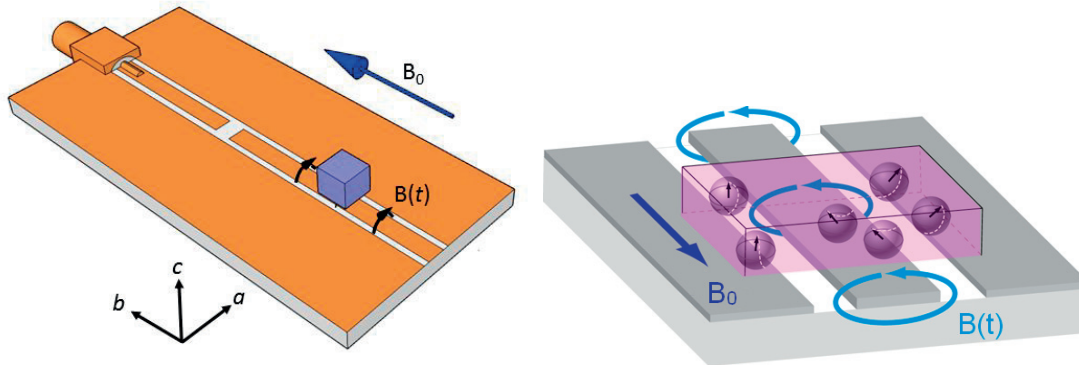
Figure 3.10: **a**) Schematic drawing of a microwave coplanar resonator loaded with the sample. **b**) Electronic spins in the sample in the static external field of the magnet and the oscillating field of the resonator. [After Ref. [53]]
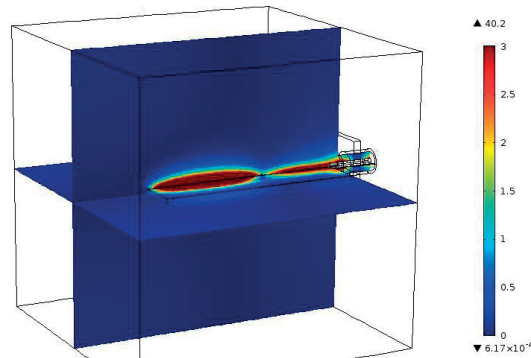

Figure 3.11: Magnitude of the oscillating magnetic field in vicinity of the resonator at fundamental frequency of the resonator.

of the original input signal, so we are not able to detect the reflected signal without separating it from the input signal by the circulator.

3.3.3   Microwave coplanar resonator

The microwave coplanar resonator absorbs most of the incident electromagnetic field in the standing wave in the active strip of the resonator (Fig. 3.10), but only in vicinity of a certain frequency of the microwave field. The scheme structure of the resonator is shown in Fig. 3.10a. Standing electromagnetic waves form in the active strip of the resonator which amplifies the microwave field. The amplitude of the magnetic field in vicinity of the resonator was modeled in the COMSOL software package by Zhuo Quan Im. The result, presented graphically in Fig. 3.11, shows that the microwave field has its largest amplitude near the active strip, but only if the microwave field is of the resonant frequency that is specific to the resonator.
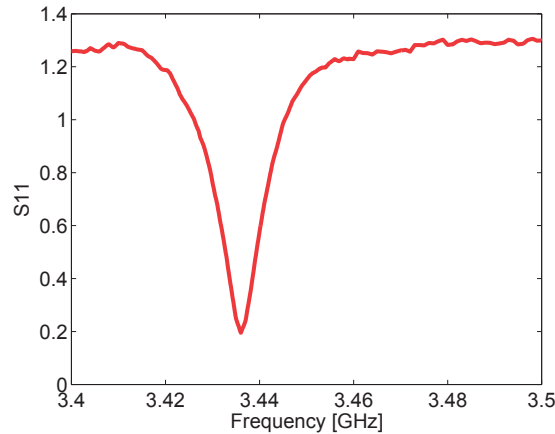
Figure 3.12: Reflection coefficient S_{11} as a function of frequency.

The resonator absorbs most of the incoming radiation, but only at the resonant frequency, while reflecting all incoming radiation at other frequencies. The resonator has a low loss at its resonant frequency, resulting in high Q factors. A high Q factor resonator amplifies the microwave, field which means there is a larger sensitivity. The Q factor is determined by the width of the resonance (FWHM) in the frequency spectrum, which means that a high-Q resonator only excites in a narrow frequency bandwidth. The benefit of a smaller Q is that we can excite more hyperfine transitions at the same time. We can measure the resonant frequency of the resonator by measuring the S_{11} parameter as a function of the frequency. The S-parameters ($S_{11}, S_{21}, S_{12}, S_{22}$), which are a typical way of characterizing two-port networks, are defined as the relationship between the reflected and incident power at each of the network ports (1 and 2). Since we did a one-port measurement, we measured the S_{11} parameter, which stands for the ratio of the reflected power (at port 1) and incident power (at port 1). A typical frequency scan, where $Q \simeq 250$, is shown in Fig. 3.12.

Our microwave resonators (Fig. 3.13) were prepared from Rogers RO4003C laminates for our experiment by Microsystems Laboratory at EPFL. The resonators consist of a 1.5 mm thick glass-reinforced hydrocarbon and a ceramic dielectric substrate (dielectric constant $\epsilon_R = 3.38$), laminated with a 35 μm electro-deposited copper layer. Two 0.1 mm thin parallel lines/gaps were cut in the copper layer to separate the central and outer parts of the plate. The central part of the plate is soldered to the inner conductor of the coaxial cable and the outer part of the plate is soldered to the shield of coaxial cable. A gap has been made in the central line and the width of this gap determines the capacitance for matching of the electronic circuits. For our experiment the gap was fixed to 0.1 mm. The length of the active strip determines the fundamental frequency of the standing wave, so we tuned all our resonators to the desired frequency by producing resonators with a different length of the active strip. The fundamental frequency should not significantly change with cooling the resonator to low temperatures. In our
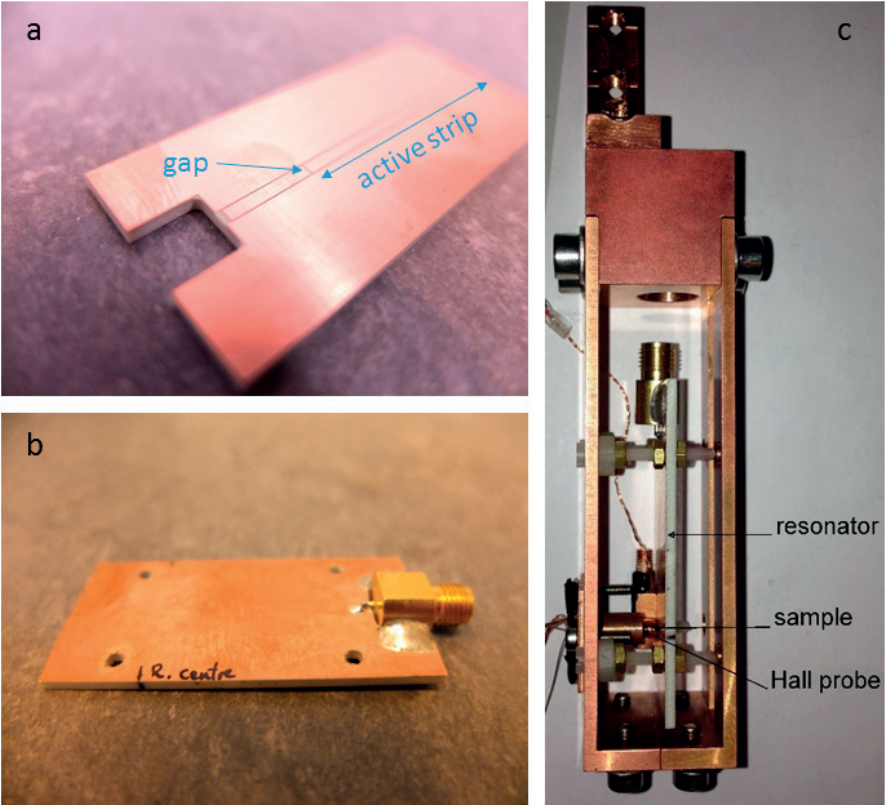
Figure 3.13: Microwave resonator **a**) before and **b**) after soldering the SMA connector for coaxial cable. **c**) Resonator mounted on the sample holder.

experiments we employed resonators with fundamental frequencies of 1.7, 3.4, 3.9, 4.5 and 5.6 GHz.

A cube-shaped LiHoF$_4$ sample of $2 \times 2 \times 2$ mm^3 is positioned just above the active strip of the resonator where the electromagnetic field is highest (Fig. 3.10). The sample is oriented in such a way that the oscillating field from the resonator is along the sample's a-axis and the magnetic field from the magnet is along the b-axis (a- and b-axis are equivalent). A copper cage around the resonator (Fig. 3.13c) holds the resonator and the sample in a fixed position in respect to each other. The copper cage hangs on a copper rod, which is screwed into the mixing chamber to ensure best thermal contact and prevent it from touching the inner vacuum chamber (IVC) can (which is at 4.2 K). To measure the signal reflected from the resonator, we first need to separate it using the circulator, then amplify it in a microwave amplifier and finally detect it using a microwave detector.

3.3.4 Microwave detector

The microwave detector, Agilent 8473B MW, is a Schottky diode detector which converts an input microwave signal to an output DC voltage. Before the detection, the signal was amplified by the 16 dB gain amplifier (Fig. 3.9). We measured the detector's input/output characteristics and fitted it to get the functional dependence of output voltage on input RF power. The measured reflected signal was then corrected for amplification and microwave detector non-linearity to estimate the microwave power. The input voltage was amplitude modulated by the signal generator so that the output signal from the microwave detector could be measured by the lock-in amplifier Ametek 7270, with the amplitude modulation from signal generator as the reference.

3.3.5 Complete magnetic resonance setup

After describing the setup component by component, we can sum up how the whole microwave setup works. The microwave signal is first synthesized by the signal generator. It is an amplitude modulated sine wave with a frequency between 1 and 6 GHz, depending on the fundamental frequency of the resonator. The microwave signal then goes through the circulator to the resonator where most of the input power is absorbed, if the microwave field is tuned to the fundamental frequency of the resonator. The input power is reflected at every other frequency far away from the fundamental frequency (Fig. 3.12). When the input power is absorbed, the standing wave is formed in the active part of the resonator where the microwave field is amplified. The spin ensemble in the sample is probed by the microwave signal. The sample can absorb the microwave power if there is an energy difference between the nuclear-electronic states that corresponds to the excitation frequency of the microwave field. The energy

Figure 3.14: Rohde & Schwarz ZVL 6 vector network analyzer.

difference of the sample's nuclear-electronic states can be tuned by magnetic field and temperature. In our case, the sample is tuned into resonance by applying an external transverse magnetic field B_0. If microwave radiation is absorbed by the sample, it perturbs the fundamental frequency f_0 and Q-factor of the resonator such that it no longer absorbs the same amount of input power as before. This perturbation can be measured by the power reflected from the resonator. The reflected signal goes through the circulator, which separates it from input signal. It is then amplified and converted to a DC signal by the microwave detector. Finally, the amplitude modulated DC signal is measured by a lock-in amplifier.

In a typical experiment we keep the frequency fixed at the resonators fundamental frequency and change the properties of the sample by slowly sweeping the magnetic field while recording the reflected signal. If the sample is tuned into resonance by the magnetic field, there is a peak in the reflected signal. The sample is constantly excited at a fixed frequency and the reflected signal is constantly recorded, while the magnetic field is slowly swept at 0.04 T/min.

3.4 Sweeping-frequency experimental setup

To test resonators' frequency characteristics S_{11} at room temperature and in zero-field, we used the Rohde & Schwarz ZVL 6 vector network analyzer (VNA) which measures the S_{11} reflection parameter in range of frequencies between 0 and 6 GHz with a maximum of 4000 points in the frequency spectrum per shot (Fig. 3.14). The network analyzer actually consists of components similar to these we have previously described in our experimental setup (chapter 3.3), but arranged in a compact package optimised for the measure of S_{11}. It also comes with a calibration kit, to compensate for various capacitance and inductance in the electric circuit between the resonator and the
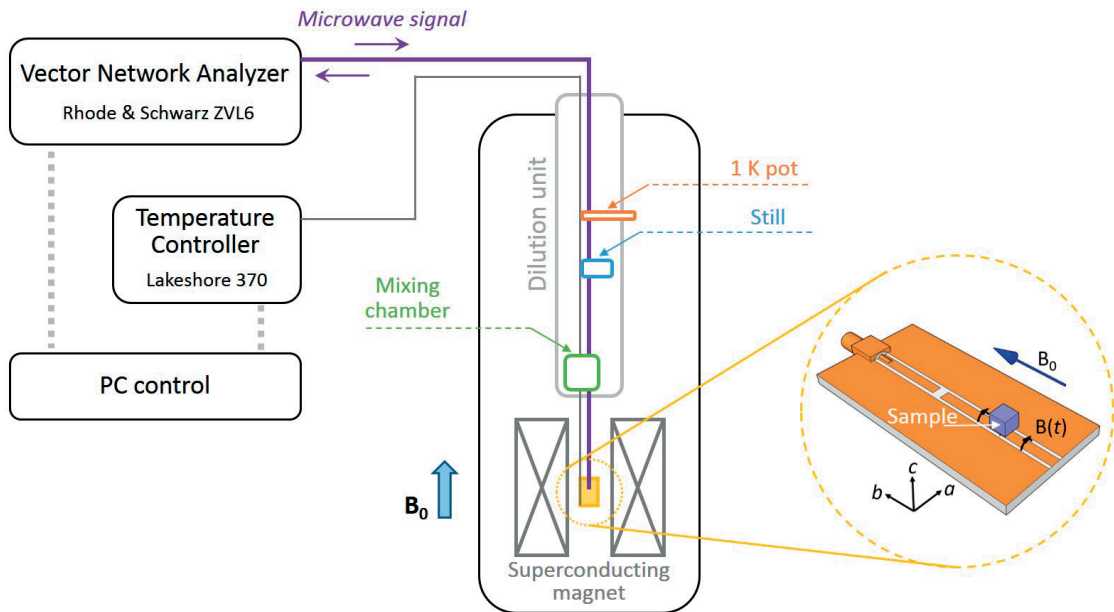
Figure 3.15: Scheme of the sweeping-frequency continuous-wave experimental setup.

network analyzer.

We could in principle do the frequency sweeps with our previously described setup, by changing the frequency in small steps and measuring S_{11} point-by-point, but we are limited by our software to recording 1 data-point every 0.1 seconds, while the network analyzer is manufactured to measure the 4000 points frequency spectrum in a fraction of a second.

We learned that we can use the network analyzer to measure the frequency spectrum of S_{11} while sweeping the field, instead of using a fixed frequency setup. This technique allowed us to take 3-dimensional data (S_{11}, frequency, magnetic field) in one field scan (Fig. 3.16). By analyzing every frequency scan at each magnetic field and fitting it to a Lorentzian we were able to determine the Q factor and the fundamental frequency of the resonator f_0, and track their field dependence. Most of our measurements were performed by using the sweeping-frequency experimental setup shown in Fig. 3.15.

On the other hand, fixed frequency setup is more versatile and can be used to measure power dependance. A fixed frequency setup constantly excites the sample at the same frequency f_0, while a vector network analyzer cyclicly changes the frequency around f_0. This makes fixed frequency setup more appropriate for measuring non-linear effects, which require a long-lasting excitation.

All instruments were controlled by a computer which also acquired the measured data. We wrote drivers for all mentioned instruments, and integrated their control in our
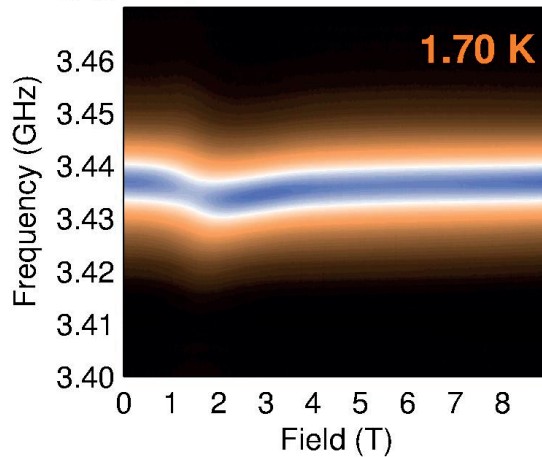
Figure 3.16: Reflected signal S_{11} as a function of the excitation frequency and magnetic field.

custom made measurements software, written in the Microsoft .NET platform. We also wrote software modules for the remote control of the dilution refrigerator.

3.5 Thermalization of the experimental setup

To cool down the LiHoF$_4$ sample to sub-Kelvin temperatures, we used an Oxford Instruments Kelvinox 400 dilution refrigerator (Fig. 3.17). The whole refrigerator was placed in the Oxford Instruments 18 T superconducting magnet providing top loading access to a sample in the dilution refrigerator. The dilution refrigerator achieves more than 400 μW cooling power at 100 mK, which makes it ideal for experiments with high heat dissipation such as microwave resonator losses. Base temperature is less than 9 mK, with no coaxial cables attached. This refrigerator has a line of sight of 38 mm diameter (from the top of the refrigerator to the mixing chamber) which allows to quickly change among different experimental inserts. We used a custom made high-frequency insert, with up to 4 semi-rigid coaxial cables and 2 Fisher 24-pin connectors.

The high-frequency insert has been wired with a semi-rigid coaxial cable, with a BeCu inner conductor and a stainless steel shield. It has been specified by manufacturer to have losses of 1 dB per meter at 5 GHz. The coaxial cable is approximately 2 m long, it goes all the way from the connector at the top of the refrigerator to the resonator bellow mixing chamber. By measuring the transmission coefficient S_{11}, we confirmed the total loss in our coaxial cable to be 2 dB. To compensate for possible losses in the coaxial cable, the network analyzer was calibrated at the SMA connector where the resonator was connected.

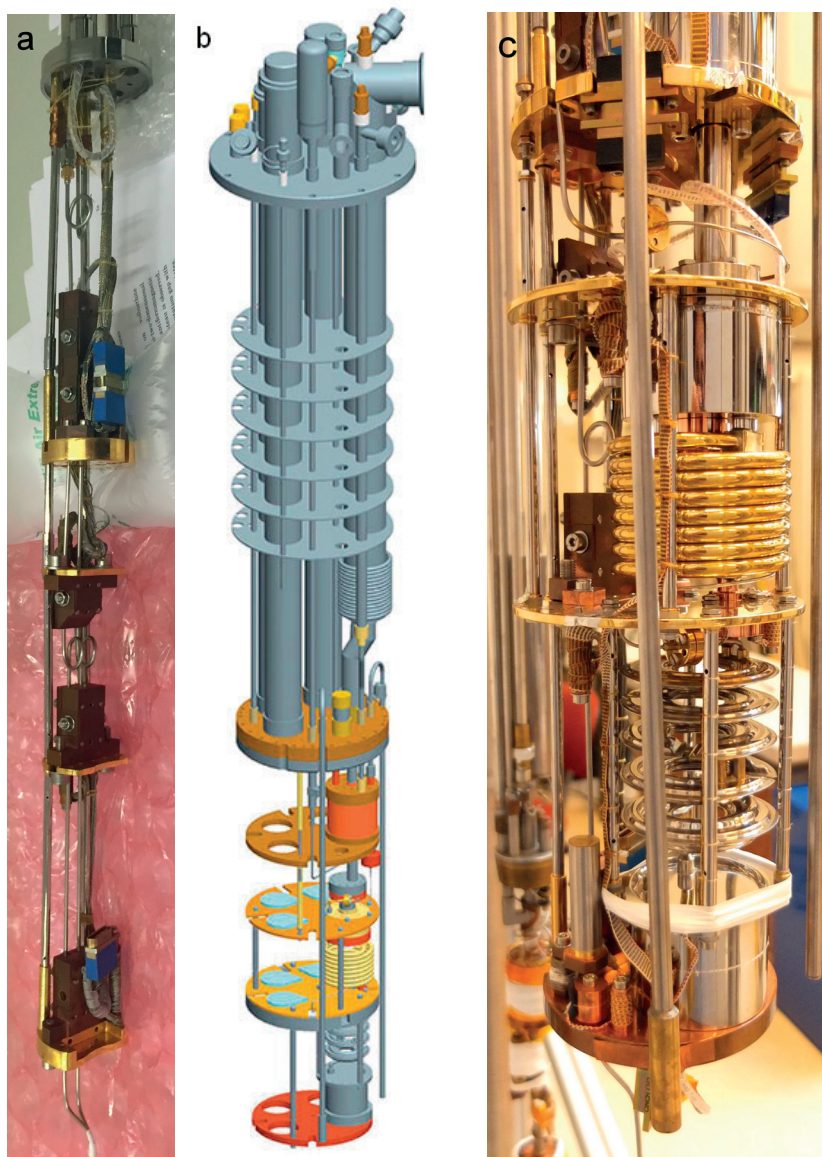After installing the high-frequency insert in the dilution refrigerator, the base temper-

Figure 3.17: **a**) High frequency insert with copper blocks attached. **b**) Scheme of the dilution refrigerator. **c**) Dilution unit with mounted high frequency insert.

ature increased to 30 mK, and the cooling power at 100 mK dropped to 150 μW. The main reason for this deterioration of the refrigerator's performance is the heat coming from outside through the coaxial cable. To reduce this effect we manufactured blocks, made in Oxygen-free high thermal conductivity copper, designed to take away the heat by thermalizing the coaxial cable at every stage of the dilution refrigerator, namely at the 1 K pot, at the still, at the cold plate and at the mixing chamber (Fig. 3.17). Copper is a good thermal conductor and these blocks have a large touching surface with the coaxial cable and with the plate at each stage. By thermalizing the coaxial cable at each stage, the heat is gradually transferred from the coaxial cable to the different parts of the dilution refrigerator. Most of the heat is extracted at higher temperature stages of the dilution refrigerator where more cooling power is available. Since the shield of the coaxial cable was well thermalized, the biggest source of heating was the inner conductor. To increase the thermal contact between inner conducer and shield, we made two loops in the coaxial cable; one loop between the cold plate and the still, and one loop just above the 1 K pot (as shown in Fig. 3.17). These loops are made so to squeeze the cable when the dilution refrigerator is cooled down and the stainless steel shield is contracted. At the very end of the coaxial cable, below the mixing chamber, a SMA connector was soldered and a microwave resonator was connected.

We made a sample and resonator holder out of copper and connected it with a copper rod to the bottom of the mixing chamber (Fig. 3.13). The sample holder was designed to thermalize the sample to the mixing chamber, and at the same time keep it thermally decoupled from the resonator.

The inner conductor of the coaxial cable is connected to the active strip of the resonator by a SMA connector. Since the inner conductor of the coaxial cable is at temperature higher than the mixing chamber, the resonator is also warmer than the mixing chamber. That is why the sample is thermally coupled to the mixing chamber, but thermally decoupled from the resonator. The sample is enclosed in Stycast with a thermometer and four copper wires. Stycast is a nonconductive epoxy resin for cryogenic use, which ensures the best thermal contact between the sample, the thermometer and the four copper wires, due to the large contact surface. The copper wires are squeezed close to the copper sample holder, which is then screwed into the mixing chamber to ensure good thermal contact between the mixing chamber and the sample. We have tried to decouple the resonator from the sample, by attaching it to the sample holder with PTFE pillars. PTFE is not only a poor thermal conductor, but also an electrical insulator, so that it keeps the resonator electrically decoupled from the copper cage.

The mixing chamber base temperature was 35 mK, while the sample temperature was 135 mK. The temperature was set by the temperature controller Lake Shore 370 with the heater attached to the mixing chamber. We show in Fig. 3.18 that the temperature of the mixing chamber was stable during field scans at different temperatures.
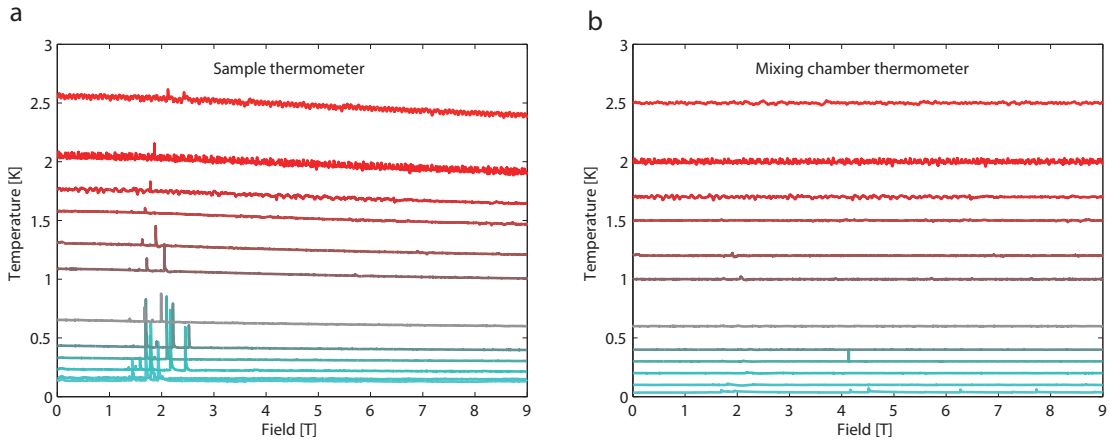
Figure 3.18: **a**) Sample and **b**) mixing chamber temperature stability during the field scan.
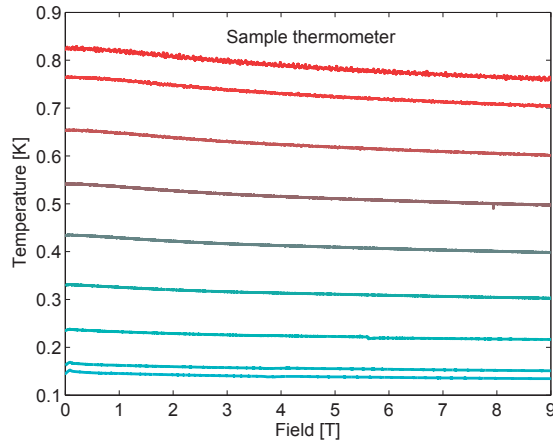

Figure 3.19: Sample temperature stability during field scan in 9T cryostat.

The sample temperature is higher than the mixing chamber temperature. Heating is coming from various sources, but mainly from the coaxial cable. Another source of heating is the Joule heating of the resonator from the oscillating microwave field which is in the vicinity of the sample. The microwave field absorbed by the sample at resonance also increases the sample temperature.

As a result of the heating, there is a temperature gradient between the sample and the mixing chamber (Fig. 3.18). This difference in temperature gradually disappears from 35 mK to 500 mK. At all temperatures above 500 mK, the averaged temperature of the sample is the same as that of the mixing chamber. An apparent cooling of the sample was observed during each field scan, even though we waited for 2 hours for temperature stability before each field scan. The apparent lowering of the sample temperature is likely due to the magnetoresistance of the sample thermometer which is a RuO_2 chip resistor with nominal resistance of 2.2 kΩ at room temperature. We do
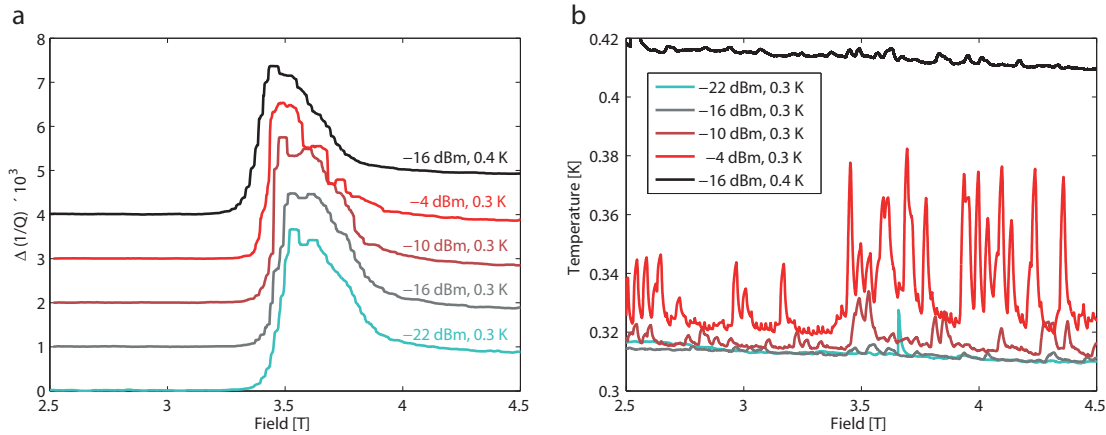
Figure 3.20: **a**) Absorption signal measured with the vector network analyzer. **b**) Sample temperature stability during the experiment at different microwave input power.

not see this effect in the mixing chamber thermometer because it is 40 cm further away from the magnet, where magnetic field is negligible. Spikes in the sample temperature at fields between 1.5 T and 2.5 T, present at low temperatures, became weaker or disappeared at higher temperatures. These spikes have not been observed in the 9 T magnet (Fig. 3.19), but once we performed the experiment in the 18 T magnet they were recorded in every experiment. The reason for this could be a flux creep in the magnet's superconducting wire. This apparent perturbation of the temperature is not affecting measurements since the measured spectrum is featureless at these fields and temperatures. Our results were consistent both in the 9 T and the 18 T magnets, hence we continued our experiments with the 18 T magnet.

We tested the heating from microwave radiation by increasing the input microwave power and monitoring the sample and mixing chamber temperatures. When performing the measurement with the network analyzer with excitation power of -22 dBm and -16 dBm, there is no heating of the sample, as shown in Fig. 3.20b. If the power is increased to -10 dB, we begin to see the first signs of heating. -16 dBm, the largest microwave excitation power at which the effect of heating from microwaves, was negligible was chosen as our standard excitation power for measurements. Figure 3.20a shows how heating of the sample influenced the measured absorption signal.

3.6   Interpretation of experimental results

The experiment is performed by cooling the sample to the desired temperature and then sweeping the transverse magnetic field from 0 to 9 T at 0.04 T/min. When the difference of energy between subsequent levels is equal to the excitation frequency, microwave power is absorbed by the sample. We have developed two experimental setups, one which works at a single fixed frequency and one which constantly sweeps
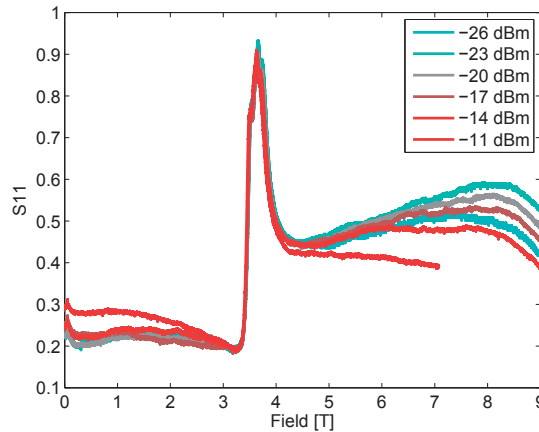
Figure 3.21: Reflected signal S_{11} as a function of field at 0.3 K.

across the frequency range, as discussed in previous sections.

First, we made the experiment with the fixed frequency setup, where the microwave excitation was supplied by a signal generator and the reflected power was measured by the microwave detector. The signal generator was supplying microwave power at a constant frequency equal to the resonant frequency, while the amplitude was modulated by 100% at a frequency of 1.123 MHz. Typical field scan recorded at 3.436 GHz and 0.15 K is shown in Fig. 3.21.

When the loaded resonator was cooled to sub-Kelvin temperatures, minimum reflected power was at 3.436 GHz, which we call the resonant frequency of the resonator f_0. At resonant frequency most of the incident power is absorbed and only a small fraction is reflected back from the resonator. The resonator is most sensitive to perturbation by spin system at the resonant frequency, so we keep the excitation frequency fixed at f_0. If microwaves are absorbed by the sample, the resonant frequency of the resonator and spin system is changed (as shown in Fig. 3.22). Not only the resonant frequency f_0 shifts, but also the depth and the width of the resonator's $S_{11}(f)$ curve (or Q factor) change at the resonance. Both of these effects result in a larger S_{11} at the fixed frequency, when the sample absorbs energy at a certain magnetic field. That is why we observe the peak in S_{11} at 3.63 T in Fig. 3.21. The only information that we can extract from this measurement is the resonant field. At given fixed temperature (0.3 K) and frequency (3.436 GHz) sample absorbs most power at 3.63 T, which means that the resonance condition is satisfied at that magnetic field. It is hard to quantify the absorption at resonant field because we do not know whether f_0 or Q is changing, or both. We would like to compare experimental results with calculations where we calculated the absorption or the imaginary part of susceptibility (Fig. 3.23). By comparing Fig. 3.21 and Fig. 3.23 we do see a resamblance, but we cannot make quantitative analysis beyond the observation that the resonant magnetic field is the same in the experiment and the calculations. This is already a proof that both our experimental setup and
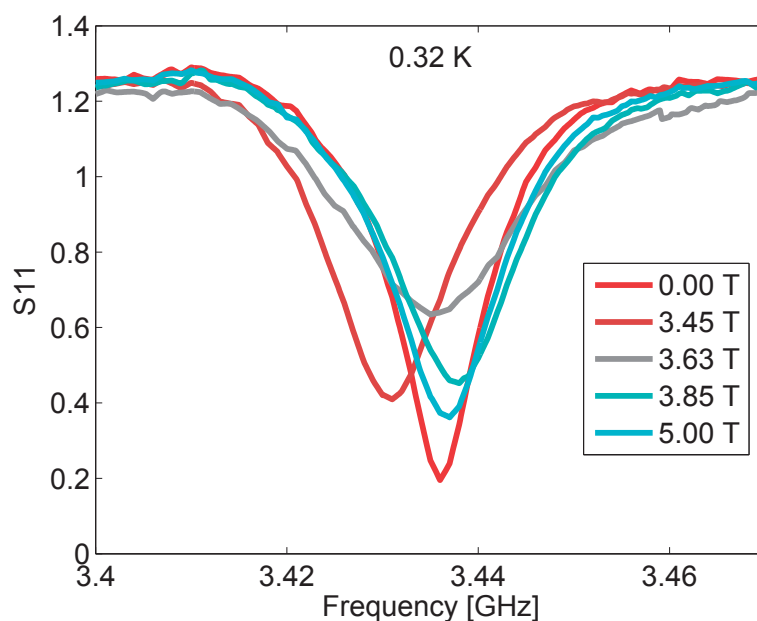
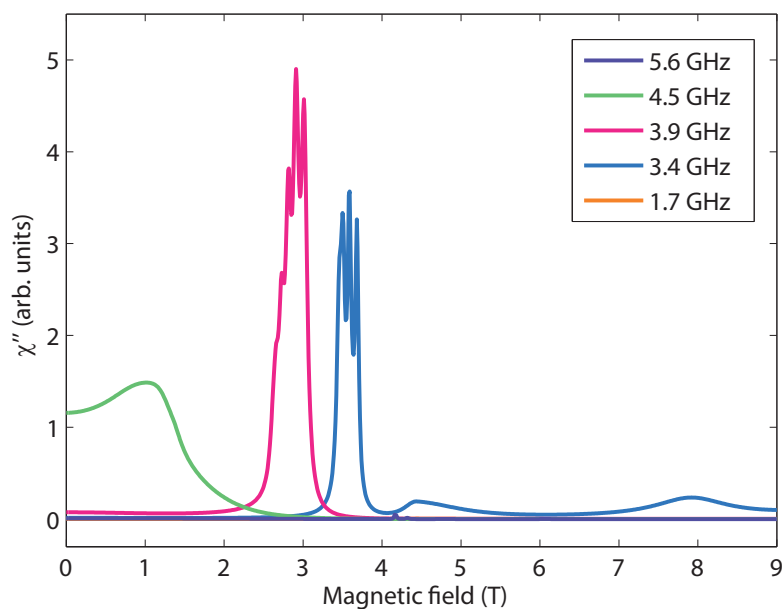Figure 3.22: Frequency scans at different fields with the resonator loaded with the sample.

Figure 3.23: Calculated absorption χ'' at different frequencies.

calculations give meaningful results. It also means that we were able to cool the sample below 0.15 K while exciting the system with a microwave field.

Instead of using the fixed frequency experimental setup, we could use the network analyzer to measure S_{11}. We have used the network analyzer at room temperature to measure the $S_{11}(f)$ of the empty resonator while tuning and matching resonators to have the desired fundamental frequency f_0.

After modifying the data acquisition and the instrument control to work with the network analyzer, we were able to record the S_{11} reflection while sweeping frequencies. That allowed us to do fast frequency sweeps continuously in a frequency range roughly centred at the resonant frequency, while slowly sweeping the magnetic field. The magnetic field was swept at 0.04 T/min to prevent heating from Eddy currents caused by changing the magnetic field in the copper sample holder. This resulted in a measurement where $S_{11}(f, B_t, T)$ was measured as a function of frequency and transverse magnetic field, at fixed temperature.

Measurements were carried out at 5 characteristic frequencies: 1.7, 3.4, 3.9, 4.5 and 5.6 GHz, each of them corresponding to a different resonator. We measured at several different temperatures with every resonator, from base temperature 0.13 K to 3 K. At each measurement we did the complete field scan from 0 to 9 T.

Now that we can measure full frequency scan at each magnetic field (Fig. 3.22), we have to relate the measured frequency spectrum with the calculated susceptibility. As we have shown in the chapter 3.6, the change of $1/Q$, where Q is quality factor of the resonator, is proportional to the imaginary part of the sample susceptibility χ''

$$\frac{1}{Q} = \frac{1}{Q_0} + \eta\chi''. \tag{3.15}$$

Change in the real part of the susceptibility χ' causes a shift in the resonance frequency f_0.

Our objective is to accurately and precisely measure the quality factor Q and the resonant frequency f_0 of a microwave resonator, using the complex reflection coefficient data acquired by the vector network analyzer as a function of frequency. Accurate Q and f_0 measurements are needed for high precision measurements of magnetic susceptibility via resonator perturbation.

We fit the reflection coefficient $S_{11}(f)$ data to a Lorentzian curve using a nonlinear least squares fit to determine the resonant frequency f_0 and the quality factor Q. The resonant frequency f_0, bandwidth $\Delta f_{Lorentz}$, background constant C and maximum
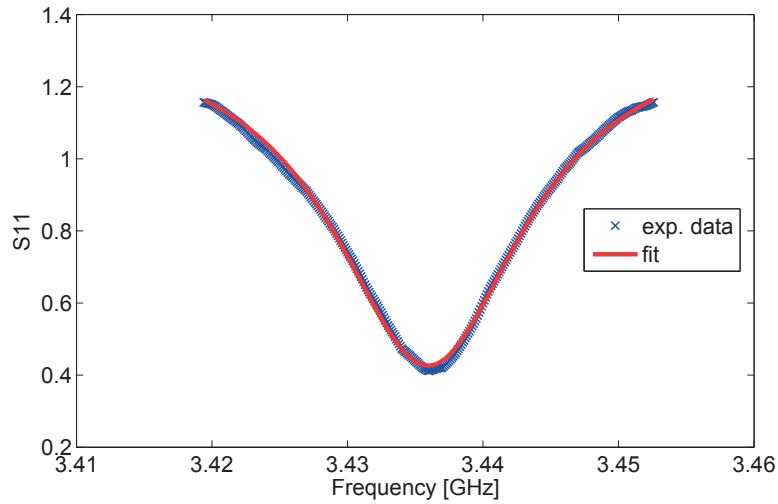
Figure 3.24: Typical fit of raw data to Lorentzian curve, recorded at 0.32 K with 3.4 GHz resonator.

magnitude A are used as fitting parameters for the Lorentzian:

$$S_{11}(f) = C + \frac{2A}{\pi} \frac{\Delta f_{Lorentz}}{4(f - f_0)^2 + \Delta f^2}. \tag{3.16}$$

Typical such fit to raw data is shown in Fig. 3.24. The Q is then calculated using the values of f_0 and $\Delta f_{Lorentz}$ from the final fit parameters $Q = f_0/\Delta f_{Lorentz}$. We fit the frequency scan at a fixed field, delivering the values of Q and f_0 at each field. This procedure allows the extraction of the full field dependence of both Q and f_0. Background constant C has been fixed to the value found at zero-field, for the entire field-scan.

4 Magnetic resonance of entangled states

4.1 Experimental results

The magnetic resonance experiment was performed by sweeping a transverse magnetic field from 0 to 9 T around 5 different frequencies between 1.7 and 5.6 GHz to get a complete picture of the energy landscape (Fig. 4.1). Each frequency was measured with different microwave resonator. The resonators can be divided in two different categories; those which satisfy the magnetic resonance condition $\Delta E = hf$ and those resonators whose frequency is either too high or too low to cross the difference between energy levels. The resonators with fundamental frequency of 3.4 and 3.9 GHz cross the maximum of absorption, which is shown by dashed blue and red line in Fig. 4.1. Measurements with 1.7 GHz resonator, shown by dashed orange line, are at a frequency which is too low to satisfy the magnetic resonance condition, while measurements at 5.6 GHz are always above the resonance frequency. Resonator with fundamental frequency at 4.5 GHz is just at the upper edge of the resonance frequency at zero-field. Each of these measurements was carried out at temperatures ranging from 0.13 to 3 K.

Experiments were carried out by measuring the reflected signal, S_{11}, by the vector network analyzer. Vector network analyzer was sweeping the frequency in span of 100 MHz, centered roughly at the fundamental frequency of the resonator. Measurements were performed in a field-scan mode from 0 to 9 T at base temperature. Temperature is then gradually increased in steps and experiment was repeated at different temperatures.

The microwave resonator is coupled to the spin ensemble, so when the resonant frequency of the spin ensemble approaches fundamental frequency of the resonator it changes f_0 and Q of the resonator. An avoided crossing pattern, which is a signature of the strong coupling between the microwave resonator and the spin ensemble, appears in frequency-field map (Fig. 4.2) when the transition between the hyperfine energy levels approaches the fundamental frequency of the resonator. Resonance frequency
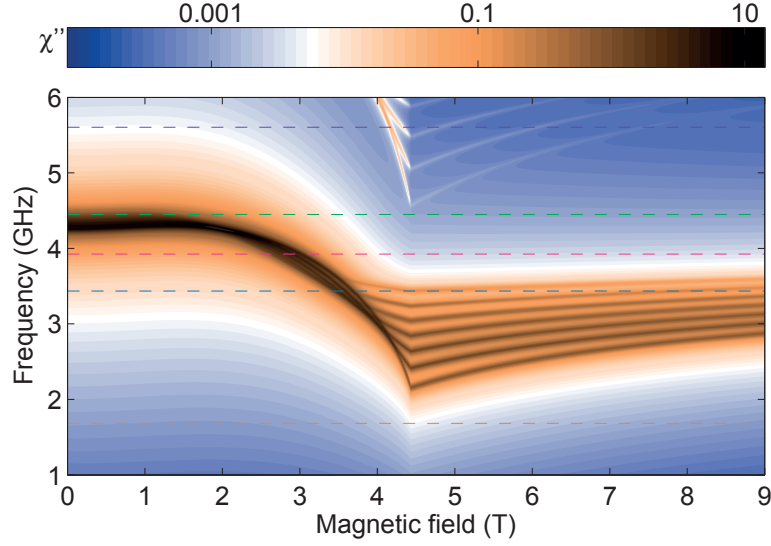
Figure 4.1: Absorption χ'' at 0.3 K calculated in linear-response theory framework. Dashed lines show fundamental frequencies of microwave resonators.

f_0 shifts when when the sample resonance is close to it. This results primarily from the dispersive part of the sample susceptibility, which is proportional to the resonance frequency f_0. When the magnetic resonance condition is satisfied, the resonator line is damped by the coupling to the nuclear-electronic spin ensemble.

4.1.1 Magnetic resonance at 3.4 GHz

The first experiment we did was with the resonator which has a resonant frequency of 3.436 GHz. The amplitude of S_{11} as a function of frequency and transverse magnetic field at different temperatures is shown in Fig. 4.2. The loaded resonator is matched ($Q \simeq 250$) and tuned to 3.436 GHz in zero-field at 0.14 K. As the magnetic field is increased, the resonator is unperturbed at low fields, then strongly perturbed around 3.7 T, and then unperturbed again at higher fields. At 3.7 T there is an avoided crossing pattern in S_{11} as a function of field and frequency. This pattern was observed in every field scan in which the temperature is below the phase transition temperature, 1.5 K. Above T_C the sample is in the paramagnetic phase where the magnetic resonance is much weaker in strength, therefore the perturbation of the resonator is also very weak, so there is no avoided crossing pattern.

We could determine the magnetic resonance field just from Fig. 4.2, but to resolve the magnetic susceptibility we extract the quality factor Q and the resonant frequency f_0 of the microwave resonator using complex reflection coefficient data, S_{11}, as a function of the frequency at each magnetic field. We perform nonlinear least squares fit of reflection coefficient S_{11} as a function of frequency (Fig. 4.3) to a Lorentzian curve,
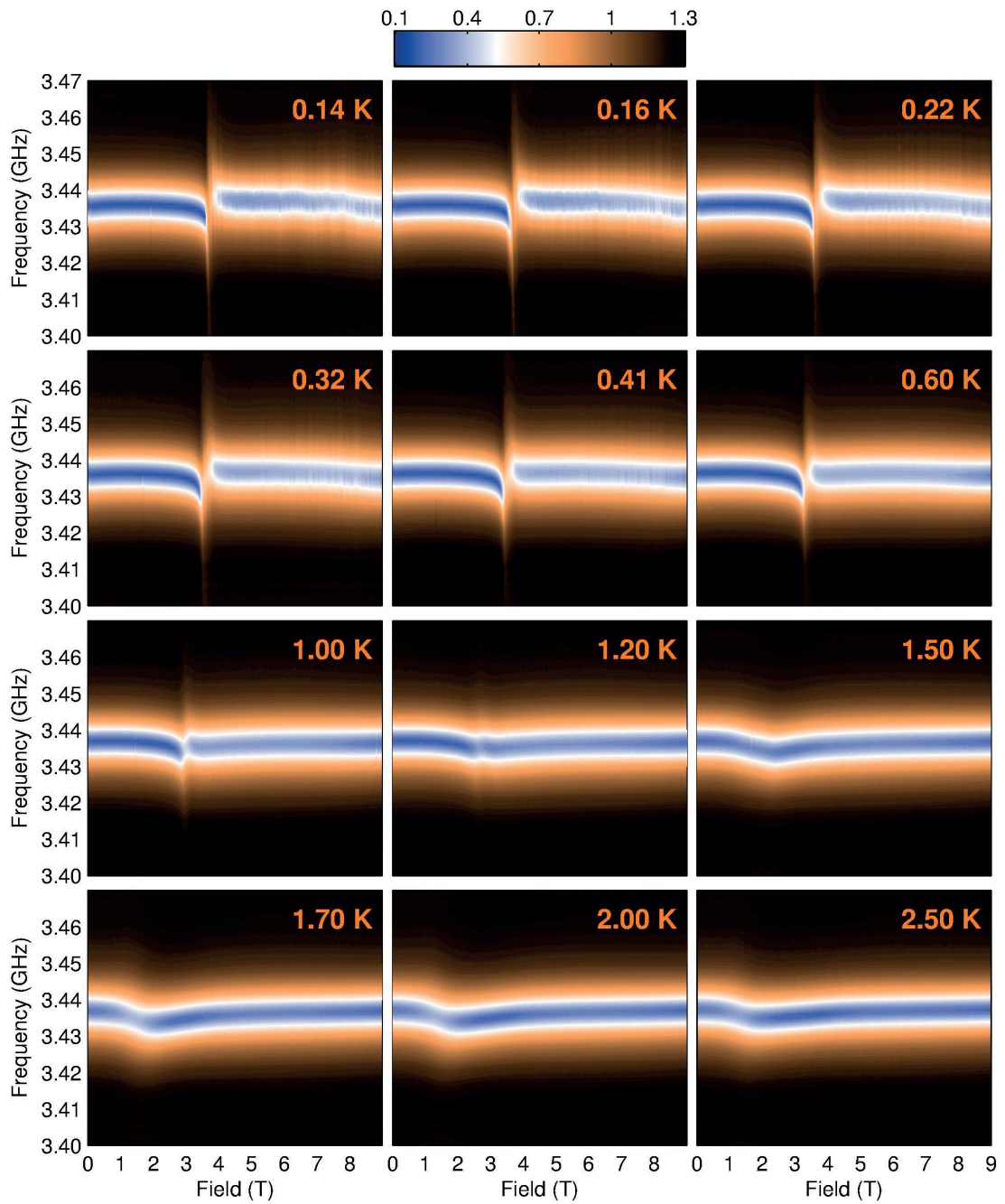
Figure 4.2: Frequency-field map of the experimental S_{11} parameter, which is the ratio of the reflected to the input power, around the fundamental frequency of a resonator loaded with the single-crystal sample. The anomaly corresponds to the expected resonance field for the frequency of 3.436 GHz.
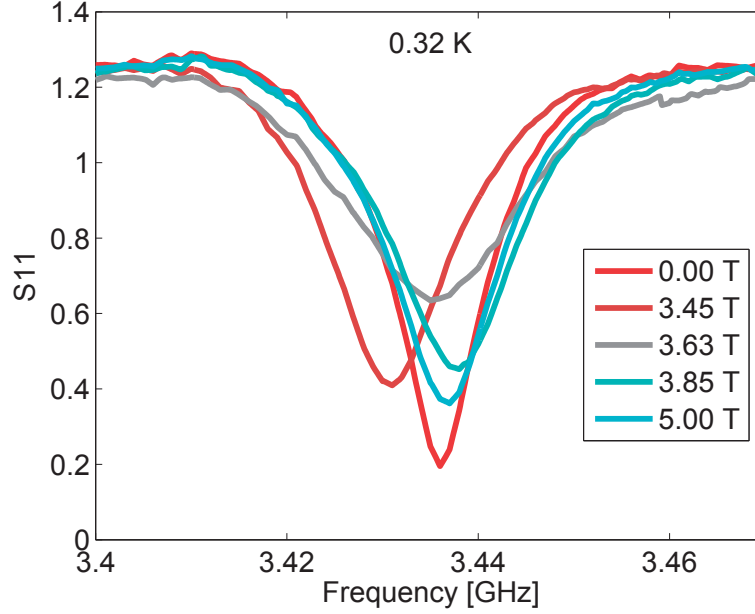
Figure 4.3: Frequency dependence of S_{11} at different fields as a signature of resonance.

while keeping the background constant. Frequency sweeps at a couple of characteristic fields are shown in Fig. 4.3. Resulting fitting parameters f_0 and Δf are then used to calculate the quality factor $Q = f_0/\Delta f$. Q and f_0 are plotted at each field between 0 and 9 T for all measured temperatures in Fig. 4.4. The linewidth at zero-field is $\Delta f = 14$ MHz ($Q \simeq 250$) which then becomes broader near the resonant field ($Q \simeq 100$) as shown in Fig. 4.3. The resonator line is repelled by 4 MHz on each side from the unperturbed resonator frequency as shown in Fig. 4.4.

The resonant field can be determined either from a peak position of $1/Q$ or from f_0. The resonant frequency f_0 shows a characteristic first derivative of the absorption spectrum at the resonant field. Figure 4.4 shows that the absorption peak in $1/Q$ is shifting to lower resonant fields with increase of temperature. This trend is expected because the magnetization, which roughly determines the excitation frequency ($\Delta E_{Hyp} = A\langle J\rangle$), decreases with increase of the temperature or the transverse magnetic field. The amplitude of the absorption $1/Q$ peak is getting weaker as the temperature is increased. This is explained by a smaller absorption of the microwave power at higher temperature due to a smaller difference in population between the energy levels (Boltzmann distribution).

The absorption peak in $1/Q$ is present at all temperatures in the ferromagnetic phase, up to the phase transition, 1.5 K. The absorption peak position agrees very well with the calculated resonance fields for 3.436 GHz resonator. The detailed comparison will be shown later in the thesis.
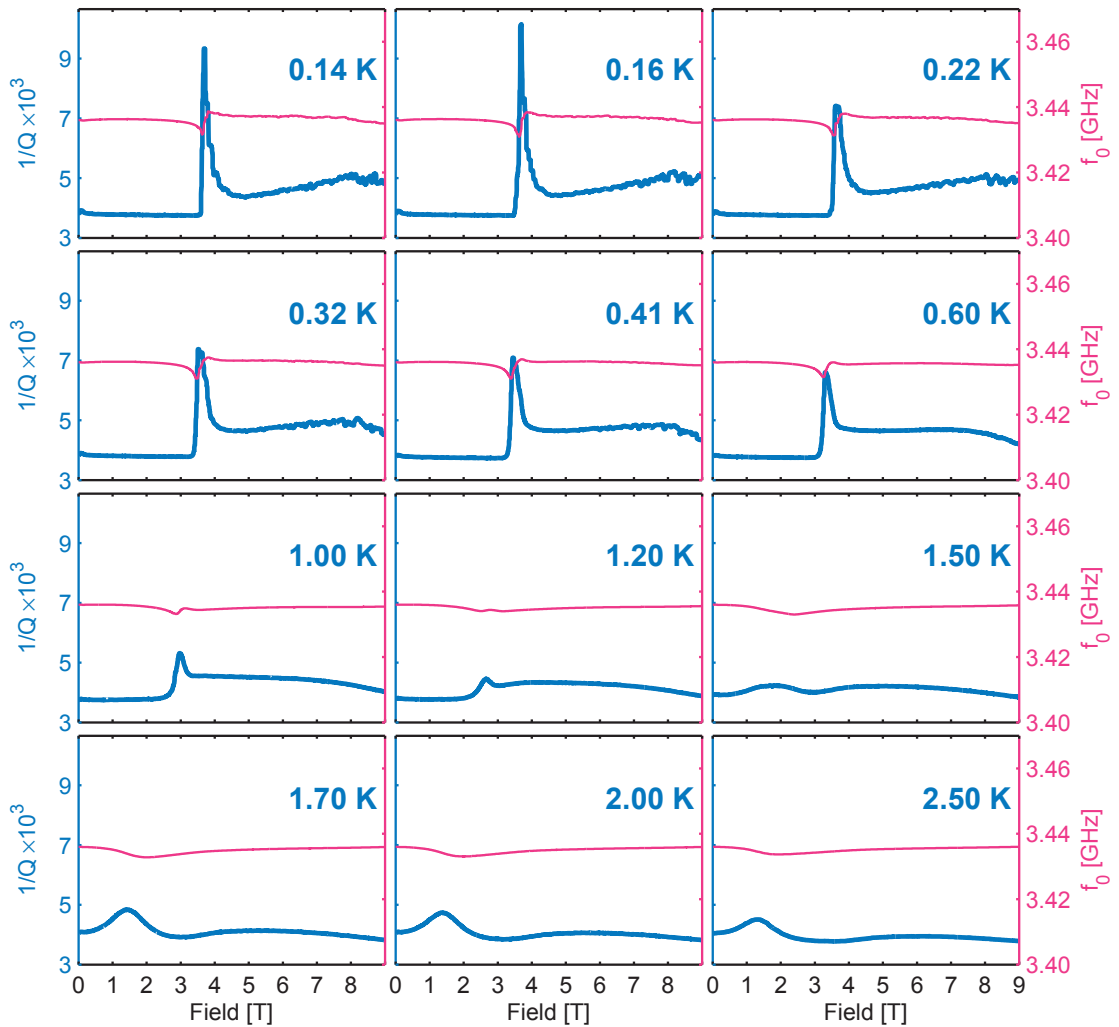
Figure 4.4: The quality factor Q and the resonant frequency f_0 as a function of the transverse magnetic field, at different temperatures for the 3.4 GHz resonator.

The width of the absorption line $\Delta B_{Resonant}$ is 250 mT and it does not change much with the temperature. It is a very broad asymmetric absorption line, because it is composed of multiple absorption lines. Since there are 8 non-equidistant hyperfine levels, there are 7 transition frequencies between them which should result in 7 separated peaks, but because difference between peaks is within the lifetime of the excitation it is not possible to resolve the 7 transitions. In the first approximation we can think of it as the nuclear-spin transitions which conserve the Ho^{3+} electronic spin, although we shall later show that this is not exactly the case because the entanglement between the electronic and nuclear spin states makes it impossible to separate electronic and nuclear subsystems. This entanglement can be ignored if the spins are highly polarized, but it has a maximum near the quantum phase transition.

4.1.2 Magnetic resonance at 3.9 GHz

To track the magnetic resonance at the different frequency we made a new resonator with the fundamental frequency of 3.924 GHz. All measurements carried out with this resonator are shown in Fig. 4.5. Frequency scans have been done in the range from 3.875 to 3.975 GHz. Again, there is the avoided crossing at the resonant field, but this time at the lower resonant field 2.9 T, at the base temperature 0.13 K. That is exactly what our calculations predict, as one can see from Fig. 4.1, the higher the excitation frequency the lower the resonant field.

The quality factor Q, shown at Fig. 4.6, is extracted from the fitting frequency scans to the Lorentzian curves, as explained in the chapter 3.6. In the zero field $Q \simeq 210$ ($\Delta f = 18$ MHz), while at the resonant field it decreases to $Q \simeq 60$, at 0.13 K. The absorption spectrum $1/Q$ shows a peak at the resonant field. The resonant field is reduced with an increase of temperature. The resonance peak amplitude is weaker as we increase the temperature to the phase transition T_C and disappears in the paramagnetic phase above 1.5 K. The width of the absorption line $\Delta B_{Resonant}$ is 250 mT, at the lowest temperature 0.13 K and is temperature independent. The resonant frequency f_0 as a function of the field shows characteristic first derivative of absorption spectrum, where f_0 shifts $\pm$ 7 MHz away 3.924 GHz.

4.1.3 Off-resonant susceptibility at 1.7 GHz

The magnetic resonance at frequencies below 2 GHz should be very weak or negligible at temperature of 0.3 K or lower, according to our calculations shown in Fig. 4.1. To probe the system in the non-resonant region we made a resonator with a fundamental frequency of 1.681 GHz. Measurements performed at different temperatures show no sign of avoided crossing characteristic for magnetic resonance, as we have seen in 3.4 and 3.9 GHz resonators. There is a shift in the resonant frequency of the resonator
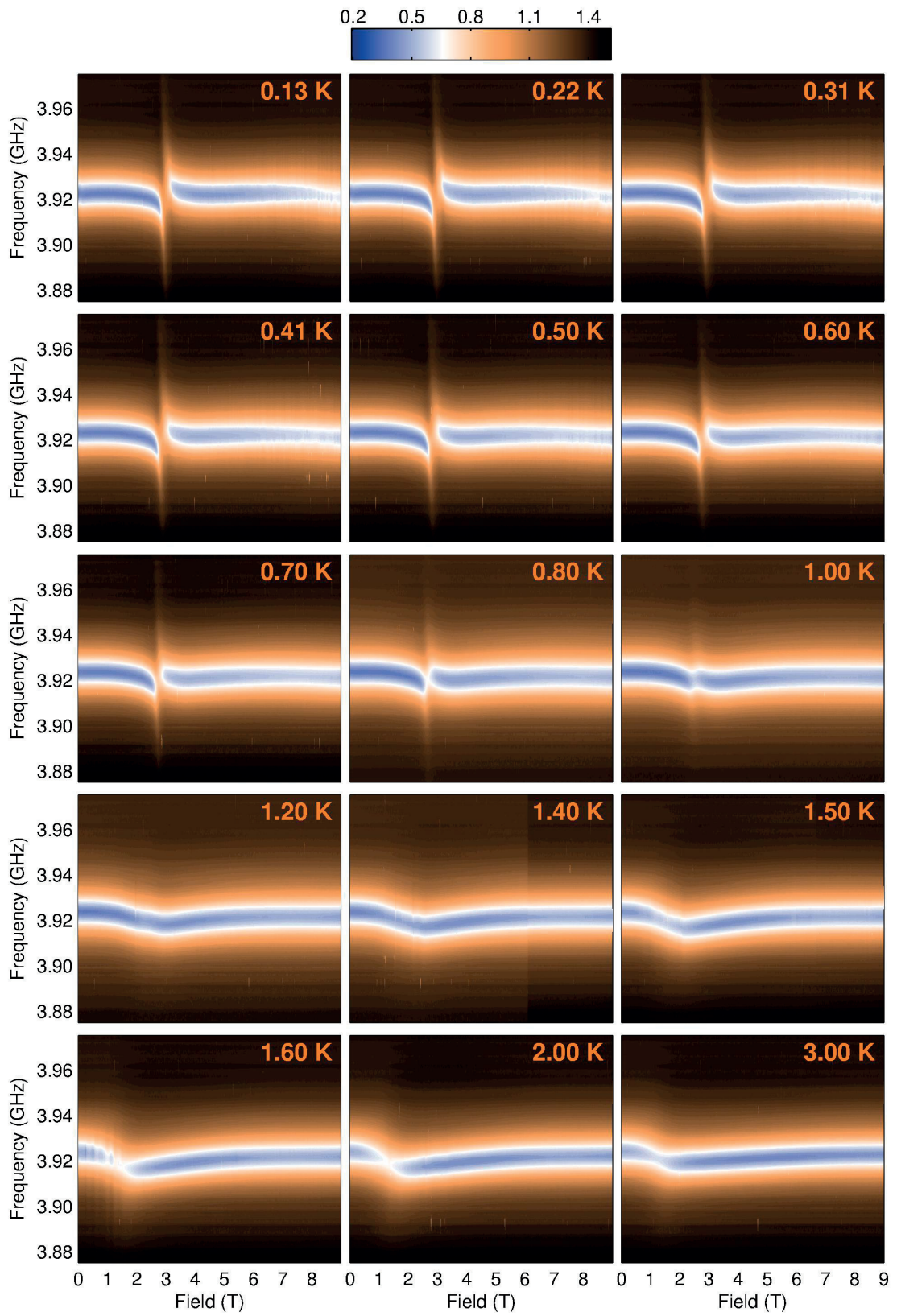
Figure 4.5: Frequency-field map of the experimental S_{11} parameter for the 3.9 GHz resonator.
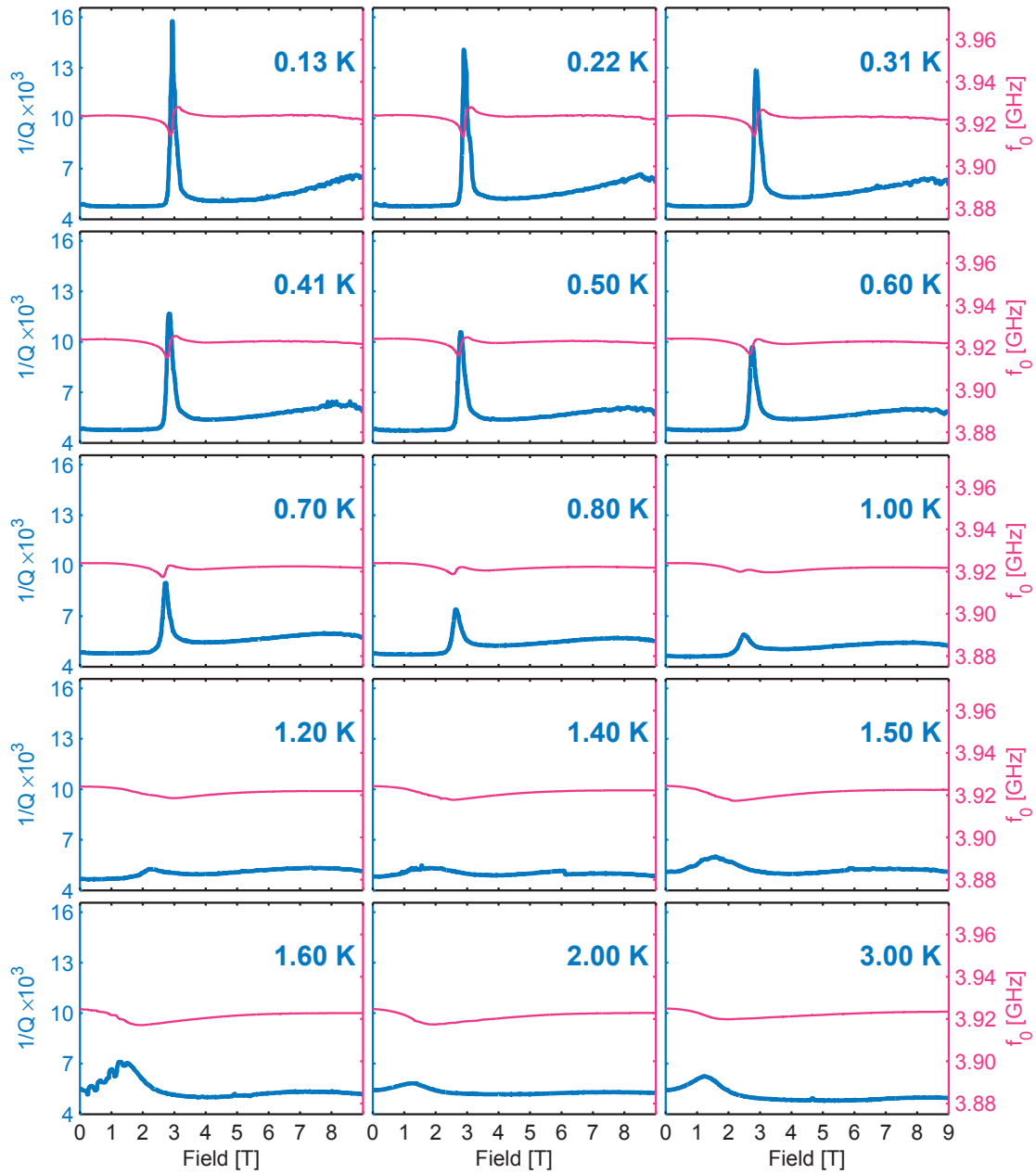
Figure 4.6: The quality factor Q and the resonant frequency f_0 as a function of the transverse magnetic field, at different temperatures for the 3.9 GHz resonator.
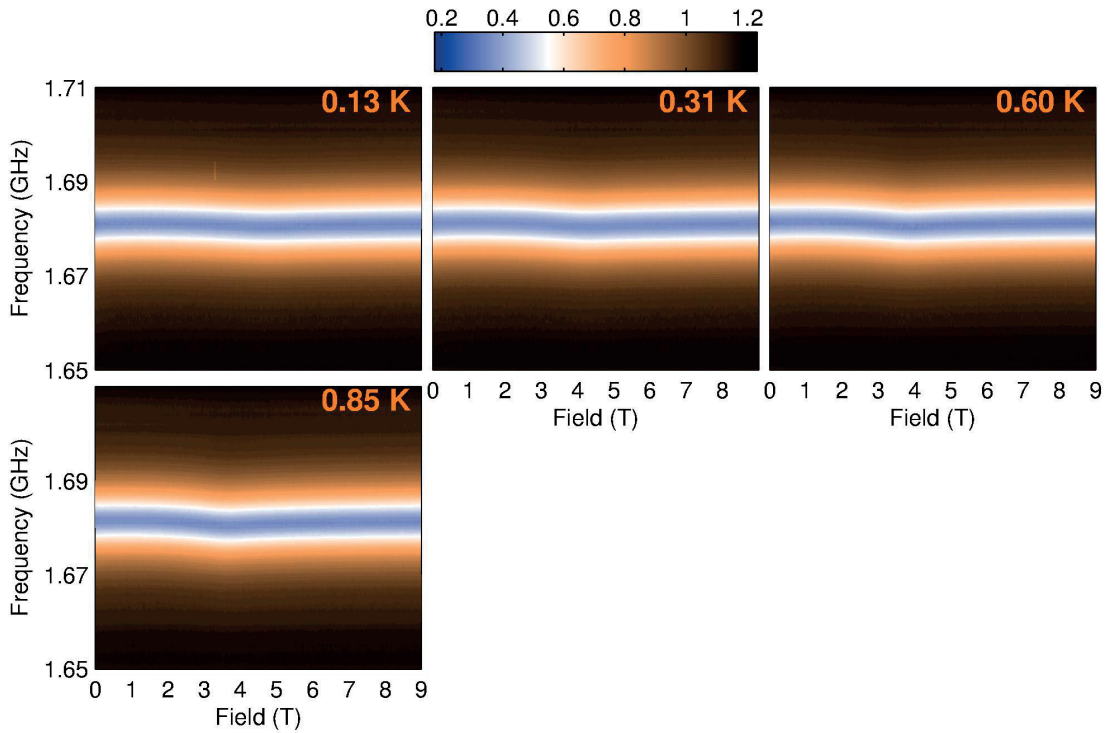
Figure 4.7: Frequency-field map of the experimental S_{11} parameter, which is the ratio of the reflected to the input power, around the fundamental frequency of the 1.7 GHz resonator loaded with the single-crystal sample.
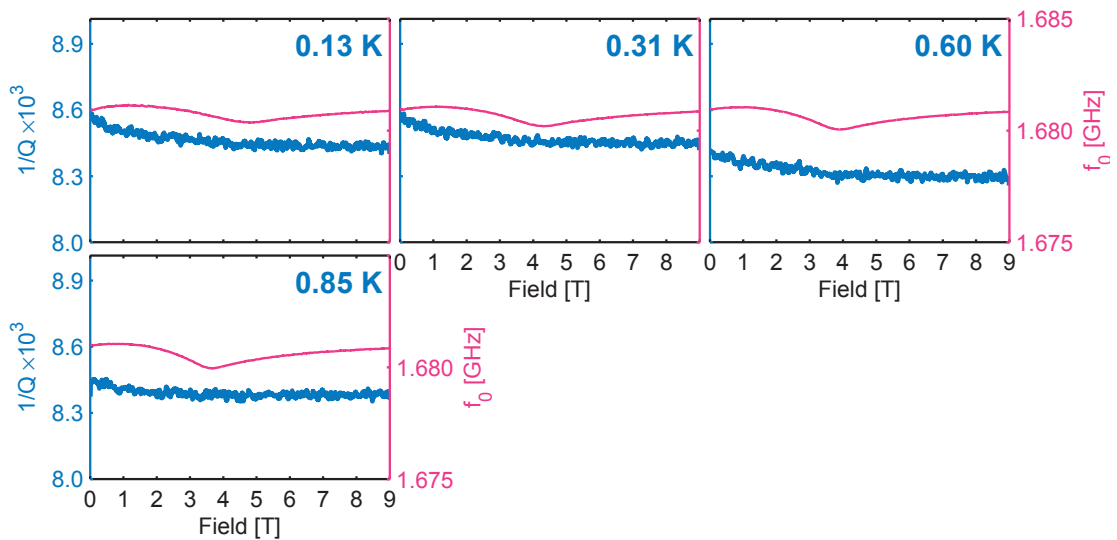

Figure 4.8: The quality factor Q and the resonant frequency f_0 as a function of the transverse magnetic field, at different temperatures for the 1.7 GHz resonator.

67

at the quantum phase transition. Even though there is no resonance at 1.681 GHz, the resonator is still sensitive to change in susceptibility of the sample. A calculated real part of susceptibility shows a peak at the quantum phase transition, which is observed as a dip in the resonant frequency f_0 (Fig. 4.7). To quantify this we fit the frequency scans with the Lorentzian to extract Q and f_0, which is shown on Fig. 4.8. This experimental result is expected since the calculations predicted that there will be no resonance at this frequency. Our experimental setup can be used in off-resonance regime to measure the real part of susceptibility and map the phase diagram, which will be demonstrated in later in the thesis.

4.1.4   Off-resonant susceptibility at 5.6 GHz

To further understand our sample, we built a resonator which measures the response at energy higher than the absorption spectrum (Fig. 4.1), with a fundamental frequency of 5.600 GHz. Our calculations predicted no magnetic resonance at 5.6 GHz, except for weak absorption when the excitation frequency corresponds to transition to next nearest energy level. This weak absorption appears visible on our colour plot in Fig. 4.1, but actually the amplitude too small to be detected by our setup. Figure 4.9 shows the spectrum recorded with the network analyzer as a function of the field at different temperatures. Similar to non-resonant measurements at 1.7 GHz, there is no avoided crossing at 5.6 GHz. Extracting the Q and f_0 by fitting the measured data we get the results shown in Fig. 4.10. Again, there is no absorption in the ordered phase, below 1.5 K. But there is a clear dip in the resonant frequency at the critical field at temperatures below 1.5 K. It is noticeable that there is some absorption in the paramagnetic phase. We shall discuss this further later in the thesis.

4.1.5   Off-resonant susceptibility at 4.5 GHz

Finally, we wanted to probe LiHoF$_4$ spins at the highest possible resonant energy. According to our original calculations, the highest frequency at which the system goes through the resonance was supposed to be around 4.5 GHz, so we made a resonator with the fundamental frequency of 4.447 GHz. We expected to see the strongest absorption when we cut parallel to the resonance, but we actually did not see much of the absorption, especially at the base temperature, 0.13 K. The measured reflected signal looks very similar to the 5.6 GHz resonator. We concluded that we actually missed the resonance by setting up the frequency too high, above all resonance energy levels. This can be explained by adjusting the hyperfine constant, but more on that later in the thesis.

There is a new feature which appears at 4.5 GHz (Fig. 4.11) at low fields and temperatures below 0.9 K. We extract Q and f_0 and plot it as a function of the field at different
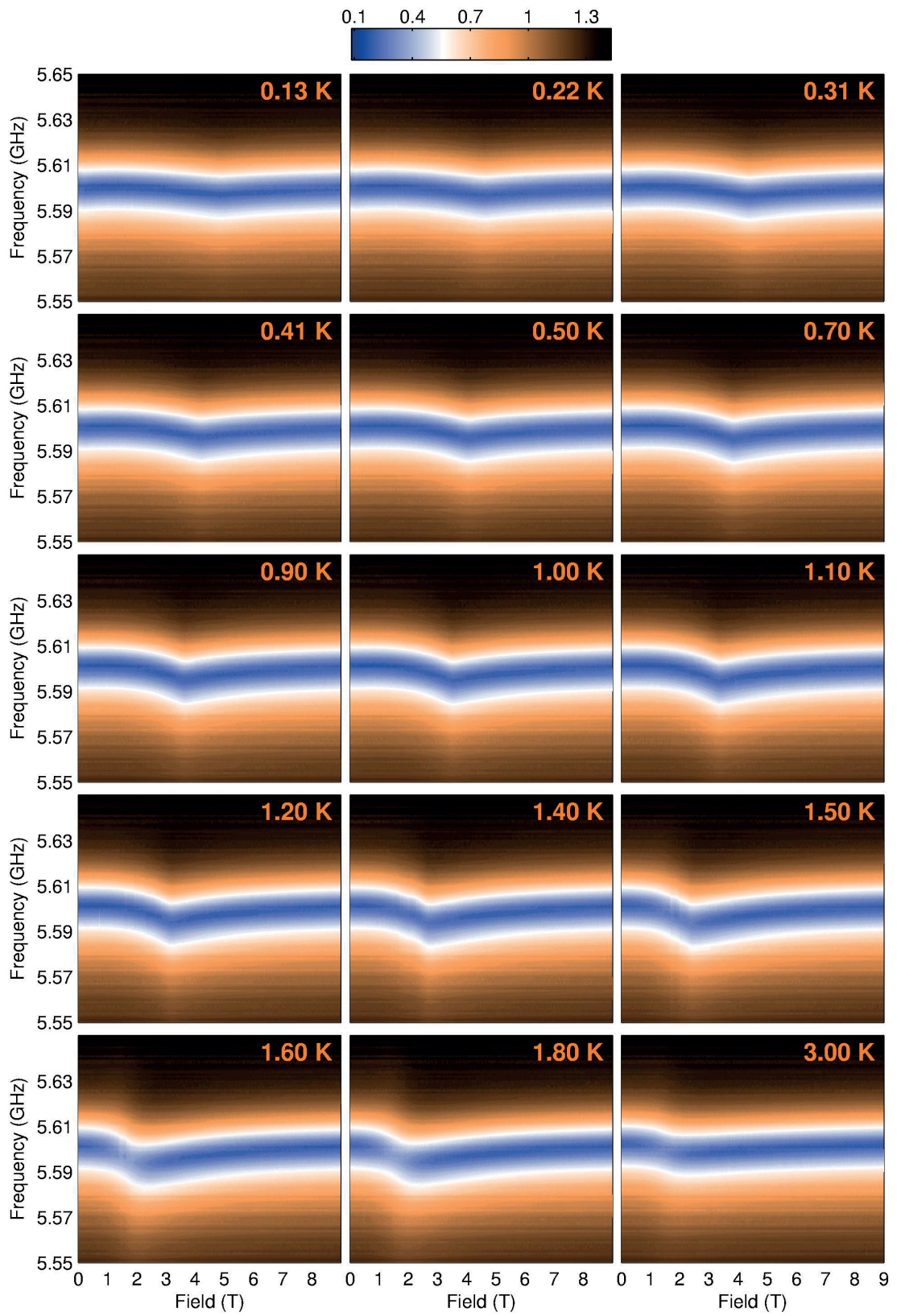
Figure 4.9: Frequency-field map of the experimental S_{11} parameter for the 5.6 GHz resonator.
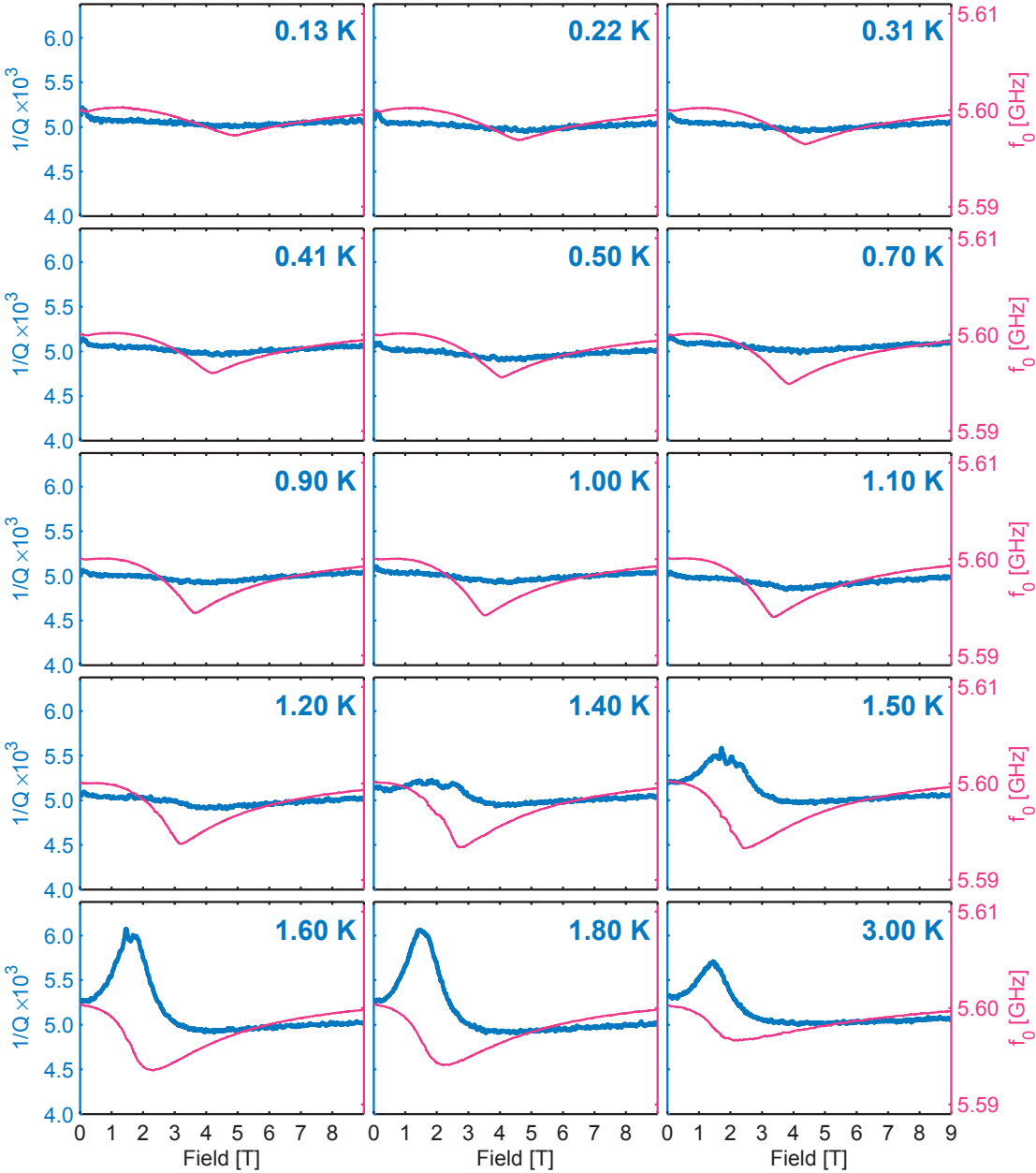
Figure 4.10: The quality factor Q and the resonant frequency f_0 as a function of the transverse magnetic field, at different temperatures for the 5.6 GHz resonator.

Figure 4.11: Frequency-field map of the experimental S_{11} parameter for the 4.5 GHz resonator.

71

Figure 4.12: The quality factor Q and the resonant frequency f_0 as a function of the transverse magnetic field, at different temperatures for the 4.5 GHz resonator.
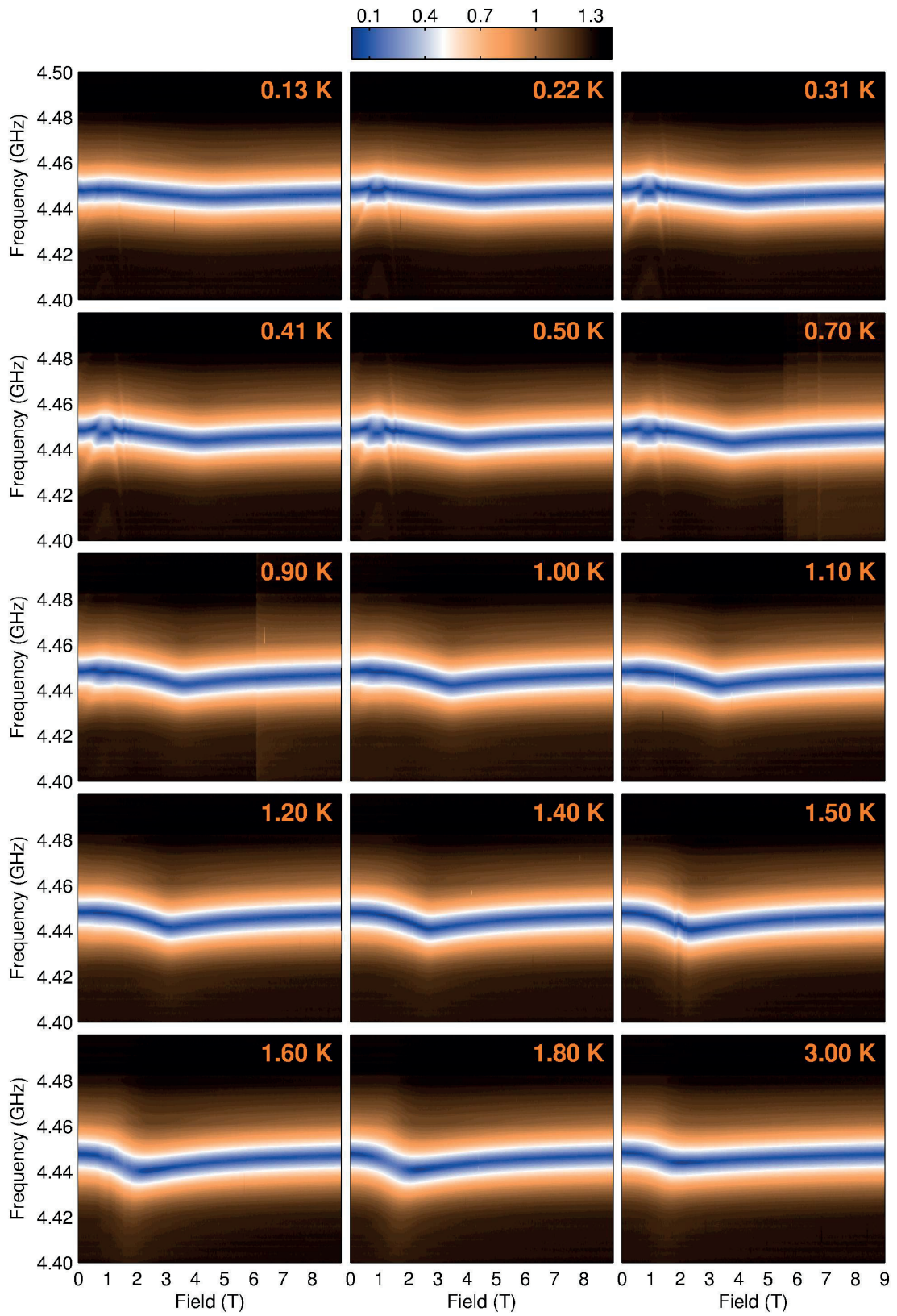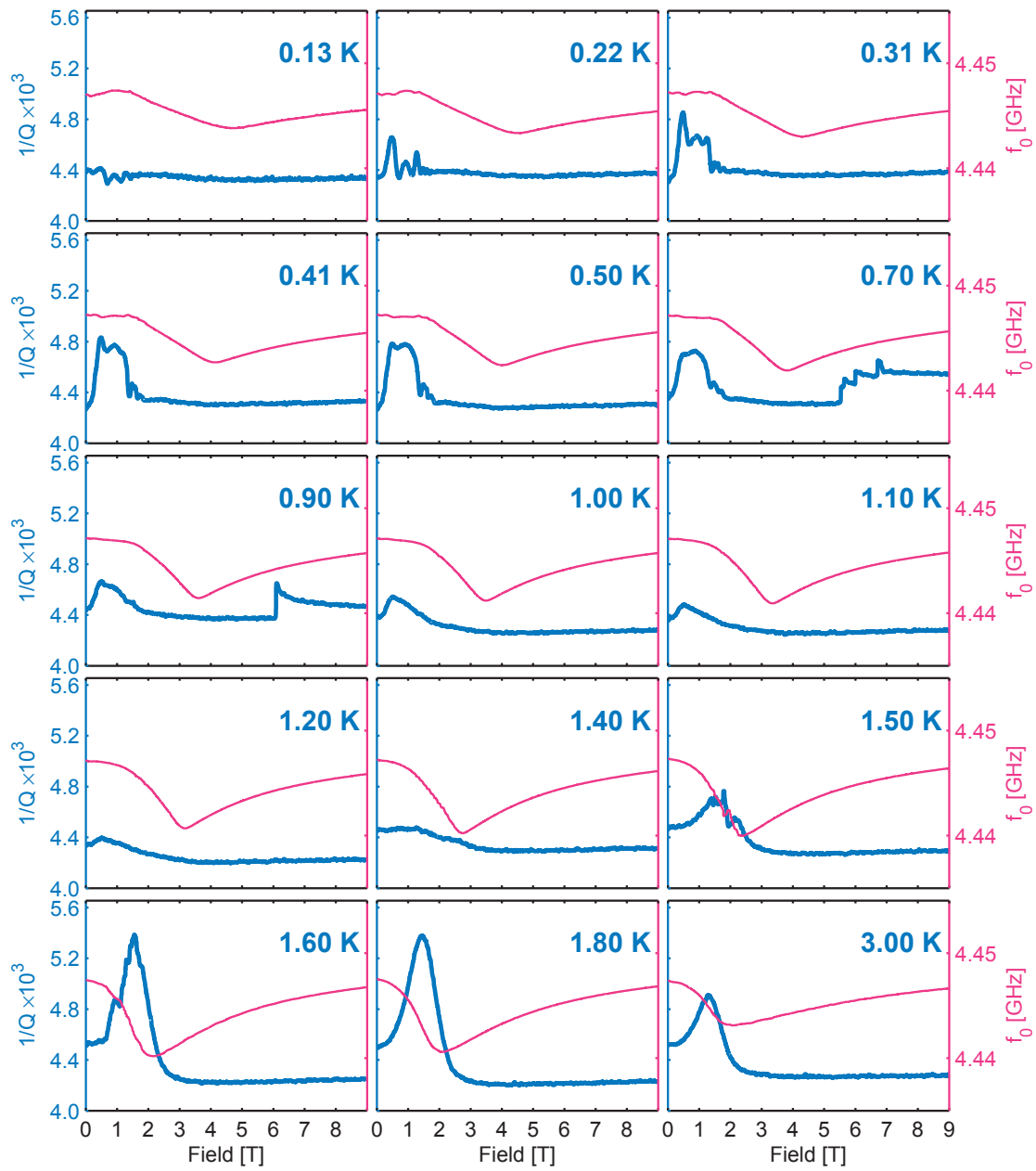
temperatures (Fig. 4.11). Oddly, this does not result in a large change of absorption $1/Q$ (Fig. 4.12), at least when compared to signal at 3.4 and 3.9 GHz (Fig. 4.13a). Also, the pattern in the frequency-field map shown in Fig. 4.11 is different from avoided crossing which appears at 3.4 and 3.9 GHz. From frequency-field map of absorption at 0.3 K in Fig. 4.1 we see that the field-scan at 4.5 GHz is just above the resonant frequency at low fields. The small change in $1/Q$ could therefore be attributed to a small change in the imaginary part of susceptibility (Fig. 4.1), since the experimental setup is sensitive to the a change in the absorption.

Since $1/Q$ shows absorption at low fields in ferromagnetic phase, minimum of resonant frequency f_0 is far enough that it is not affected by the absorption, so we can use f_0 to track the critical field at each temperature.

There is an anomaly at 0.7 and 0.9 K measurement between 6 and 9 T which can also be seen in raw frequency scans in Fig. 4.12 as a slightly brighter color of the high-field data. It seems that the data are corrupted so that the background is changed. Possible reason for this could be vibrations or similar. Since the fitting parameter background is fixed throughout the whole field scan, a change in the experimental background in the middle of the field scan would result in change in Q.

4.2   Data analysis and simulations

4.2.1   Hyperfine constant determination

If we compare low temperature (0.3 K) experimental data with calculations we see that the curve at 4.5 GHz is very different from calculations (Fig. 4.13a and Fig. 4.13b). There is a strong absorption in calculated data at low fields, which is much weaker in measured data.

We remember from Fig. 4.1 that the frequency of 4.5 GHz is at the very top of the predicted absorption spectrum. The energy difference between energy levels is, in the first approximation, determined by the hyperfine constant and the expectation value of the electron magnetic moment, $\Delta E_{Hyp} = A\langle J \rangle$. Since $\langle J \rangle$, in zero field, is determined by the crystal electric field, we could change the resonant frequency either by adjusting the crystal field parameters or by adjusting the hyperfine constant. Crystal field parameters and the hyperfine constant were determined from the same hyperfine resonance experiment [20]. By measuring the spacing between the hyperfine resonance lines Magarino *et al.* observed that the hyperfine constant is $A = 3.36$ μeV $\pm 2.1\%$. By decreasing the hyperfine constant in our simulations by only 3% of the cited value, the resonant frequency became smaller than 4.5 GHz, so that experiment with 4.5 GHz resonator never satisfies the resonance condition (which we show in Fig. 4.13c). The change of hyperfine constant did not significantly affect calculations
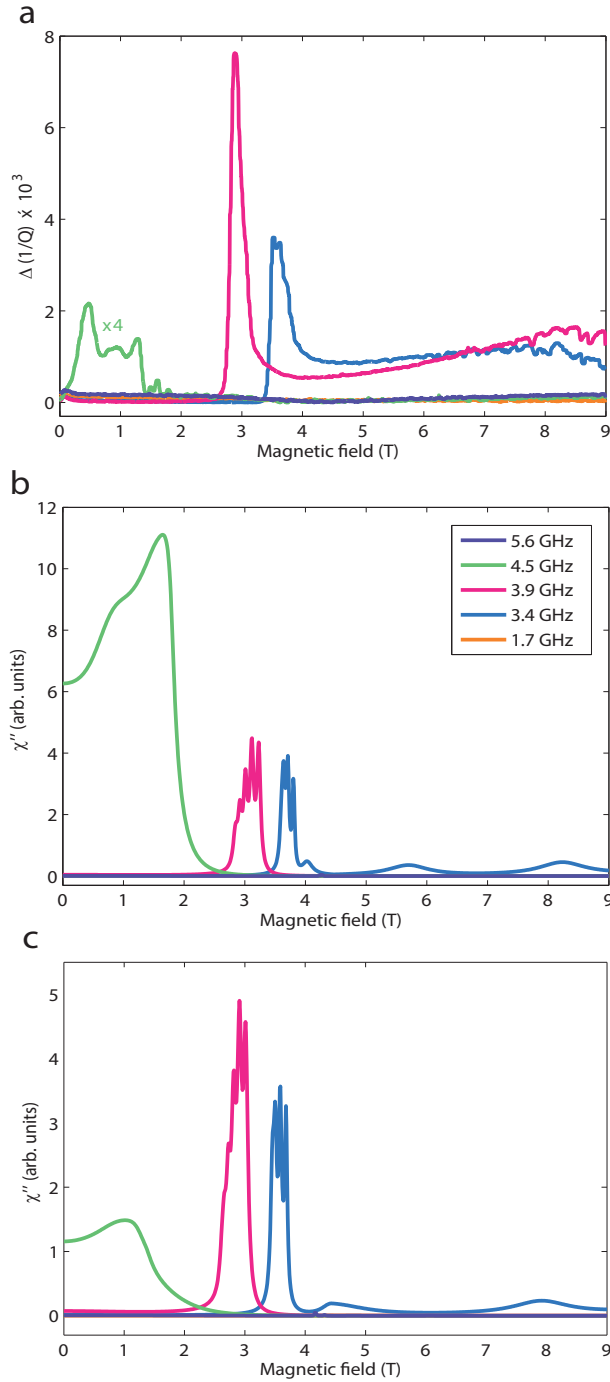
Figure 4.13: Comparison between **a)** measured absorption at 0.3 K, **b)** calculated absorption at 0.3 K with $A = 3.36\ \mu$eV and $\Gamma_{\alpha'\alpha} = 0.1\ \mu$eV, and **c)** calculated absorption at 0.3 K with $A = 3.26\ \mu$eV and $\Gamma_{\alpha'\alpha} = 0.1\ \mu$eV.

at other frequencies because they do not critically depend on it.

This shows that the nuclear-electronic magnetic resonance experiment, where we probe hyperfine levels directly, is very sensitive to small changes in the hyperfine constant. Original value of the hyperfine constant $A = 3.36\ \mu$eV was refined to $A = 3.26\ \mu$eV. In all calculations shown in this thesis we used the refined $A = 3.26\ \mu$eV.

The only free parameter in our model was the width of the peak in the absorption spectrum $\Gamma_{\alpha'\alpha}$. The width of $\chi''(\omega)$ in our simulations in Fig. 4.1 was set to $\Gamma_{\alpha'\alpha} = 0.1\ \mu$eV (lifetime $\tau \simeq 40$ ns) to best fit the absorption in the ferromagnetic phase. If we significantly reduce $\Gamma_{\alpha'\alpha}$, we would recognise the hyperfine structure with 7 distinct peaks. Comparison between calculations and experiment at 0.3 K is shown in Fig. 4.13a and Fig. 4.13c. We see that the model reproduces the peaks and features of the measured absorption up to critical field around 4.5 T. We shall show more detailed comparison later in the thesis.

4.2.2 Temperature and field dependence

After fixing the hyperfine constant $A = 3.26\ \mu$eV and the lifetime of states to $\Gamma_{\alpha'\alpha} = 0.1\ \mu$eV we look into the temperature dependence of the two resonators with the resonance at 3.4 and 3.9 GHz (Fig. 4.14).

There is no rescaling of experimental or measured data. Lifetime of excitations $\Gamma_{\alpha'\alpha}$ and the hyperfine constant A were kept fixed. Calculations in Fig. 4.14 are in very good agreement with measurements. The resonance peak in $1/Q$ can be reproduced by our calculations.

To better visualise the absorption at 3.4 and 3.9 GHz, we show the absorption peak as a point in temperature vs. field diagram on Fig. 4.15. We plot the calculated peak position on the same figure as a band whose upper boundary corresponds to calculations with the hyperfine constant A increased by 3% and the lower band boundary corresponds to A decreased by 3%, relative to the new adjusted value $A = 3.26\ \mu$eV. To make a distinction between the magnetic resonance condition and the phase transition, we also plot the calculated phase boundary (note that mean-field calculations overestimate T_C at 1.8 K).

We can also compare the calculated resonant bands directly with the colormap of absorption measured as a function of the field and temperature at 3.4 and 3.9 GHz, shown in Fig. 4.16. We see that the maximum of absorption (dark color) corresponds to the calculated band in Fig. 4.15.

To show how sensitive the resonant field is to the value of the hyperfine constant A, we recalculated the resonant field with A varied by $\pm10\%$ for 3.4 GHz and from -6% to
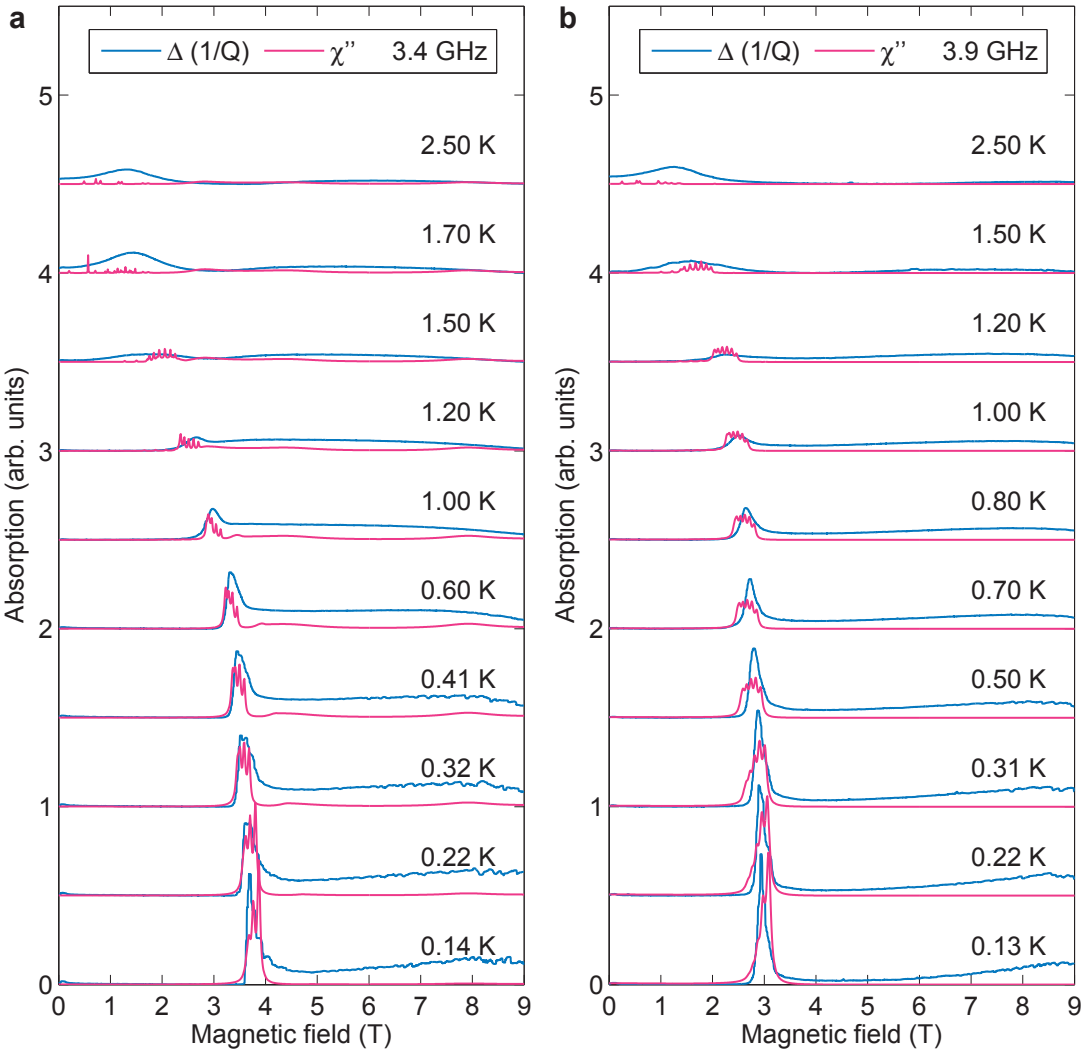
Figure 4.14: Temperature evolution of the magnetic resonance spectra from 0.13 K to 2.5 K from experiments (blue) and calculations (red) using excitation frequency of **a)** 3.4 GHz and **b)** 3.9 GHz.
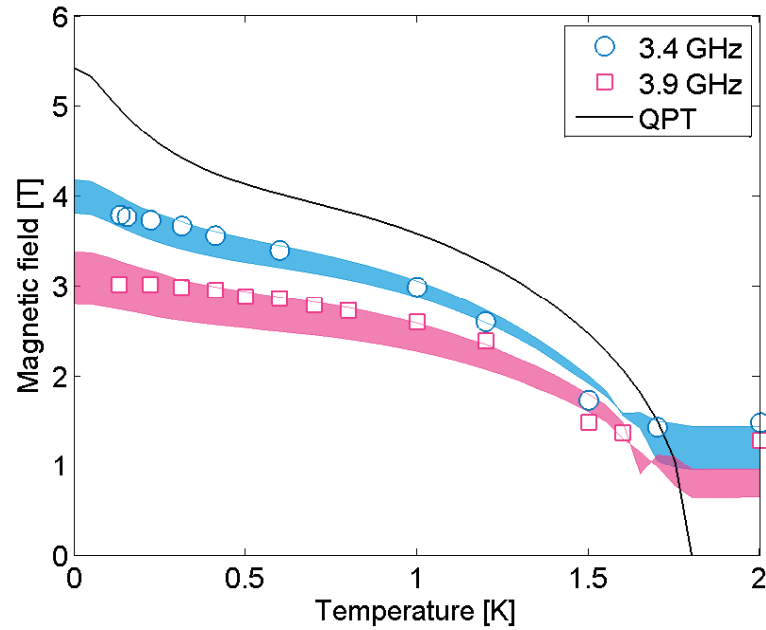
Figure 4.15: The resonance field as a function of temperature for two different frequencies, 3.4 GHz (blue) and 3.9 GHz (red). Symbols denote experimentally obtained values while the coloured bands are calculations using hyperfine constant in the range of $\pm 3\%$ from the value used in calculations $A = 3.26$ μeV. Black line reproduces the calculated phase boundary.

Figure 4.16: Colorplot of measured absorption $1/Q$ as a function of temperature and field at **a**) 3.4 and **b**) 3.9 GHz.

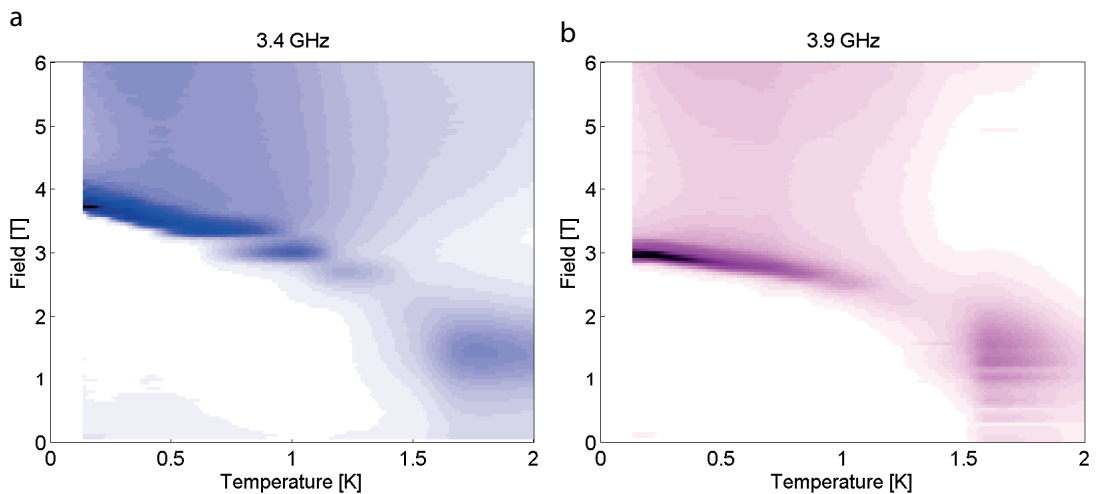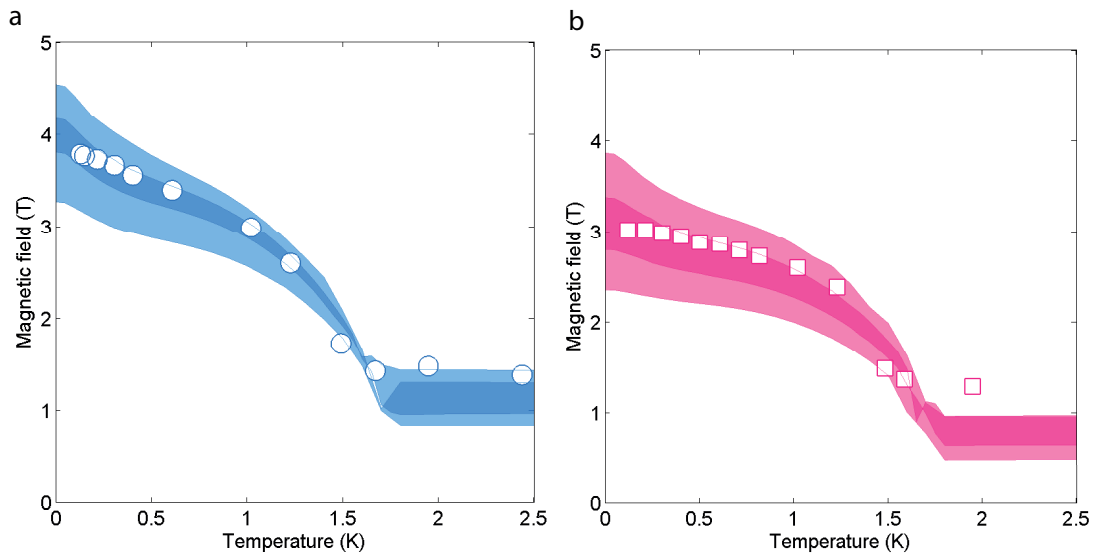Figure 4.17: Temperature evolution of the resonant field at 3.4 and 3.9 GHz. **a**), Dark blue band shows resonant field as a function of temperature calculated at fixed frequency of 3.4 GHz by using the hyperfine constant, A, in the range of ±3% of the value used in this paper. Light blue band shows resonant fields for A in the range of ±10%. **b**), Dark red band shows resonant field at the fixed frequency of 3.9 GHz based on A in the range of ±3%. Light red band shows resonant fields where A was varied by -6% and +10% of the optimal value. There is no resonance at 3.9 GHz if A is decreased by more than 6% because the resonator frequency is larger than the difference between energy levels.

Figure 4.18: Comparing **a)** measured absorption with **b)** calculations at all frequencies at 0.3 K. Absorption was calculated with $\Gamma_{\alpha'\alpha} = 1\ \mu$eV.

+10% for 3.9 GHz excitation (Fig. 4.17).
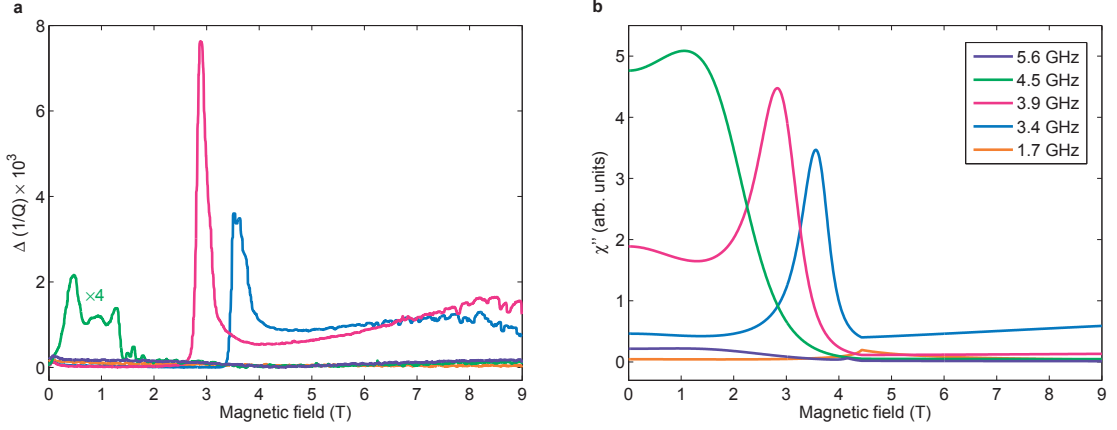
4.2.3 Lifetime of the states

It is evident from Fig. 4.14 that calculations do not agree with the experiment above the critical field and above the critical temperature. There are strong correlations above T_C and H_C which are not accounted for in the mean-field calculations. One could make the calculations which take these correlations into account, but that is out of the scope of this thesis. If we stay within the mean-field approximation, we can ask how much do we have to change the lifetime of the nuclear-electronic states to take the correlations into account.

Let us first consider absorption above H_C at low temperatures. In the ferromagnetic phase the width of excitation was fixed to $\Gamma_{\alpha'\alpha} = 0.1\ \mu$eV which corresponds to lifetime of $\tau \simeq 40$ ns. We recalculated the absorption spectrum for measured frequencies with 10 times shorter lifetime, $\tau \simeq 4$ ns, *i.e.* 10 times larger energy width of nuclear-electronic states, $\Gamma_{\alpha'\alpha} = 1\ \mu$eV (shown in Fig. 4.18). Shorter lifetimes reproduces the tail measured above 4.5 T with 3.4 and 3.9 GHz resonators. Both calculated absorptions, for 3.4 and 3.9 GHz, increase as a function of field, which is observed in experimental data. 10 times shorter lifetime of states reproduces the absorption above H_C.

Let us now consider the absorption at temperatures above T_C. There is a weak absorption in the paramagnetic phase, at temperatures above 1.5 K, between 1 and 2 T with all resonators (Fig. 4.19a). Since calculated peaks with width of $\Gamma_{\alpha'\alpha} = 0.1\ \mu$eV were too sharp to fit our measurements we increased it by factor of 10 in Fig. 4.19b and by factor of 100 in Fig. 4.19c and compared calculations with the experiment. Calculations with $\Gamma_{\alpha'\alpha} = 10\ \mu$eV *i.e.* $\tau \simeq 0.4$ ns (shown in Fig. 4.19c) reproduce the low field (0 to 3 T) part

a

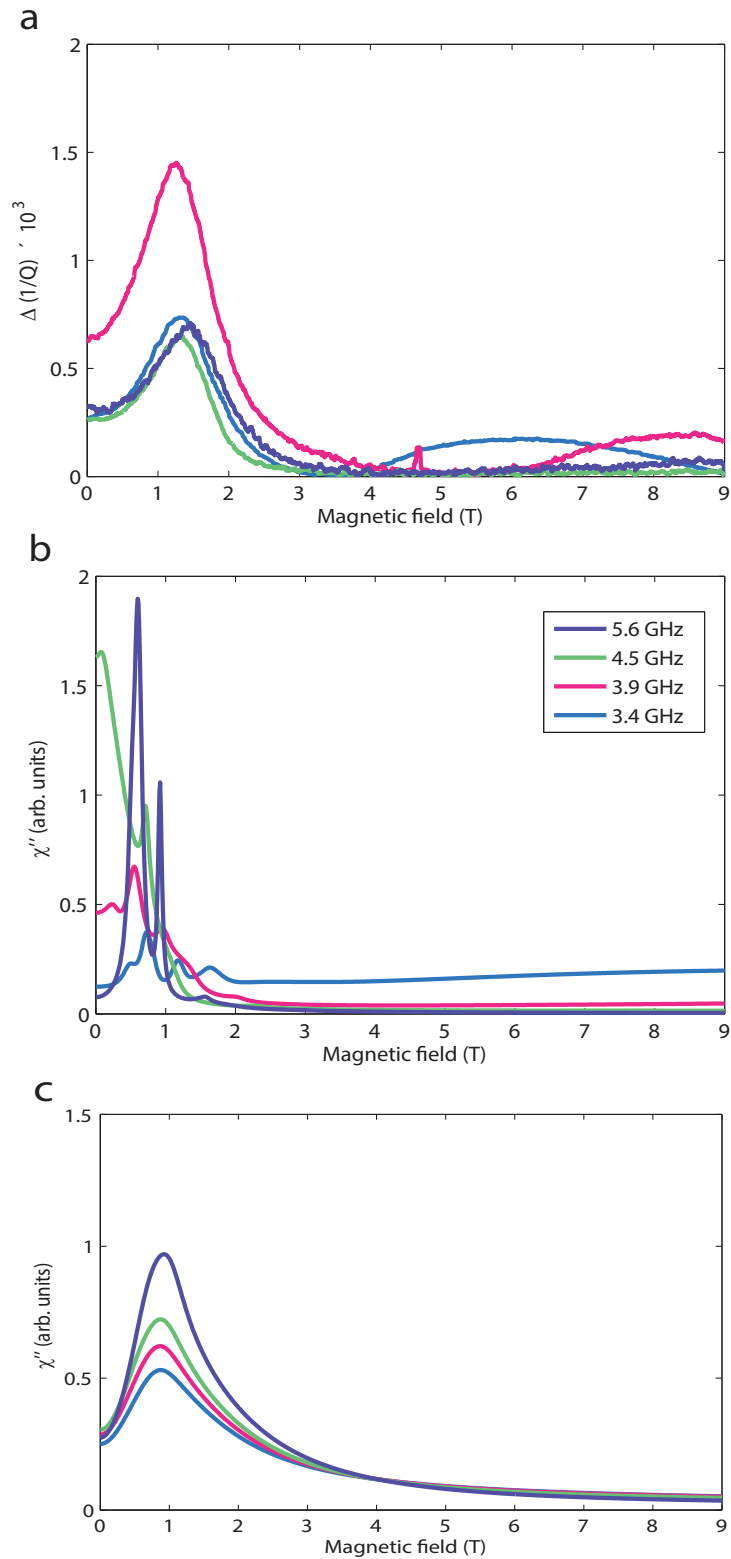
b

c

Figure 4.19: Comparison between **a)** measured absorption at 3 K, **b)** absorption was calculated at 3 K with $\Gamma_{\alpha'\alpha} = 1\ \mu$eV and **c)** absorption was calculated at 3 K with $\Gamma_{\alpha'\alpha} = 10\ \mu$eV.
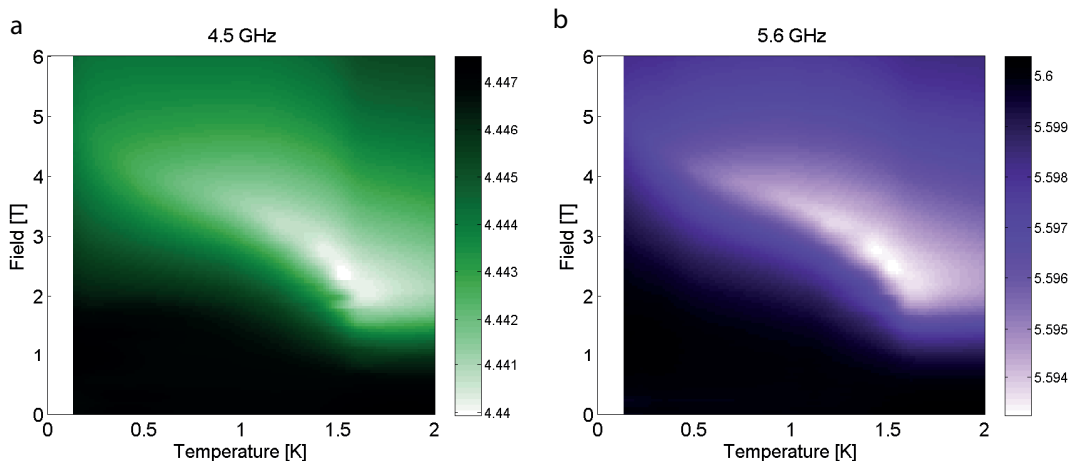
Figure 4.20: Colormap of the resonant frequency at **a,** 4.5 GHz and **a,** 5.6 GHz where white is minimum and black is maximum of the resonant frequency as a function of the field and temperature.

of the spectrum, at all frequencies, while calculations with $\Gamma_{\alpha'\alpha} = 1$ μeV *i.e.* $\tau \simeq 4$ ns (shown in Fig. 4.19b) reproduce the high-field tail in absorption measured at 3.4 and 3.9 GHz.

4.2.4 Off-resonant measurements

The resonators with f_0 of 1.7, 4.5 and 5.6 GHz show no absorption because they have the fundamental frequency too large or too low to cross excitations (Fig. 4.1). Even though there is no absorption, the resonator is sensitive enough to measure a change in the susceptibility of the sample across the phase transition. The phase diagram can be mapped by tracing the minimum in resonant frequency of the resonators (Fig. 4.8, 4.10, 4.12). The colormap in the Fig. 4.20 shows the resonant frequency f_0 (represented with green or purple color) as a function of the field at different temperatures, for 4.5 and 5.6 GHz resonators. The field at which f_0 is minimal (white color) corresponds to the critical field H_C.

We extract H_C as a function of temperature for every measured resonator and plot it on top of the mean-field phase boundary and the previous measurements of the phase boundary from literature [16] (Fig. 4.21). There is a very good agreement of measurements at all frequencies with theory and literature up to T$_C$, 1.5 K. It is a longstanding problem that mean-field calculations overestimate the T$_C$ at low fields in the phase diagram [22]. It is peculiar that our measurements stop tracing the phase transition at 1.5 K and 2.5 T, exactly where mean-field calculations fail. Explanation for this might be in the temperature dependence of the hyperfine energy levels (Fig. 4.22) which shows that hyperfine levels begin to be appreciably split only below 1.6 K, while between 1.6 and 1.8 K there are still were close in energy. Since at 1.6 K hyperfine levels
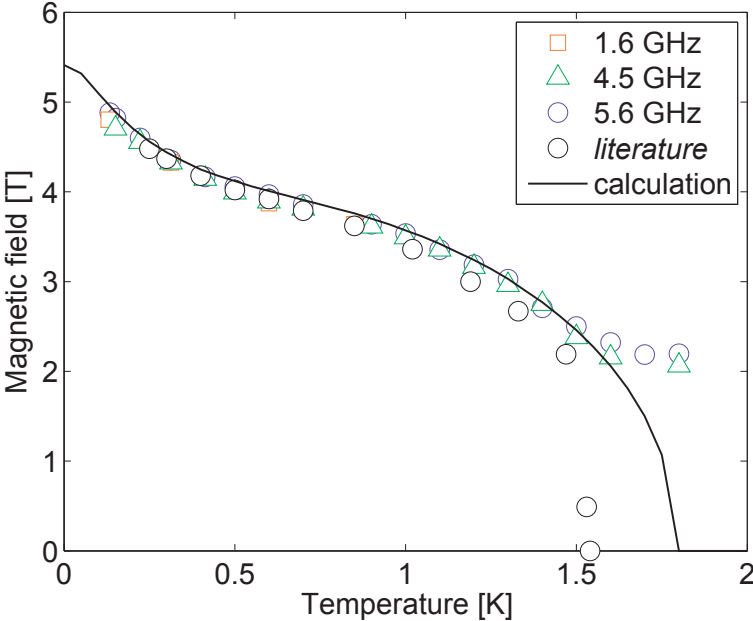
Figure 4.21: Minimum of the resonant field at measured frequencies compared with the calculated phase transition and literature measurements data.
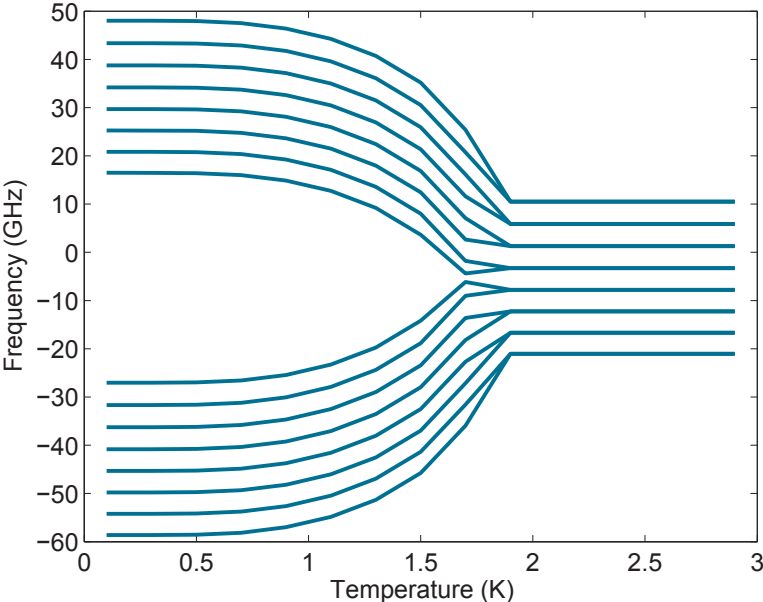

Figure 4.22: Temperature dependence of the lowest 16 energy levels in zero-field.
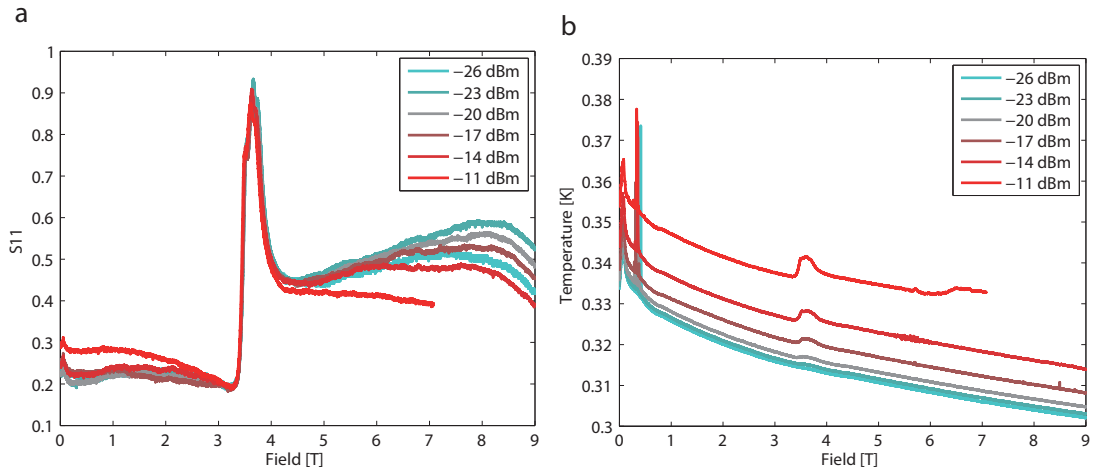
Figure 4.23: **a**) Reflected signal S_{11} as a function of field at 0.3 K. **b**) Sample temperature as a function of applied field.

are almost equally populated, that could be the reason for the paramagnetic behaviour.

4.3 Power dependence of the magnetic resonance

In LiHoF$_4$ hyperfine coupling significantly alters the phase boundary at low temperatures below 0.3 K. It would be interesting if we could get insight into the non-equilibrium phenomena in the vicinity of the quantum phase transition through control of hyperfine coupling by microwave radiation. One could reduce or completely eliminate the hyperfine coupling by equally populating hyperfine states. The magnetic resonance is changing the population of states (between which it operates). If the excitation field is increased, the population of hyperfine states could be changed from Boltzmann distribution to equal population of all excited states. If all states are equally populated there would be no absorption of microwave field by the sample. This can be experimentally tested by increasing the excitation until the absorption of the sample stops increasing linearly. To do this kind of a test one should constantly excite the system at fixed frequency, so we used the fixed frequency experimental setup described in the chapter 3.3.

We show the results of the S_{11} reflected power normalised by the input power in Fig. 4.23. The input power was changed from -26 dBm to -11 dBm in steps of 3 dBm (3 dBm is equal to a factor of 2 difference in power). The amplitude of the peak at 3.5 T is a measure of the absorbed power. We see that the peak is not changing significantly with the increase of the input power, which means that it shows no signs of saturation. There is a small decrease of the peak intensity accompanied with a small shift of peak to lower fields. This can simply be due to heating of the sample by increased microwave radiation as shown in Fig. 4.23b. At higher temperatures, the difference between the
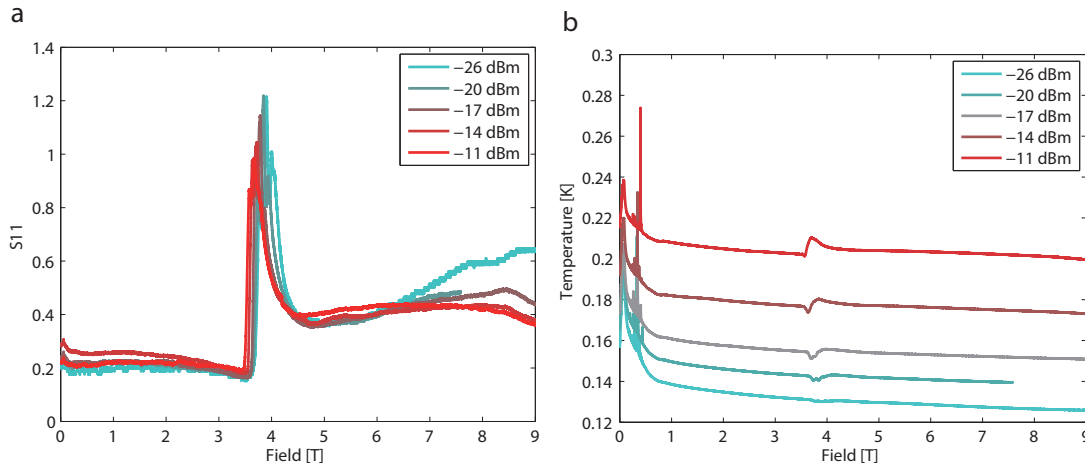
Figure 4.24: **a**) Reflected signal S_{11} as a function of field at 0.15 K. **b**) Sample temperature as a function of applied field.

population of energy levels is smaller so the absorption amplitude is smaller. Also, the effective spin $\langle J \rangle$ is smaller so the resonant field is smaller at higher temperatures. At transverse magnetic fields above 5 T, there are signs of saturation of the signal as excitation power is increased. To confirm this, we repeated the experiment at 0.15 K (Fig. 4.24).

The effect of the lower absorption amplitude and the resonant field shift is even more noticeable at 0.15 K, due to a relatively larger increase of a sample temperature at 0.15 K than at 0.3 K. The dilution refrigerator has less cooling power at a lower temperature to compensate for heating from microwave radiation and heat conductivity of copper is lower to remove the heat from the sample. Since the frequency is not changing - there is a continuous pumping on the sample spin system. The absorption of the microwave power is even witnessed in the sample thermometer when temperature peaks at the resonance position. At 0.15 K there is a large decrease of the reflected signal at high fields, which cannot be explained just by the temperature, but may be attributed to the saturation.

There is no saturation at the peak position in the ferromagnetic phase. This is probably due to the fast relaxation of the system to the thermodynamic equilibrium, compared to the relatively low power of microwave excitation which populates higher energy levels. The effect of saturation might have been partially masked by the fact that the field strength is inhomogeneous across the sample, so while in some parts of the sample closer to the resonator the saturation might have been achieved, parts of the sample which are further away from the resonator are in weaker field and are therefore still not saturated. There are some indications of non-linearity at high fields, but we would need more experimental data to be sure.

4.4   Entanglement entropy

It has been suggested that the expectation values of thermodynamical observables such as internal energy or susceptibility can been used as entanglement witnesses [46, 54]. In Fig. 4.25b, we show the field dependance of the real part of the susceptibility, χ', which was obtained from the relative frequency shift $\chi'(f) \propto -\Delta f/f$ [49] off resonance at 1.7 and 5.6 GHz. The peak at 4.83 T agrees with the experimental critical field value found by Bitko *et al.* [16] at 0.15 K, which confirms that the temperature of our sample was indeed 0.15 K. Comparing the measured and mean-field χ' to the calculated entanglement entropy at 0.15 K (Fig. 4.25a), we find they behave remarkably similar across the QPT.

Since in our calculation the total wavefunction is approximated to a product of mean-field wavefunctions of the nuclear-electronic states the correlations between the electronic moments are neglected (Fig. 1.1c). On the other hand, an isolated nuclear-electronic state would not track the QPT which results from the underlying transverse-field Ising model as a solely many-body phenomenon. Therefore the extended entanglement present in the transverse-field Ising model may leave a signature on the nuclear-electronic states through hybridization.

Whilst current theory of entanglement entropy has largely focused on pure states of spin-1/2 one-dimensional systems or mixed states of two qubits [12, 46], the field is still developing. Strong hyperfine interaction has been previously suggested to limit our ability to observe intrinsic electronic criticality by the introduction of nuclear spin bath [26]. The novelty in our experimental scheme is that having access to nuclear spin as an observer may open an interesting avenue towards experimental probes of many body entanglement, and as such is intended as a stimulant for future theoretical and experimental work.
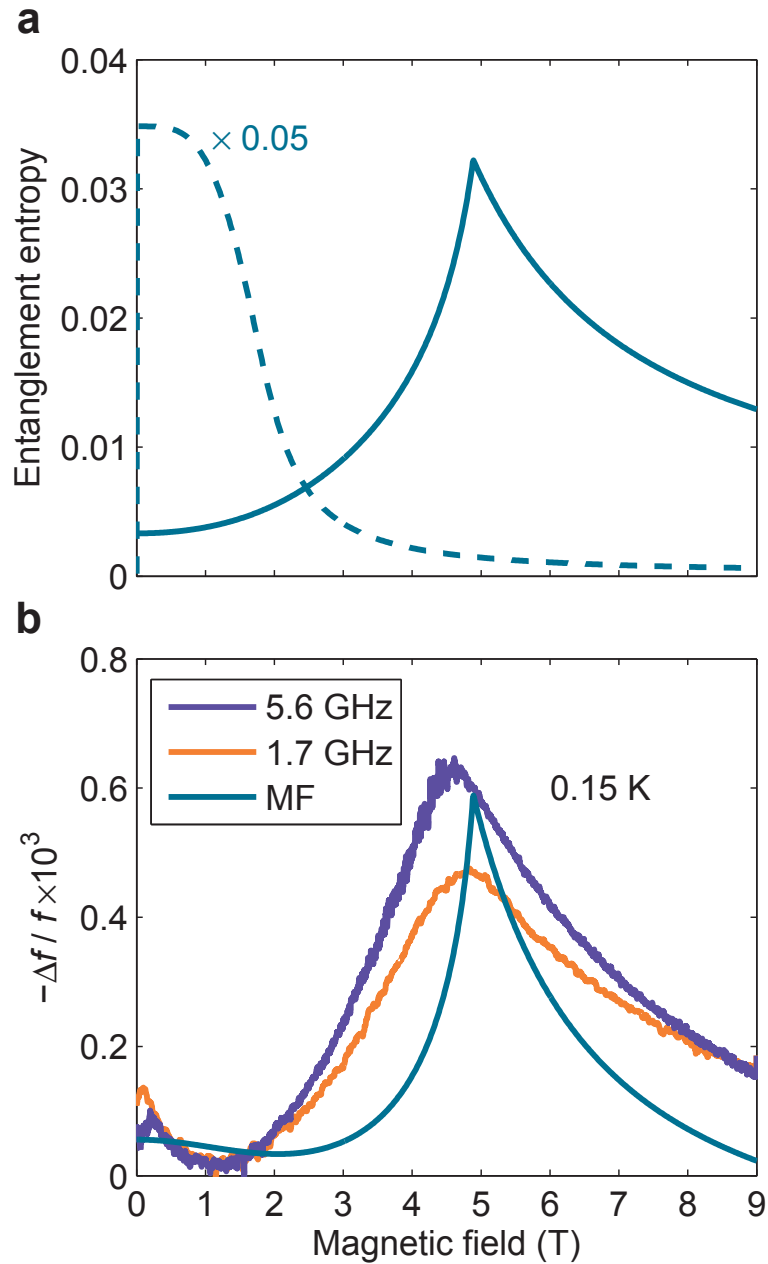
Figure 4.25: **a**) Entanglement entropy calculated for the ground state at 0.15 K, which is thermally populated between 54% and 74% at 0.15 K, as a function of transverse magnetic field (solid line). Dashed line is the entanglement entropy calculated without dipolar interactions in the single-ion limit. **b**) Relative shift in the resonance frequency, $\propto \chi'$, experimentally observed at 0.15 K as a function of field using 1.7 GHz (orange) and 5.6 GHz (purple) resonators. Mean-field calculation of the real part of the frequency-dependent susceptibility at 1.7 GHz and 0.15 K is shown by the blue line.

5 Conclusions

I calculated nuclear-electronic states and energy levels in LiHoF$_4$ by solving the single-ion Hamiltonian in the mean-field approximation. Excitations in the magnetic resonance experiment are simulated in the linear response framework based on mean-field states. Quantum entanglement of the nuclear-electronic states is quantified by entanglement entropy.

I developed the low-temperature continuous-wave magnetic resonance setup to probe the entangled nuclear-electronic states in LiHoF$_4$. The magnetic resonance was measured from 0.13 to 3 K in transverse magnetic field between 0 and 9 T. The experiment has been performed at five different frequencies from 1.7 to 5.6 GHz in order to investigate the excitations between hyperfine levels.

Temperature evolution of the absorption spectrum was measured at 3.4 and 3.9 GHz. To interpret the magnetic resonance absorption I compared the measured spectra to the calculated imaginary part of susceptibility. The frequency-dependent resonant fields in experiments showed excellent agreement with those obtained by calculations. I found that all the salient features of the experimental results are well reproduced by the model calculations.

Since the setup probes the hyperfine states directly, our measurements are shown to be very sensitive to the hyperfine coupling constant. This is particulary true when excitation frequency is 4.5 GHz, because it is right at the edge of hyperfine transition energies, so we used this measurement to refine the hyperfine constant.

Off-resonant measurements at 1.7, 4.5 and 5.6 GHz allowed us to map the phase diagram by extracting H$_C$ as a function of temperature. There is a very good agreement of measurements at all frequencies both with our calculated mean-field phase boundary and with previous experiments on LiHoF$_4$.

Having established experimentally that the mean-field wavefunctions are an excellent

approximation of the actual wavefunction, I used them to calculate the ground-state entanglement entropy between the electronic and nuclear magnetic moments. The calculated entanglement entropy in the absence of dipole interactions decreases smoothly as a function of transverse field. However, turning on dipolar coupling in the model produces a peak at the quantum phase transition, which reflects the enhanced mixing upon approaching the quantum phase transition.

Finally, I compared the off-resonant measurements at 1.7 and 5.6 GHz with calculated entanglement entropy. I find that the calculated entanglement entropy shows a peak at the quantum phase transition. This raises the tantalizing possibility that electronic entanglement is encoded onto the nuclear-electronic states, which presents an interesting avenue towards experimental probes of many-body entanglement.

6 Outlook

Our demonstration of nuclear-electronic magnetic resonance using a simple experimental scheme may find direct applications in other systems containing rare-earth ions, for instance, in rare-earth doped insulators or spin ice compounds.

$LiHoF_4$ diluted with nonmagnetic Yttrium, $LiHo_xY_{1-x}F_4$, evolves from a ferromagnet (x = 1) to a long range ordered ferromagnetic state with strong history dependent effects (x = 0.44), to a spin glass (x = 0.1 - 0.3) and to an antiglass phase (x < 0.1) [55, 56]. The positional randomness introduced by the dilution through the dipole coupling and the transverse field lead to random fields along the Ising direction. Very diluted $LiHo_xY_{1-x}F_4$ (x = 0.002) has been studied via ^{19}F NMR [57] where they found that at low temperature the field dependence of ^{19}F nuclear spin-lattice relaxation $1/T_1$ shows peaks in correspondence to the critical magnetic fields for energy level crossings. Nuclear-electronic energy states of Ho^{3+} ion could be probed directly by our magnetic resonance setup.

$LiErF_4$ is another interesting compound since it is one of the first model dipolar-coupled antiferromagnet with planar spin-anisotropy [27]. This compound has been studied by electron paramagnetic resonance [20, 58] and [7]Li nuclear magnetic resonance [59]. Nuclear-electronic sub-system coupling can be controlled by replacing Er with the nuclear-spin free [168]Er izotope. This allows us to separate the effects of electro-nuclear entanglement from purely electronic ones in the observed spectrum. In light of our results for $LiHoF_4$, this could be used to study the connection between measured susceptibility and entanglement entropy across the quantum phase transition further.

Nuclear spins play an important role in the spin ice compound $Ho_2Ti_2O_7$ [60] . Low lying weak excitations, observed by neutrons, are identified as nuclear spin system excitations. Hyperfine energy splitting of the Ho ion is estimated at 6.36 GHz, which is at the limit of the possible energy resolution in neutron scattering experiments. Nevertheless, our setup is ideally suited to examine such excitations in the gigaherz frequency spectrum.

We have shown that using our setup we are able to couple to electro-nuclear hybrid modes using a continuous-wave method. Following from this, it could be possible to develop pulsed mode techniques. Pulsed mode magnetic resonance has been already used in controlling quantum state of hybrid nuclear–electronic qubits in bismuth-doped silicon [3], and could be used for controlling rare-earth based qubits in rare-earth doped insulators [61].

A Code for calculating the suscepti-bility

On the next page I show the Matlab code I wrote to calculate the frequency dependant susceptibility in the linear response theory framework, based on the eigenstates and eigenvalues from the mean-field calculations.

```matlab
function linear_response_theory
cd('W:\MF_calc\variousA\A097')
load('0.150.mat') % loads variables "fields", "temp", "E" and "V"
% which are eigenstates and eigenvalues calculated in the mean-field model
% as a function of transverse field and temperature

for zzz = 1:length(freq_total(1,:)) %calculate susceptibility for all frequencies
    freq = freq_total (zzz);

J=8;
I=3.5;
gLande_Ho=1.25;

%Initiate J operators
Jz=diag(J:-1:-J);
Jzh=kron(Jz,eye(2*I+1));
Jp=diag(sqrt((J-[(J-1):-1:-J]).*(J+1+[(J-1):-1:-J])),1);
Jm=Jp';
Jph=kron(Jp,eye(2*I+1));
Jmh=kron(Jm,eye(2*I+1));
Jxh=(Jph+Jmh)/2;
Jyh=(Jph-Jmh)/2i;
%tensor product of cristal field to include nuclear moments
%Initiate I operators
Iz=diag(I:-1:-I);
Izh=kron(eye(2*J+1),Iz);
Ip=diag(sqrt((I-[(I-1):-1:-I]).*(I+1+[(I-1):-1:-I])),1);
Im=Ip';
Iph=kron(eye(2*J+1),Ip);
Imh=kron(eye(2*J+1),Im);
Ixh=(Iph+Imh)/2;
Iyh=(Iph-Imh)/2i;

ghztomeV = 1/241.8;
omega = freq*ghztomeV;      % define frequency sweep range (meV)
gama = 0.0001; % define lifetime (meV)

for l = 1:length(temp(1,:)) % calculate susceptibility for all temperatures
t = temp(1,l);

for k = 1:length(fields(1,:)) % calculate susceptibility for all fields
v = squeeze ( V(k,l,:,:) );
e = squeeze ( E(k,l,:) );
field = fields(1,k);

N = length(e);
chi_t = zeros(1,N^2);
ll = 1;
zz = zeros(1,N);
beta = 1/(t/11.6);
z=sum(exp(-beta*e));
zz=exp(-beta*e)/z;
```

```matlab
[n,np]=meshgrid(zz,zz);
NN=n-np;
[ee,eep]=meshgrid(e,e);
EE1=1./(ee-eep-omega);
EE = eep-ee-omega;
gamma = ones(size(EE))*gama;
G = gamma ./ (EE.^2 + gamma.^2);
G1 = EE ./ (EE.^2 + gamma.^2);


ELEf = 1.250 * 0.05788;
NUCf = 4.732 * 3.1519e-5;
JxhT = Jxh * ELEf;
IxhT = Ixh * NUCf;
JyhT = Jyh * ELEf;
IyhT = Iyh * NUCf;
JzhT = Jzh * ELEf;
IzhT = Izh * NUCf;
tittt = 'S(Jyy+Iyy)';
tt  = v'  * (JyhT+IyhT) * v;
chi_t  = (tt) .* (tt.') .* NN .* G;
chi_t1 = (tt) .* (tt.') .* NN .* G1;
sss=sum(sum(chi_t));
sss1=sum(sum(chi_t1));
imchi  (k) =  real(sss)   ;
rechi1 (k) =  real(sss1)  ;
end
        hfig1 = figure (1);
        clf
        set(hfig1,'position',[50 100 600 400])
        h1=plot (fields(1,:), imchi ,'r','LineWidth',2);
        set(gca,'XTick',[0,1,2,3,4,5,6,7,8,9]);
        set(gca,'fontsize',15)
        xlim([0 9]);
        xlabel('Magnetic field (T)','FontSize',15)
        ylabel('\chi'''' (arb. u.)','FontSize',15)

        hfig2 = figure (2);
        clf
        set(hfig2,'position',[680 100 600 400])
        h2=plot (fields(1,:), rechi1 ,'r','LineWidth',2);
        set(gca,'XTick',[0,1,2,3,4,5,6,7,8,9]);
        set(gca,'fontsize',15)
        xlim([0 9]);
        xlabel('Magnetic field (T)','FontSize',15)
        ylabel('\chi'' (arb. u.)','FontSize',15)
end
end
end
```

93

B Code for calculating the entanglement entropy

Here I show the Matlab code I wrote to calculate the entanglement entropy, by using the eigenstates and eigenvalues calculated in the mean-field aproximation.

```matlab
function entanglement_entropy
cd('D:\Projects\LiHoF4_Network_Analyzer\plots\new_analysis\A097-\mf')
load('0.150.mat') % loads variables "fields", "temp", "E" and "V"
% which are eigenstates and eigenvalues calculated in the mean-field model
% as a function of transverse field and temperature

J=8;
I=3.5;
gLande_Ho=1.25;

% Initiate J operators
Jz=diag(J:-1:-J);
Jzh=kron(Jz,eye(2*I+1));
Jp=diag(sqrt((J-[(J-1):-1:-J]).*(J+1+[(J-1):-1:-J])),1);
Jm=Jp';
Jph=kron(Jp,eye(2*I+1));
Jmh=kron(Jm,eye(2*I+1));
Jxh=(Jph+Jmh)/2;
Jyh=(Jph-Jmh)/2i;
%tensor product of cristal field to include nuclear moments
%Initiate I operators
Iz=diag(I:-1:-I);
Izh=kron(eye(2*J+1),Iz);
Ip=diag(sqrt((I-[(I-1):-1:-I]).*(I+1+[(I-1):-1:-I])),1);
Im=Ip';
Iph=kron(eye(2*J+1),Ip);
Imh=kron(eye(2*J+1),Im);
Ixh=(Iph+Imh)/2;
Iyh=(Iph-Imh)/2i;

for l = 1:length(temp(1,:)) % calculate entanglement entropy for all temperatures
for k = 1:length(fields(1,:)) % calculate entanglement entropy for all fields
    v = squeeze ( V(k,l,:,:));
    e = squeeze ( E(k,l,:));
    field = fields(1,k);
    Bbb = reshape(v(:,1),[8,17]);
    [U,S,Vv] = svd(B) ;
    tt = sum ( S .* S );
    entanglement_entorpy  (k) = - sum ( tt .* log(tt+eps) ) ;
end
fig1 = figure (1); hold on;
hpcfr = plot (fields(1,:), entanglement_entorpy + br ,'b','LineWidth',2);
set(gca,'fontsize',15);
text(8,br+1,num2str(temp(1,l)));
set(fig1,'position',[100 100 600 400])
xlabel('Field (T)','FontSize',15)
ylabel('Entanglement entropy','FontSize',15)
title('Entanglement entropy','FontSize',15)
end
end
```
96

Bibliography

[1] Ze-Liang Xiang, Sahel Ashhab, J. Q. You, and Franco Nori. Hybrid quantum circuits: Superconducting circuits interacting with other quantum systems. *Rev. Mod. Phys.*, 85:623–653, Apr 2013.

[2] Gershon Kurizki, Patrice Bertet, Yuimaru Kubo, Klaus Mølmer, David Petrosyan, Peter Rabl, and Jörg Schmiedmayer. Quantum technologies with hybrid systems. *Proceedings of the National Academy of Sciences*, 112(13):3866–3873, 2015.

[3] Gavin W. Morley, Petra Lueders, M. Hamed Mohammady, S. etrak J. Balian, G. abriel Aeppli, Christopher W. M. Kay, Wayne M. Witzel, Gunnar Jeschke, and Tania S. Monteiro. Quantum control of hybrid nuclear- electronic qubits. *Nat Mater*, 12(2):107, 2013.

[4] Iulia Buluta and Franco Nori. Quantum simulators. *Science*, 326(5949):108–111, 2009.

[5] I. M. Georgescu, S. Ashhab, and Franco Nori. Quantum simulation. *Rev. Mod. Phys.*, 86:153–185, Mar 2014.

[6] Luigi Amico, Rosario Fazio, Andreas Osterloh, and Vlatko Vedral. Entanglement in many-body systems. *Rev. Mod. Phys.*, 80:517–576, May 2008.

[7] J. Eisert, M. Cramer, and M. B. Plenio. *Colloquium*: Area laws for the entanglement entropy. *Rev. Mod. Phys.*, 82:277–306, Feb 2010.

[8] S. Ghosh, T. F. Rosenbaum, G. Aeppli, and S. N. Coppersmith. Entangled quantum state of magnetic dipoles. *Nature*, 425(6953):48–51, Sep 2003.

[9] N. B. Christensen, H. M. Rønnow, D. F. McMorrow, A. Harrison, T. G. Perring, M. Enderle, R. Coldea, L. P. Regnault, and G. Aeppli. Quantum dynamics and entanglement of spins on a square lattice. *Proc Natl Acad Sci U S A*, 104(39):15264–15269, Sep 2007. 6387[PII].

[10] S. Sahling, G. Remenyi, C. Paulsen, P. Monceau, V. Saligrama, C. Marin, A. Revcolevschi, L. P. Regnault, S. Raymond, and J. E. Lorenzo. Experimental

realization of long-distance entanglement between spins in antiferromagnetic quantum spin chains. *Nat Phys*, 11(3):255–260, Mar 2015. Article.

[11] Tobias J. Osborne and Michael A. Nielsen. Entanglement in a simple quantum phase transition. *Phys. Rev. A*, 66:032110, Sep 2002.

[12] A. Osterloh, Luigi Amico, G. Falci, and Rosario Fazio. Scaling of entanglement close to a quantum phase transition. *Nature*, 416(6881):608–610, Apr 2002.

[13] Michael Levin and Xiao-Gang Wen. Detecting topological order in a ground state wave function. *Phys. Rev. Lett.*, 96:110405, Mar 2006.

[14] Hui Li and F. D. M. Haldane. Entanglement spectrum as a generalization of entanglement entropy: Identification of topological order in non-abelian fractional quantum hall effect states. *Phys. Rev. Lett.*, 101:010504, Jul 2008.

[15] Hong-Chen Jiang, Zhenghan Wang, and Leon Balents. Identifying topological order by entanglement entropy. *Nat Phys*, 8(12):902–905, Dec 2012.

[16] D. Bitko, T. F. Rosenbaum, and G. Aeppli. Quantum critical behavior for a model magnet. *Phys. Rev. Lett.*, 77:940–943, Jul 1996.

[17] H. M. Rønnow, R. Parthasarathy, J. Jensen, G. Aeppli, T. F. Rosenbaum, and D. F. McMorrow. Quantum phase transition of a magnet in a spin bath. *Science*, 308(5720):389–392, 2005.

[18] Sergio Boixo, Troels F. Ronnow, Sergei V. Isakov, Zhihui Wang, David Wecker, Daniel A. Lidar, John M. Martinis, and Matthias Troyer. Evidence for quantum annealing with more than one hundred qubits. *Nat Phys*, 10(3):218–224, Mar 2014. Article.

[19] G. Mennenga, L.J. de Jongh, W.J. Huiskamp, and I. Laursen. A comparative study of the magnetic ordering specific heats of four s = 12 dipolar magnets: Lirf4 (r = er, dy, ho, tb). *Journal of Magnetism and Magnetic Materials*, 44(1):48 – 58, 1984.

[20] J. Magariño, J. Tuchendler, P. Beauvillain, and I. Laursen. Epr experiments in $litbf_4$, $lihof_4$, and $lierf_4$ at submillimeter frequencies. *Phys. Rev. B*, 21:18–28, Jan 1980.

[21] M. Schechter and P. C. E. Stamp. Derivation of the low-t phase diagram of $liho_x y_{1-x} f_4$: A dipolar quantum ising magnet. *Phys. Rev. B*, 78:054438, Aug 2008.

[22] H. M. Rønnow, J. Jensen, R. Parthasarathy, G. Aeppli, T. F. Rosenbaum, D. F. McMorrow, and C. Kraemer. Magnetic excitations near the quantum phase transition in the ising ferromagnet $LiHof_4$. *Phys. Rev. B*, 75:054426, Feb 2007.

[23] A. I. & Khmel'nitskiǐ D. E. Larkin. Phase transition in uniaxial ferroelectrics. *Sov. Phys. JETP*, 29:1123–1128, 1969.

[24] Amnon Aharony. Critical behavior of magnets with dipolar interactions. v. uniaxial magnets in d dimensions. *Phys. Rev. B*, 8:3363–3370, Oct 1973.

[25] P. C. E. Prokof'ev, N. V. & Stamp. Theory of spin bath. *Rep. Prog. Phys.*, 63:669, 2000.

[26] H. M. Rønnow, R. Parthasarathy, J. Jensen, G. Aeppli, T. F. Rosenbaum, and D. F. McMorrow. Quantum phase transition of a magnet in a spin bath. *Science*, 308(5720):389–392, 2005.

[27] Conradin Kraemer, Neda Nikseresht, Julian O. Piatek, Nikolay Tsyrulin, Bastien Dalla Piazza, Klaus Kiefer, Bastian Klemke, Thomas F. Rosenbaum, Gabriel Aeppli, Ché Gannarelli, Karel Prokes, Andrey Podlesnyak, Thierry Strässle, Lukas Keller, Oksana Zaharko, Karl W. Krämer, and Henrik M. Rønnow. Dipolar antiferromagnetism and quantum criticality in lierf4. *Science*, 336(6087):1416–1419, 2012.

[28] International Union of Crystallography. International tables for crystallography. online, 2006.

[29] P. B. Chakraborty, P. Henelius, H. Kjønsberg, A. W. Sandvik, and S. M. Girvin. Theory of the magnetic phase diagram of $\mathrm{LiHof_4}$. *Phys. Rev. B*, 70:144411, Oct 2004.

[30] M.T. Hutchings. Point-charge calculations of energy levels of magnetic ions in crystalline electric fields. volume 16 of *Solid State Physics*, pages 227 – 273. Academic Press, 1964.

[31] K W H Stevens. Matrix elements and operator equivalents connected with the magnetic properties of rare earth ions. *Proceedings of the Physical Society A*, 65:209–215, March 1952.

[32] B Bleaney and K W H Stevens. Paramagnetic resonance. *Reports on Progress in Physics*, 16(1):108, 1953.

[33] S. M. A. Tabei, M. J. P. Gingras, Y.-J. Kao, and T. Yavors'kii. Perturbative quantum monte carlo study of lihof$_4$ in a transverse magnetic field. *Phys. Rev. B*, 78:184408, Nov 2008.

[34] A. Biltmo and P. Henelius. Phase diagram of the dilute magnet $\mathrm{Liho}_x\mathrm{y}_{1-x}\mathrm{f}_4$. *Phys. Rev. B*, 76:054423, Aug 2007.

[35] Peter Meyer, Jacques Pommier, and Jacques Ferre. Magnetooptic observation of domains at low temperature in the transparent ferromagnet lihof[sub]4[/sub], 1989.

[36] Pau Jorba. *SHPM imaging of LiHoF$_4$ at ultra low temperatures*. PhD thesis, EPFL, 2014. http://lqm.epfl.ch/page-66986-en.html.

Bibliography

[37] J. Jensen and A. R. Mackintosh. *Rare Earth Magnetism.* Clarendon Press Oxford, 1991.

[38] A. Einstein, B. Podolsky, and N. Rosen. Can quantum-mechanical description of physical reality be considered complete? *Phys. Rev.*, 47:777–780, May 1935.

[39] S. Sachdev. *Quantum Phase Transitions.* Cambridge University Press, 1999.

[40] S. L. Sondhi, S. M. Girvin, J. P. Carini, and D. Shahar. Continuous quantum phase transitions. *Rev. Mod. Phys.*, 69:315–333, Jan 1997.

[41] William K. Wootters. Entangled chains. 7 2003.

[42] M. C. Arnesen, S. Bose, and V. Vedral. Natural thermal and magnetic entanglement in the 1d heisenberg model. *Phys. Rev. Lett.*, 87:017901, Jun 2001.

[43] D. Gunlycke, V. M. Kendon, V. Vedral, and S. Bose. Thermal concurrence mixing in a one-dimensional ising model. *Phys. Rev. A*, 64:042302, Sep 2001.

[44] Xiaoguang Wang, Hongchen Fu, and Allan I Solomon. Thermal entanglement in three-qubit heisenberg models. *Journal of Physics A: Mathematical and General*, 34(50):11307, 2001.

[45] Xiaoguang Wang. Entanglement in the quantum heisenberg XY model. *Phys. Rev. A*, 64:012313, Jun 2001.

[46] Marcin Wieśniak, Vlatko Vedral, and Časlav Brukner. Magnetic susceptibility as a macroscopic entanglement witness. *New Journal of Physics*, 7(1):258, 2005.

[47] *Elexsys E 500 user's manual.* Bruker, 2001.

[48] L. A. Sorin and M. V. Vlasova. *Electron Spin Resonance of Paramagnetic Crystals.* Springer, 1973.

[49] Brian Cowan. *Nuclear Magnetic Resonance and Relaxation.* Cambridge University Press, 1997.

[50] Simeon Mark Warner. *NMR Spectroscopy and the Crystal-Field Interaction in Holmium Trifluoride.* PhD thesis, University of Manchester, 1994.

[51] *Principles of dilution refrigeration.* Oxford Instruments, 2015.

[52] Wikipedia. dbm decibel-milliwatts, 2015. [Online; accessed 22-July-2004].

[53] Tim Duty. Towards superconductor-spin ensemble hybrid quantum systems. *Physics 3, 80*, 80, Sep 2010.

[54] Géza Tóth. Entanglement witnesses in spin models. *Phys. Rev. A*, 71:010301, Jan 2005.

[55] C. Ancona-Torres, D. M. Silevitch, G. Aeppli, and T. F. Rosenbaum. Quantum and classical glass transitions in $\text{liho}_x\text{y}_{1-x}\text{f}_4$. *Phys. Rev. Lett.*, 101:057201, Jul 2008.

[56] Michel J P Gingras and Patrik Henelius. Collective phenomena in the lihoyf4 quantum ising magnet recent progress and open questions. *Journal of Physics: Conference Series*, 320(1):012001, 2011.

[57] M. J. Graf, A. Lascialfari, F. Borsa, A. M. Tkachuk, and B. Barbara. Probing spin dynamics and quantum relaxation in $\text{Liy}_{0.998}\text{ho}_{0.002}\text{f}_4$ via ^{19}F nmr. *Phys. Rev. B*, 73:024403, Jan 2006.

[58] M R Brown, K G Roots, and W A Shand. Energy levels of er 3+ in liyf 4. *Journal of Physics C: Solid State Physics*, 2(4):593, 1969.

[59] P. E. Hansen, T. Johansson, and R. Nevald. Magnetic properties of lithium rare-earth fluorides: Ferromagnetism in lierf$_4$ and lihof$_4$ and crystal-field parameters at the rare-earth and li sites. *Phys. Rev. B*, 12:5315–5324, Dec 1975.

[60] G Ehlers, E Mamontov, M Zamponi, and J S Gardner. Low lying spin excitation in the spin ice, ho 2 ti 2 o 7. *Journal of Physics: Conference Series*, 251(1):012003, 2010.

[61] BertainaS., GambarelliS., TkachukA., KurkinI N., MalkinB., StepanovA., and BarbaraB. Rare-earth solid-state qubits. *Nat Nano*, 2(1):39–42, Jan 2007.

IVAN KOVAČEVIĆ

Chemin de Renens 41
1004 Lausanne
+41 78 943 3511
ivankowacevic@gmail.com
linkedin.com/in/kovacevici
29 November 1985
Croatian, Swiss working permit B
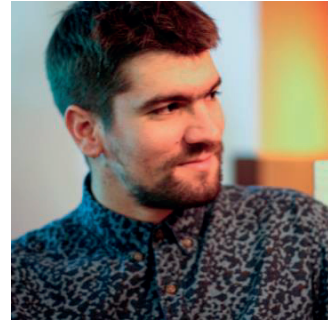
RESEARCH EXPERIENCE

02/2012 – Present
Swiss Federal Institute of Technology Lausanne EPFL, Laboratory for Quantum Magnetism LQM
Doctoral Assistant

- Developing hypotheses, computer simulation of physical model
- Designing, developing and testing microwave experimental setup in collaboration with 2 postdoctoral fellows and other experts
- Writing software for remote instrument control and data collection
- Operating sophisticated ultra-low temperature experiments
- Analysing data, drawing conclusions
- Writing publications and proposals for experiments at large international facilities
- Mentoring and tutoring undergraduate students

03/2011 – 10/2011
Institute of Physics, Laboratory for Dielectric Spectroscopy and Magnetotransport, Zagreb, Croatia
Assistant in research project

EDUCATION

02/2012 – 02/2016 (est.)
PhD in Physics
Doctoral Program in Physics EDPY
Swiss Federal Institute of Technology Lausanne EPFL

PhD thesis topic: "Probing entangled states of a nuclear-electronic quantum magnet"

09/2006 – 07/2011
Master of Science in Physics (mag. phys.)
Integrated Bachelor and Master program (10 semesters)
Department of Physics, Faculty of Science, University of Zagreb, Croatia

AWARDS & SCHOLARSHIPS

2015	Outstanding job as a teaching assistant at General Physics III course
2011	Top 10 graduated students in Physics based on GPA (4.6 out of 5.0)
2004 – 2011	Scolarship City of Split and National scholarship for gifted students
2000, 2001, 2003	2nd, 1st, 3rd prize at the National Physics Competition

ADDITIONAL EXPERIENCE

10/2005 – Present   **Founder, Owner and Online Community Manager**
www.dubstepforum.com, Dubstep Forum Awards

10/2006 – Present   **Promoter and DJ**
Confusion Association, Illectricity Festival in Zagreb, Croatia

ADDITIONAL SKILLS

Computer skills
- Algorithm development and data analysis, Matlab
- High-level programming language, Visual Basic .NET
- 3D CAD software for mechanical design, Autodesk Inventor
- Statistical data analysis and graphics software, SigmaPlot, Origin

Languages   English (C1), French (A2), Italian (A2), Croatian (mother tongue)

HOBBIES

Water polo   Lausanne Natation water polo club (Swiss National League B)

PUBLICATIONS

- I. Kovacevic, P. Babkevich, M. Jeong, J. O. Piatek, G. Boero, H. M. Rønnow. Probing entangled states of a nuclear-electronic quantum magnet. *In Review*.

- P. Babkevich, M. Jeong, Y. Matsumoto, I. Kovacevic, A. Finco, R. Toft-Petersen, C. Ritter, M. Mansson, S. Nakatsuji, and H. M. Rønnow. Universal Dimensional Reduction in Quantum Dipolar Antiferromagnets. *Phys. Rev. Lett.,* Accepted 19 April 2016.

- P. Babkevich, A. Finco, M. Jeong, B. Dalla Piazza, I. Kovacevic, G. Klughertz, K. W. Krämer, C. Kraemer, D. T. Adroja, E. Goremychkin, T. Unruh, T. Strässle, A. Di Lieto, Jensen, and H. M. Rønnow. Neutron spectroscopic study of crystal-field excita- tions and the effect of the crystal field on dipolar magnetism in $LiRF_4$ (r = Gd, Ho, Rr, Tm, and Yb). *Phys. Rev. B*, 92:144422, Oct 2015.

- J. O. Piatek, I. Kovacevic, P. Babkevich, B. Dalla Piazza, S. Neithardt, J. Gavilano, W. Krämer, and H. M. Rønnow. Nonequilibrium hysteresis and spin relaxation in the mixed-anisotropy dipolar-coupled spin-glass $LiHo_{0.5}Er_{0.5}F_4$. *Phys. Rev. B*, 90:174427, Nov 2014.

- T. Ivek, I. Kovačević, M. Pinterić, B. Korin-Hamzić, S. Tomić, T. Knoblauch, D. Schweitzer, and M. Dressel. Cooperative dynamics in charge-ordered state of α-$(BEDT\text{-}TTF)_2I_3$. *Phys. Rev. B*, 86:245125, Dec 2012.